# Hadron production via $e^+e^-$ collisions with initial state radiation

V. P. Druzhinin, S. I. Eidelman, S. I. Serednyakov, and E. P. Solodov

*Budker Institute of Nuclear Physics SB RAS, Novosibirsk, 630090, Russia and Novosibirsk State University, Novosibirsk, 630090, Russia*

(published 6 December 2011)

A novel method of studying $e^+e^-$ annihilation into hadrons using initial state radiation at $e^+e^-$ colliders is described. After a brief history of the method, its theoretical foundations are considered. Numerous experiments in which exclusive cross sections of $e^+e^-$ annihilation into hadrons below the center-of-mass energy of 5 GeV have been measured are presented. Some applications of the experimental results to fundamental tests of the standard model are listed.

DOI: 10.1103/RevModPhys.83.1545 PACS numbers: 13.66.Bc, 14.40.Be, 14.40.Pq

## CONTENTS



## I. INTRODUCTION

### A. Why is low-energy $e^+e^-$ annihilation interesting?

Studies of low-energy $e^+e^-$ annihilation into hadrons are of great interest for theory and have numerous applications. According to current concepts, $e^+e^-$ annihilation into hadrons proceeds via an intermediate virtual photon that produces a pair of quarks $q\bar{q}$, followed by the hadronization of quarks into observed hadrons. This process is described by the lowest-order Feynman diagram shown in Fig. 1. When the initial energy of $e^+e^-$, or equivalently of the intermediate virtual photon, is large enough, the process of hadronization is well described by QCD. At small energies, lower than 2–3 GeV, produced hadrons are relatively soft and intensively interact with each other forming hadronic resonances. At the moment QCD fails to describe this energy region. Because of that, it is vitally important to gain sufficient information from experiment to be used as input for various QCD-based theoretical models. QCD sum rules are an example of how measurements of total and exclusive cross sections can be used to extract such fundamental parameters of theory as the strong coupling constant $\alpha_s$, quark, and gluon condensates (Shifman, Vainshtein, and Zacharov, 1979).

Precise knowledge of vacuum polarization effects based on the total cross section of $e^+e^-$ annihilation into hadrons is necessary to estimate the hadronic contributions to the running fine-structure constant and thus determine its value at the $Z$ boson mass $\alpha(M_Z^2)$, a key component of the high-precision tests of the standard model (Burkhardt *et al.*, 1989; Eidelman and Jegerlehner, 1995; Hagiwara *et al.*, 2003; Burkhardt and Pietrzyk, 2005; Actis *et al.*, 2010).

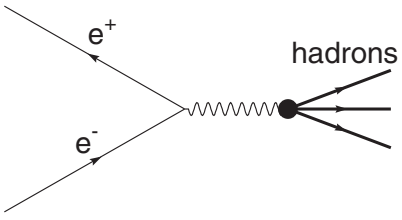


FIG. 1. The lowest-order Feynman diagram describing the process of $e^+e^-$ annihilation into hadrons.

 

Improvement of the precision with which the total cross section of $e^+e^-$ annihilation into hadrons is known is also needed for a more accurate estimation of the hadronic contribution to the muon anomalous magnetic moment because it is one of the crucial limiting factors in a search for new physics (Bouchiat and Michel, 1961; Gourdin and de Rafael, 1969; Bennett *et al.*, 2006).

There is an important relation between spectral functions in $e^+e^-$ annihilation into hadrons with isospin $I=1$ and corresponding $\tau$ lepton decays based on conservation of vector current (CVC) and isospin symmetry (Thacker and Sakurai, 1971; Tsai and Tsai, 1971). Although first detailed tests of such relations showed satisfactory agreement between such spectral functions (Kawamoto and Sanda, 1978; Eidelman and Ivanchenko, 1991), higher accuracy reached in both $e^+e^-$ and $\tau$ lepton sectors revealed possible systematic effects not accounted for in the $e^+e^-$ and/or $\tau$ experiments (Davier *et al.*, 2003a, 2003b). An understanding of these effects is crucial for improving the accuracy with which the hadronic contributions to the muon anomalous magnetic moment can be estimated from $\tau$ decays to two and four pions as first suggested by Alemany, Davier, and Höcker (1998).

Detailed measurements of the energy dependence of various exclusive cross sections allow us to improve our knowledge of vector mesons and look for new states, both of light (Druzhinin, 2007) and heavy quarks (Eichten *et al.*, 2008).

### B. Initial state radiation

In $e^+e^-$ collider experiments, exclusive and total hadronic cross sections are usually measured by scanning the accessible energy range. The process of $e^+e^-$ annihilation is accompanied by emission of one or several photons from the initial state. The lowest-order Feynman diagram describing initial state radiation (ISR) is shown in Fig. 2. The quantity measured directly in the experiment is the visible cross section

$$\sigma_{\rm vis}=\frac{N}{L}, \tag{1}$$

where $N$ is the number of selected events of the process $e^+e^-\to$ hadrons $+n\gamma$, $n=0,1,2,\ldots$, and $L$ is the integrated luminosity of the collider collected at the center-of-mass (c.m.) $e^+e^-$ energy $2E_0$. The visible cross section is related to the Born cross section $\sigma_0$ corresponding to the lowest-order diagram of Fig. 1 via the integral (Kuraev and Fadin, 1985) providing the $10^{-3}$ accuracy:

$$\sigma_{\rm vis}=\int_0^{1-m_{\rm min}^2/s}\varepsilon(s,x)W(s,x)\sigma_0[s(1-x)]dx, \tag{2}$$

where $s=4E_0^2$, $x$ is an effective fraction of the beam energy $E_0$ carried by photons emitted from the initial state, $m_{\rm min}$ is the minimal possible invariant mass of the final hadrons, and $\varepsilon(s,x)$ is the detection efficiency for the process $e^+e^-\to$ hadrons $+n\gamma$ as a function of $x$ and $s$. The so-called radiator function $W(s,x)$, taking into account higher-order QED contributions, in particular, from the diagram in Fig. 2, is fully calculable in QED (Actis *et al.*, 2010). Because of the photon

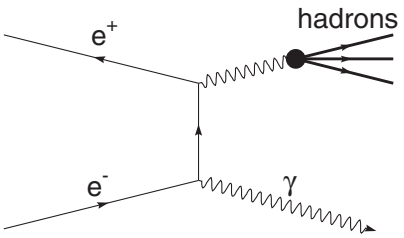


FIG. 2. The lowest-order Feynman diagram describing the initial state radiation process $e^+e^-\to\gamma+$ hadrons.

emission from the initial state, the visible cross section depends on the Born cross section at all energies below the nominal $e^+e^-$ c.m. energy $2E_0$.

In conventional scanning experiments, the influence of ISR is suppressed by the requirements of the energy and momentum balance between the final hadrons and the initial $e^+e^-$ state. In this case the detection efficiency has an $x$ dependence close to the step function $\varepsilon(s,x)=\varepsilon_0(s)$ for $x<x_0$, and zero for $x>x_0$. At small $x_0$, Eq. (2) can be rewritten as

$$\sigma_{\rm vis}=\varepsilon_0(s)\sigma_0(s)[1+\delta(s)], \tag{3}$$

where $1+\delta(s)$ is the radiative correction factor, which takes into account higher-order QED corrections. To calculate this factor it is necessary to know the $s$ dependence of $\sigma_0$ in the range from $s(1-x_0)$ to $s$. For slowly varying cross sections, $\delta$ is about 10% and can be determined with an accuracy better than 1% using existing data on the cross section energy dependence. Thus, in scanning experiments, from the data collected at the c.m. energy $\sqrt{s}$, the cross section $\sigma_0(s)$ is determined directly.

Another approach is also possible. Equation (2) can be rewritten in the differential form:

$$\frac{d\sigma_{\rm vis}(s,m)}{dm}=\frac{2m}{s}\varepsilon(s,m)W(s,x)\sigma_0(m), \tag{4}$$

where we have made a transformation to the variable $m=\sqrt{s(1-x)}$, the invariant mass of the hadronic system. At nonzero $x$ the dominant contribution to the visible cross section comes from the one-photon ISR (see Fig. 2). With the inclusion of the ISR photon momentum in the selection conditions on the energy and momentum balance, the nonzero detection efficiency for ISR events can be obtained in a wide range of the hadronic invariant mass. As a result, from the measurement of the mass spectrum for the process $e^+e^-\to$ hadrons $+\gamma$ at fixed c.m. energy $\sqrt{s}$, the cross section $\sigma_0(m)$ can be extracted in the invariant-mass range from threshold to the mass close to $\sqrt{s}$.

The idea of utilizing initial state radiation from a high-mass state to explore electron-positron processes at all energies below that state was previously outlined by Baier and Khoze (1965) and Baier and Fadin (1968). The possibility of exploiting such processes at high-luminosity $\phi$ and $B$ factories was discussed by Arbuzov *et al.* (1998), Benayoun *et al.* (1999), Binner, Kühn, and Melnikov (1999), and Konchatnij and Merenkov (1999) and motivated studies described in this paper.

Analysis of ISR events at $e^+e^-$ factories provides independent and contiguous measurements of hadronic cross sections in the low-energy region and also contributes to the spectroscopy of low-mass resonances.

### C. Calculation of ISR and accuracy

To lowest order (see Fig. 2), the probability of the initial state radiation of the photon with energy $xE_0$ and polar angle $\theta$ is as follows (Baier and Khoze, 1965; Bonneau and Martin, 1971):

$$w_0(\theta, x) = \frac{\alpha}{\pi x}\left[\frac{(1 - x + x^2/2)\sin^2\theta - (x^2/2)\sin^4\theta}{[\sin^2\theta + (4m_e^2/s)\cos^2\theta]^2} - \frac{4m_e^2}{s}\frac{(1-2x)\sin^2\theta - x^2\cos^4\theta}{[\sin^2\theta + (4m_e^2/s)\cos^2\theta]^2}\right], \quad (5)$$

where $\alpha$ is the fine-structure constant, and $m_e$ is the electron mass.

The ISR photon is predominantly emitted at small angles with respect to the beam axis. In Fig. 3 we show the dependence of the function $W_0(\theta_0, x)/W_0(0, x)$ on the polar-angle limit $\theta_0$, where

$$W_0(\theta_0, x) = \int_{\theta_0}^{\pi-\theta_0} w_0(\theta, x)\sin\theta d\theta. \quad (6)$$

The integration is performed for three values of $x$ at $2E_0 = 10.58$ GeV, the c.m. energy of $B$ factories. It can be seen that the angular distribution of the ISR photon weakly depends on $x$ and that a considerable fraction of photons is emitted at large angles. In the next section we discuss two approaches to study ISR events, a tagged and an untagged one. In the tagged approach the ISR photon should be detected, i.e., emitted at a large angle, into the fiducial volume of the detector. At $B$ factories ($2E_0 = 10.58$ GeV) about 10% of high-energy ISR photons have $30° < \theta < 150°$. This angular range corresponds approximately to the fiducial volume of the electromagnetic calorimeter of the *BABAR* detector. A fraction of the large-angle ISR increases with a decrease in energy as shown in Fig. 4. The compact expressions for $W_0$ can be written for two practically applicable cases. For the range of integration $\theta_0 < \theta < \pi - \theta_0$, $\theta_0 \gg m_e/\sqrt{s}$,

$$W_0(\theta_0, x) = \frac{\alpha}{\pi x}\left[(2 - 2x + x^2)\ln\frac{1 + \cos\theta_0}{1 - \cos\theta_0} - x^2\cos\theta_0\right]. \quad (7)$$

For the full range of polar angles $0 < \theta < \pi$,

$$W_0(0, x) = \frac{\alpha}{\pi x}\left(\ln\frac{s}{m_e^2} - 1\right)(2 - 2x + x^2). \quad (8)$$

The formulas given above describe ISR processes in the lowest QED order. To estimate a contribution of higher-order diagrams (loops and related to extra photon emission) the function $W(x)$ from Kuraev and Fadin (1985) can be used, which takes into account soft multiphoton emission and $\alpha^2$ terms in the leading logarithmic approximation. In this approximation the accuracy $\Delta W/W$ is expected to be better than 1%. The relative difference between $W(x)$ and $W_0(0, x)$ as a function of the invariant mass of the final hadronic system is shown in Fig. 5 for $2E_0 = 1.02$ GeV, the c.m. energy of the $\phi$ factory in Frascati. It can be seen that the radiative correction to the lowest-order radiator function reaches 15%. It should be noted that the size of the radiation correction depends on experimental conditions. For example, Aubert *et al.* (2006a) calculated the function $W(x)$ at $2E_0 = 10.58$ GeV with conditions that the highest-energy ISR photon has a polar angle in the range $20° < \theta < 160°$ and that the invariant mass of the hadronic system combined with the ISR photon is $>8$ GeV$/c^2$. The latter condition restricts the maximum energy of extra photons emitted from the initial state. With these conditions the radiative correction factor $1 + \delta = W(20°, x)/W_0(20°, x)$ is close to unity with the maximum deviation $\delta$ of about 2%.

To provide accuracy better than 1% required for the measurement of the exclusive hadronic cross sections at low energies, the calculation of the radiator function should include the higher-order radiative correction, in particular, due

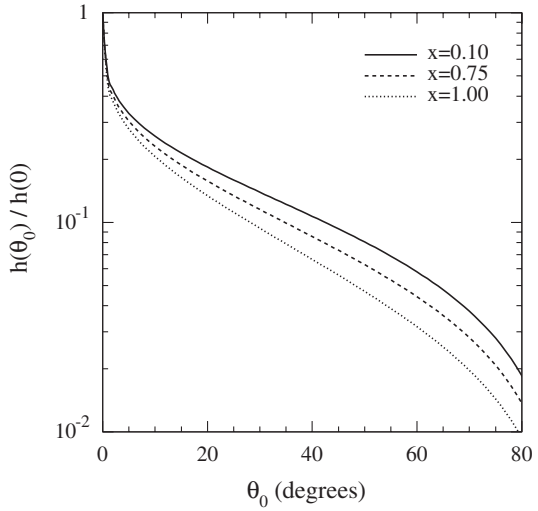


FIG. 3. The relative probability for the ISR photon emitted into the polar-angle range $\theta_0 < \theta < 180° - \theta_0$ for three representative values of $x$.

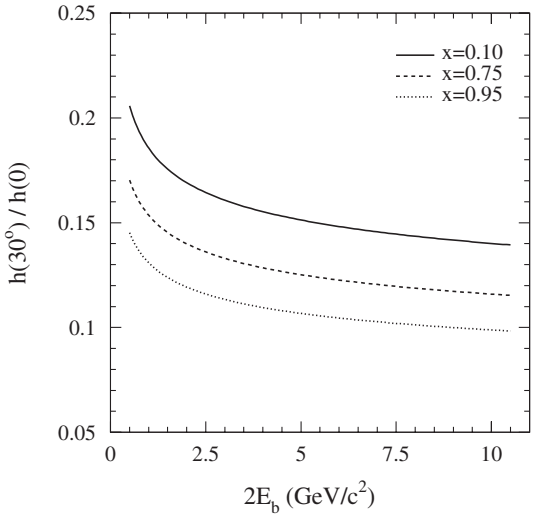


FIG. 4. The relative probability for the ISR photon emitted into the polar-angle range $30° < \theta < 150°$ as a function of the $e^+e^-$ c.m. energy for three representative values of $x$.

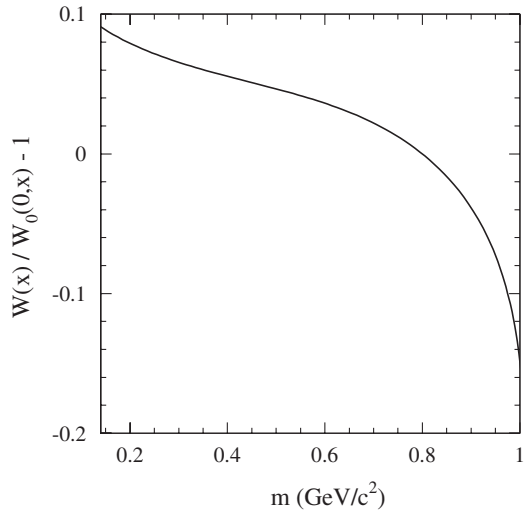


FIG. 5. The mass ($m = 2E_0\sqrt{1-x}$) dependence of the relative difference between the radiator function $W(x)$ from Kuraev and Fadin (1985) and the lowest-order function $W_0(0, x)$ for $2E_0 =$ 1.02 GeV.

to emission of extra photons. Several theoretical papers are devoted to study radiative corrections to ISR processes, for example, Arbuzov *et al.* (1998), Binner, Kühn, and Melnikov (1999), Khoze *et al.* (2001, 2002), Rodrigo *et al.* (2002), and Czyż *et al.* (2003). The approaches of Binner, Kühn, and Melnikov (1999), Rodrigo *et al.* (2002), and Czyż *et al.* (2003) allow one to develop generators of Monte Carlo (MC) events and are used in analyses of experimental data. Binner, Kühn, and Melnikov (1999) considered the photon emission at large angles only; radiative corrections are calculated in the leading logarithmic approximation with the structure function technique (Caffo, Czyż, and Remiddi, 1994, 1997). The accuracy of the method is determined by neglecting subleading $\alpha^2$ contributions and is estimated by Rodrigo *et al.* (2001) to be about 1%. Rodrigo *et al.* (2002), Czyż *et al.* (2003) calculated the one-loop corrections and exact matrix element for emission of two hard photons. The accuracy of this next-to-leading-order (NLO) calculation is estimated to be about 0.5% (Rodrigo *et al.*, 2002) due to higher-order effects.

### D. Monte Carlo generators

The calculation of the radiator function is usually performed with the Monte Carlo method. A special computer code referred to as an ''event generator'' provides events (sets of the four momenta of the final particles) distributed over the phase space according to the matrix element squared of the process under study. The phase space can be restricted by placing conditions on the angles and energies of the generated ISR photons. These conditions should be less strict than the actual experimental conditions used for event selection.

The interaction of the generated particles with the detector and the detector response are then simulated. In modern experiments the detector simulation is based on the GEANT4 (Agostinelli *et al.*, 2003) package. The simulated events are reconstructed with the program chain used for experimental data. The detection efficiency is determined as the ratio of the mass spectrum of simulated events that passed selection criteria to the spectrum of generated events.

Most of the ISR analyses discussed in this paper are based on two event generators. Historically, EVA was the first ISR Monte Carlo generator. The AFKQED package used in the *BABAR* experiment at the Stanford Linear Accelerator Center (SLAC) $B$ factory is a development of the EVA generator (Binner, Kühn, and Melnikov, 1999; Czyż and Kühn, 2001) initially designed to simulate ISR production of $2\pi$ and $4\pi$ final states with an ISR photon emitted at large angles. The soft-photon radiation from the initial state is generated with the structure function method (Caffo, Czyż, and Remiddi, 1994, 1997). Two extra photons are emitted in the directions of the initial electron and positron. The program has a modular structure allowing us to implement new hadronic modes easily. The AFKQED package includes generations of $2\pi$, $3\pi$, $4\pi$, $5\pi$, $6\pi$, and $\eta\pi^+\pi^-$ states, modes with kaons $K\bar{K} + n\pi n = 0$, 1, 2, 3, and 4, and protons $p\bar{p}$ and $p\bar{p}2\pi$. The generation of the process $e^+e^- \to \mu^+\mu^-\gamma$ is also included into the AFKQED package. For this process both initial and final state radiation (FSR) diagrams and their interference are taken into account. For charged particles the final state radiation is generated using the PHOTOS package (Barberio, van Eijk, and Was, 1991).

The PHOKHARA event generator is used in the *BABAR* and Belle experiments at the $B$ factories, and in the KLOE experiment at the $\phi$ factory. Its latest version 6.1[1] includes generation of the $2\pi$, $3\pi$, $4\pi$, $K\bar{K}$, $p\bar{p}$, and $\Lambda\bar{\Lambda}$ hadronic states, and the process $e^+e^- \to \mu^+\mu^-\gamma$. The initial state radiation is generated in NLO (Rodrigo *et al.*, 2002; Czyż *et al.*, 2003); i.e., one or two photons can be emitted by the initial electron and positron. The generator can be used for simulation of both tagged and untagged ISR measurements. For the processes $e^+e^- \to \mu^+\mu^-\gamma$, $e^+e^- \to \pi^+\pi^-\gamma$, and $e^+e^- \to K^+K^-\gamma$, NLO FSR radiative corrections are implemented. In particular, a hard ISR photon can be accompanied by emission of a soft photon from the final state.

For all hadronic states, except the two-body $2\pi$ and $K\bar{K}$ as well as $\pi^+\pi^-\pi^0$, the structure of the electromagnetic hadronic current entering the matrix element of the process $e^+e^- \to$ hadrons is model dependent and the object of a study by itself. This model dependence is the second source of the theoretical uncertainty. For most of the measurements of multihadron cross sections, its contribution significantly exceeds the 0.5%–1.0% uncertainty of the radiator function. To estimate the model uncertainty, distributions of hadrons in data are compared to the corresponding simulated distributions. Usually, the difference between the detection efficiency obtained with different models of the hadronic currents is taken as an estimate of the model uncertainty.

## II. EXPERIMENTAL TECHNIQUES

### A. Tagged and untagged ISR

There are two approaches for studying ISR events. In the first approach, the untagged one, detection of the ISR photon is not required, but all final hadrons must be detected and

[1] http://ific.uv.es/rodrigo/phokhara/.

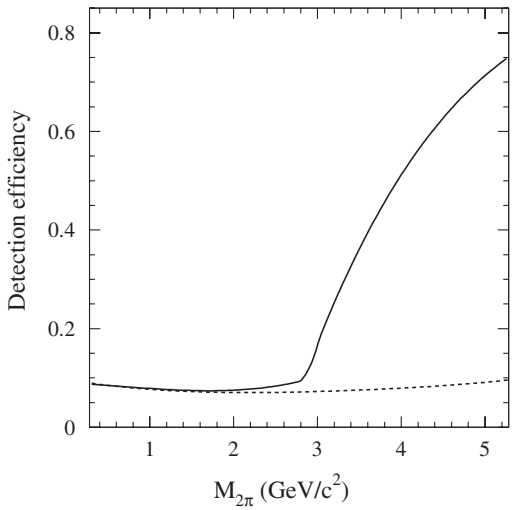


FIG. 6. The detection efficiency for the process $e^+e^- \to \pi^+\pi^-\gamma$ at $2E_0 = 10.58$ GeV as a function of the $2\pi$ invariant mass for untagged (solid curve) and tagged (dotted curve) ISR photons.

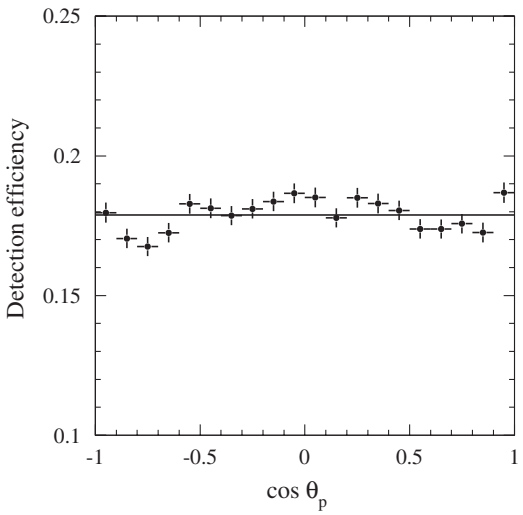


FIG. 7. The $\cos\theta_p$ dependence of the detection efficiency for the process $e^+e^- \to p\bar{p}\gamma$ (Aubert *et al.*, 2006a), where $\theta_p$ is the proton angle measured in the $p\bar{p}$ rest frame with respect to the ISR photon direction. The horizontal line indicates the detection efficiency averaged over $\cos\theta_p$.

fully reconstructed. The ISR events are selected by the requirement that the recoil mass against the hadronic system be close to zero. The mass dependence of the detection efficiency for the process $e^+e^- \to \pi^+\pi^-\gamma$ at $2E_0 = 10.58$ GeV is shown in Fig. 6. The efficiency is calculated with the PHOKHARA event generator in leading-order mode. The detector acceptance for charged pions is assumed to be limited by the condition $30° < \theta < 150°$, which corresponds to the polar-angle coverage of the *BABAR* detector. The solid curve in Fig. 6 represents the efficiency for the case of untagged ISR photons. For two-pion masses below 3 GeV/$c^2$, the detection efficiency is about 10% and changes slowly with mass. At these relatively low invariant masses, pions are produced in a narrow cone around the vector opposite the ISR photon momentum and therefore can be detected only if the ISR photon is emitted at a large angle. The dotted curve in Fig. 6 represents the detection efficiency for the case of a tagged ISR photon. The photon polar angle is required to be in the range of 30° to 150°. It can be seen that tagged and untagged efficiencies are close in the mass range below 3 GeV/$c^2$. For higher masses the small-angle ISR begins to contribute to the untagged efficiency leading to its rapid increase, whereas the efficiency for the case of a tagged ISR photon varies insignificantly.

At *B* factories the untagged approach is used for measurements of exclusive cross sections for masses of produced hadronic systems above 3.5 GeV/$c^2$. The untagged detection efficiency is sensitive to the angular distributions of the final hadrons. Therefore, this approach is suitable for the measurement of hadronic processes with well-defined dynamics, for example, $e^+e^- \to D\bar{D}$ or $e^+e^- \to D^*\bar{D}$. For multihadron final states this strong sensitivity to hadron angular distributions can lead to a sizable systematic uncertainty of the measurement.

All measurements of exclusive cross sections of $e^+e^-$ annihilation into light hadrons at *B* factories were performed using the tagged approach. In contrast to the case of untagged ISR, the efficiency for events with a detected photon depends weakly on the angular distributions of the final hadrons. As an example, the angular dependence of the detection efficiency for the process $e^+e^- \to p\bar{p}\gamma$ (Aubert *et al.*, 2006a) is shown in Fig. 7, where $\theta_p$ is the proton angle in the $p\bar{p}$ rest frame measured with respect to the ISR photon direction. This advantage of the tagged ISR approach allows one to measure the cross section for multihadron final states with a relatively small model uncertainty.

Because ISR photons are emitted predominantly along the beam axis, in untagged ISR measurements the additional condition that $\cos\theta_\gamma$ is close to $\pm 1$ can be used, where $\theta_\gamma$ is the polar angle of the momentum recoil against the hadronic system in the $e^+e^-$ c.m. frame. In particular, Aloisio *et al.* (2005) and Ambrosino *et al.* (2009) used the condition $\theta_\gamma < 15°$ or $\theta_\gamma > 165°$ to select $e^+e^- \to \pi^+\pi^-\gamma$ events at the $\phi$ factory. This condition allows one to significantly reduce background from the decay $\phi \to 3\pi$ and almost completely remove the FSR background, i.e., $e^+e^- \to \pi^+\pi^-\gamma$ events with the photon emitted from the final state. It should be noted that the FSR contribution related to radiation by pions is negligible in *B*-factory experiments due to the smallness of the pion electromagnetic form factor at $s = 112$ GeV$^2$. At this energy, the structure-dependent contribution of the processes $e^+e^- \to f_0\gamma$ and $e^+e^- \to f_2\gamma$ is also expected to be small. Theoretical estimations for the cross sections of these processes at large $s$ are absent in the literature. An estimate was made for the process $e^+e^- \to p\bar{p}$ by Aubert *et al.* (2006a). The FSR contribution (including a structure-dependent part) was found to be less than $10^{-3}$ for the $p\bar{p}$ mass below 4.5 GeV. The detection efficiency for the process $e^+e^- \to \pi^+\pi^-\gamma$ at $2E_0 = 1.02$ GeV with the condition on $\theta_\gamma$ described above is shown in Fig. 8. The pion polar angles are required to be in the range 50°–130°. Because of this restriction the detection efficiency falls rapidly with decreasing $2\pi$ mass. The untagged approach was used by Aloisio *et al.* (2005) and Ambrosino *et al.* (2009) to measure the $e^+e^- \to \pi^+\pi^-$ cross section in

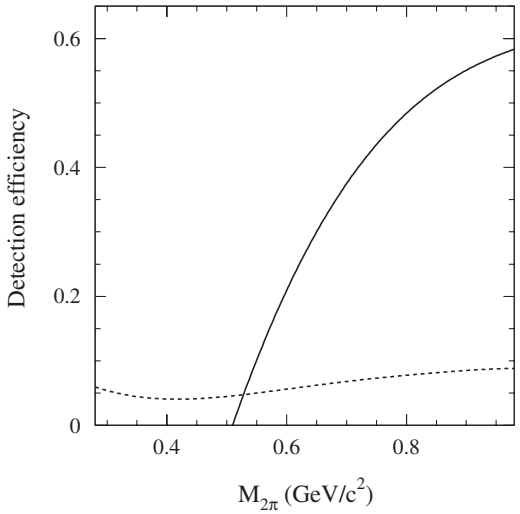


FIG. 8. The mass dependence of the detection efficiency for the process $e^+e^- \to \pi^+\pi^-\gamma$ at $2E_0 = 1.02$ GeV for two selections, untagged ($\theta_\gamma < 15°$ or $\theta_\gamma > 165°$) and tagged ($50° < \theta_\gamma < 130°$), shown by the solid and dashed curves, respectively. The pion polar angles range from 50° to 130°.

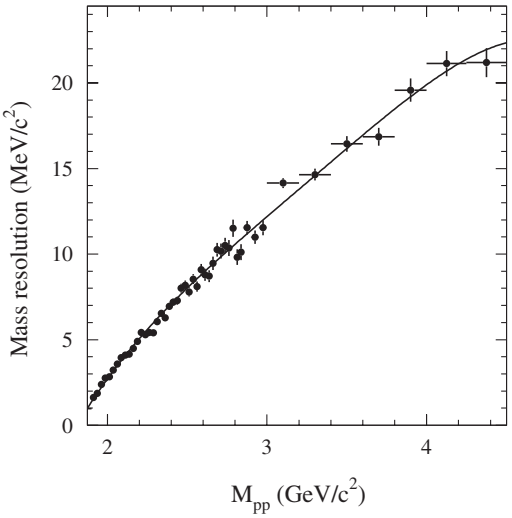


FIG. 9. The mass dependence of the $p\bar{p}$ mass resolution obtained from MC simulation for the process $e^+e^- \to p\bar{p}\gamma$ in Aubert *et al.* (2006a). The curve represents the result of a polynomial fit.

the mass range from 0.592 to 0.975 GeV. The tagged approach allows one to access the near-threshold mass region. The detection efficiency for $\pi^+\pi^-\gamma$ events with a detected photon ($50° < \theta_\gamma < 130°$) is shown in Fig. 8 by the dashed curve. This selection was also used in the KLOE experiment (Muller, 2010; Ambrosino *et al.*, 2011) and allowed one to reduce the lower mass boundary for the cross section measurement from 0.592 to 0.316 GeV.

### B. Hadronic mass resolution and mass scale calibration

The detector resolution on the hadronic invariant mass and the accuracy of the mass scale calibration are important experimental parameters for the ISR cross section measurements. The mass resolution $\sigma_m$ is usually determined using MC simulation as rms of the $m_{\rm meas} - m_{\rm true}$ distribution, where $m_{\rm meas}$ and $m_{\rm true}$ are the measured and generated invariant masses, respectively. The experimental value of the mass resolution can be extracted from the fit of the measured line shape of a narrow resonance, for example, $J/\psi$.

In general, the invariant mass can be represented as a sum of the two terms $m_{\rm meas} = \Sigma_i m_i + \Delta m(\vec{p}_1, \vec{p}_2, \ldots)$, where $m_i$ are masses of stable hadrons produced in the process under study, and $\Delta m$ is the term depending on the final particle momenta $\vec{p}_i$. The mass resolution $\sigma_m$ is determined from the precision of the measurement of the momenta of the charged hadron tracks and photons from $\pi^0$ decays. Since $\Sigma_i m_i$ has no sizable spread, and the $\Delta m$ term and its uncertainty are minimal near threshold and grow with the mass increase, it is expected that $\sigma_m$ also increases with mass. As an example, the mass resolution versus the proton-antiproton mass for the ISR process $e^+e^- \to p\bar{p}\gamma$ (Aubert *et al.*, 2006a) is shown in Fig. 9.

At $B$ factories the mass resolution for multihadron systems consisting of light quarks varies from 4–7 MeV/$c^2$ at the mass of 1.5 GeV/$c^2$ to 6–11 MeV/$c^2$ at 3 GeV/$c^2$; the worse values are for hadron states with neutral pions. The hadronic cross sections in the mass region between the $\phi$- and $J/\psi$-meson resonances do not contain structures with a width comparable to the detector resolution. The 25-MeV/$c^2$ mass bin was chosen for a study of most of the processes with light hadrons. With such a bin size the distortion of the mass spectrum due to resolution effects is small. A smaller bin size was used for analyses of the processes $e^+e^- \to p\bar{p}\gamma$ and $e^+e^- \to \pi^+\pi^-\gamma$. For the former, it is important to study a near-threshold enhancement in the mass dependence of the proton electromagnetic form factor. The good $p\bar{p}$ mass resolution for masses below 2 GeV/$c^2$ (see Fig. 9) allows one to measure the cross section in this region with the 5 MeV/$c^2$ mass bin (Aubert *et al.*, 2006a). The $e^+e^- \to \pi^+\pi^-$ cross section near the $\rho$-meson peak was measured in the *BABAR* experiment with a mass interval of 2 MeV/$c^2$ (Aubert *et al.*, 2009a), which is significantly smaller than the $\pi^+\pi^-$ mass resolution (about 6 MeV/$c^2$ at the $\rho$ peak). The unfolding of resolution effects from the high-statistics (about 500 000 events) mass spectrum was performed with the procedure described by Malaescu (2009). The procedure used a mass-transfer matrix that gives the probability that an event with true mass in an interval $i$ is reconstructed with $m_{\rm meas}$ in the interval $j$. The transfer matrix is usually obtained using MC simulation and corrected to take into account a difference in the resolution between data and simulation.

The measurement of the $e^+e^- \to \pi^+\pi^-$ cross section at the $\phi$ factory (Ambrosino *et al.*, 2009) with the KLOE detector was performed with a 0.01 GeV$^2$ step in the squared mass $s' = m^2_{2\pi}$ corresponding to a mass bin width of 6.5 MeV/$c^2$ near the $\rho$ peak. The mass resolution of the KLOE detector is about 1.3 MeV/$c^2$ at the $\rho$ mass. The resolution effects are substantial only in the mass region of the $\omega$-$\rho$ interference. For comparison with theory, these effects were removed by unfolding the mass spectrum using the Bayesian method (D'Agostini, 1995).

For the $J/\psi$ and $\psi(2S)$ produced in ISR processes the observed line shapes are fully determined by the detector resolution. In this case better mass resolution leads to the

larger signal-to-background ratio. For the process $e^+e^- \to 2(\pi^+\pi^-)\pi^0\gamma$ (Aubert *et al.*, 2007c) in the mass region of the $J/\psi$ and $\psi(2S)$ mesons discussed in Sec. V, the value of the mass resolution obtained from the fit to the $J/\psi$ spectrum is about 9 MeV/$c^2$, in good agreement with MC simulation.

For the final states containing charmed and charmonium mesons ($J/\psi\pi^+\pi^-$, $D\bar{D}$, etc.), the typical resolution in the 4–5 GeV/$c^2$ mass range is about 5 MeV/$c^2$. The corresponding cross sections were measured with the 20–25 MeV/$c^2$ mass bin. For these final states the influence of the limited mass resolution on the cross section measurement is negligible.

The precision of the absolute mass scale calibration can be tested by comparison of the measured mass values for known resonances with their nominal values. For many multihadron states (see Sec. V) the mass calibration is performed at the $J/\psi$ mass. The difference between the measured and nominal (Eidelman *et al.*, 2004) $J/\psi$ masses is found to be less than 1 MeV/$c^2$ [see, for example, Aubert *et al.* (2007c, 2008b)]. For the $3\pi$ final state the mass scale shift was determined at the $\omega$- and $\phi$-meson masses (Aubert *et al.*, 2004b) $m_\omega - m_\omega^{\text{nominal}} = -(0.2 \pm 0.1)$ MeV/$c^2$ and $m_\phi - m_\phi^{\text{nominal}} = -(0.6 \pm 0.2)$ MeV/$c^2$. We conclude that for the measurements of hadronic cross sections at $B$ factories the mass scale is defined with a relative accuracy better than or about $5 \times 10^{-4}$.

### C. ISR luminosity

It is clear that radiation of a hard photon significantly decreases the cross section, so the ISR technique can be efficient at high-luminosity colliders only. To compare the effectiveness of the ISR method for the measurement of hadronic cross sections with direct $e^+e^-$ experiments, it is useful to introduce the concept of ISR luminosity. The mass spectrum for the ISR process $e^+e^- \to X\gamma$ is expressed in terms of the ISR differential luminosity $dL/dm$ and the Born cross section for the process $e^+e^- \to X$ as

$$\frac{dN}{dm} = \varepsilon(m)[1 + \delta(m)]\sigma_0(m)\frac{dL}{dm}, \tag{9}$$

where $1 + \delta(m) = W(m)/W_0(m)$ is the radiative correction factor discussed in Sec. I.C. The ISR luminosity is proportional to the total integrated luminosity $L$ collected in an experiment and the lowest-order radiator function given by Eqs. (7) or (8) depending on the angular range used for determination of the detection efficiency $\varepsilon(m)$:

$$\frac{dL}{dm} = W_0(m)\frac{2m}{s}L. \tag{10}$$

The mass dependence of the ISR differential luminosity multiplied by the detection efficiency for the *BABAR* experiment is shown in Fig. 10 for masses below 2.2 GeV/$c^2$. The detection efficiency used was calculated in Sec. II.A for the process $e^+e^- \to \pi^+\pi^-\gamma$ with a tagged ISR photon. The integrated luminosity is taken to be 500 fb$^{-1}$. The dashed curve in Fig. 10 shows the same quantity calculated for the KLOE experiment with an integrated luminosity of 240 pb$^{-1}$ and detection efficiency taken for the case of an untagged ISR photon (see Fig. 8). A luminosity of 240 pb$^{-1}$ was used in the

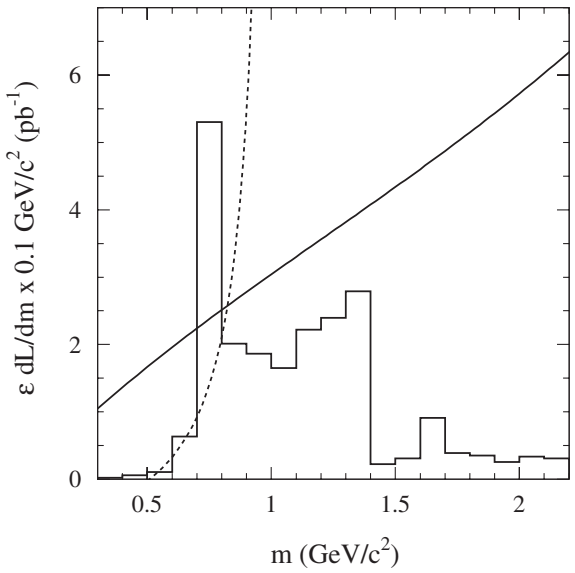


FIG. 10. The mass dependence of the ISR differential luminosity multiplied by the detection efficiency. The solid curve shows $\varepsilon dL/dm$ for the $B$ factory ($2E_0 = 10.58$ GeV, $L = 500$ fb$^{-1}$, tagged ISR photon), while the dashed curve shows the same function for the $\phi$ factory ($2E_0 = 1.02$ GeV, $L = 240$ pb$^{-1}$, untagged ISR photon). The histogram represents integrated luminosities collected in direct $e^+e^-$ experiments with the SND detector (Achasov *et al.*, 2002) at the Novosibirsk VEPP-2M collider (below 1.4 GeV/$c^2$), and with the DM1 (Bisello *et al.*, 1981) and DM2 (Antonelli *et al.*, 1992) detectors at the Orsay DCI collider (above 1.4 GeV/$c^2$).

recent measurement (Ambrosino *et al.*, 2009) of the $e^+e^- \to \pi^+\pi^-$ cross section in the 0.592–0.975 GeV/$c^2$ mass range. The total integrated luminosity collected by the KLOE experiment is about an order of magnitude larger, 2.5 fb$^{-1}$. The KLOE ISR luminosity is shown only up to 0.92 GeV/$c^2$. It increases sharply and reaches 21 pb$^{-1}$ at 0.975 GeV/$c^2$. It should be noted that the *BABAR* measurement of the $e^+e^- \to \pi^+\pi^-$ cross section (Aubert *et al.*, 2009a) is also based on a part of the recorded data corresponding to 232 fb$^{-1}$. The histogram in Fig. 10 shows the distribution of the integrated luminosities collected in some direct $e^+e^-$ experiments. At masses below 1.4 GeV/$c^2$ the statistics of the SND experiment (Achasov *et al.*, 2002) recorded at the VEPP-2M collider is presented. This is the largest integrated luminosity collected in this mass region in a single experiment. The mass bin 1.0–1.1 GeV/$c^2$ does not include about 13 pb$^{-1}$ taken by SND in the vicinity of the $\phi$-meson resonance. The significant part of the statistics from the 0.7–0.8 GeV/$c^2$ mass interval is collected in the $\omega$-meson mass window 0.76–0.80 GeV/$c^2$. In the c.m. energy range 1.4–2.2 GeV/$c^2$ the experiments with the largest statistics are DM1 and DM2 at the Orsay $e^+e^-$ collider DCI. The histogram at $m > 1.4$ GeV/$c^2$ shows a sum of the integrated luminosities collected with these detectors.

At low masses of the hadronic system the data samples of ISR events currently available at $B$ factories exceed the statistics collected in conventional $e^+e^-$ experiments, especially at masses below 0.7 and above 1.4 GeV/$c^2$. The ISR luminosity of the $\phi$ factory increases rapidly with mass. For

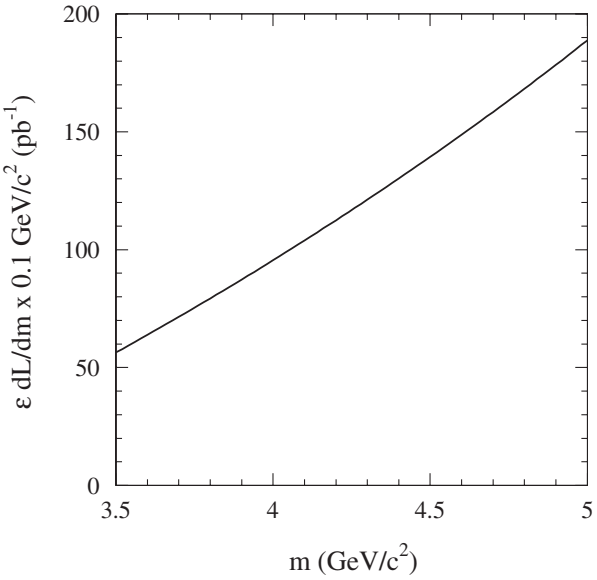


FIG. 11. The mass dependence of the ISR differential luminosity multiplied by the detection efficiency for experiments at the $B$ factory ($2E_0 = 10.58$ GeV, $L = 500$ fb$^{-1}$, untagged ISR photon) in the charm production mass region.

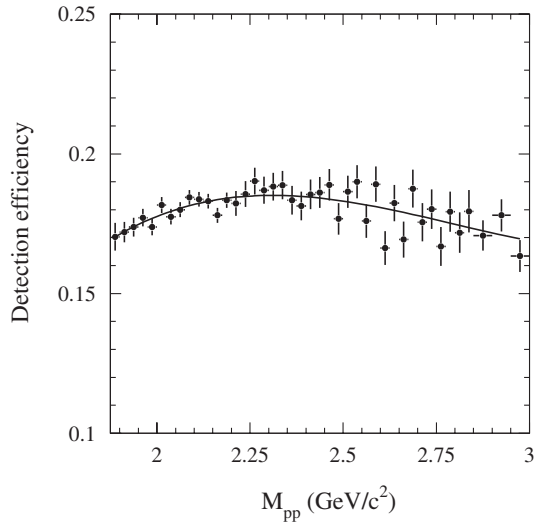


FIG. 12. The detection efficiency for the process $e^+e^- \to p\bar{p}\gamma$ (Aubert *et al.*, 2006a) as a function of the $p\bar{p}$ invariant mass. The curve represents the result of a polynomial fit.

masses below 0.8 GeV/$c^2$ the luminosity currently used for ISR analysis (Ambrosino *et al.*, 2009) is comparable with that collected in direct $e^+e^-$ experiments. For higher masses it exceeds both *BABAR* and $e^+e^-$ luminosities.

The ISR luminosity for the mass region of charm production is shown in Fig. 11. It corresponds to the 500 fb$^{-1}$ integrated luminosity collected at $2E_0 = 10.58$ GeV/$c^2$ and is multiplied by the detection efficiency calculated for the case of an untagged ISR photon (see Fig. 6). The ISR luminosity in this mass region significantly exceeds the integrated luminosity collected in direct $e^+e^-$ experiments including the recent CLEO-c energy scan (Cronin-Hennessy *et al.*, 2009), 60 pb$^{-1}$ at 12 points between 3.97 and 4.26 GeV.

Thus, the current data samples of ISR events produced at the $B$ and $\phi$ factories are larger than those produced directly in $e^+e^-$ collisions for all masses of interest excluding the regions near the narrow resonances [$\omega$, $\phi$, $J/\psi$, and $\psi(2S)$]. For masses above 1.4 GeV/$c^2$ this allows one to significantly improve accuracy of the measurements of exclusive hadronic cross sections. In the mass region below 1.4 GeV/$c^2$ the results obtained with the ISR method are comparable to rather precise direct $e^+e^-$ measurements.

### D. Comparison with $e^+e^-$ scan

The ISR technique offers some advantages over conventional $e^+e^-$ measurements. One of them is that the entire hadronic mass range is accessible in one experiment. This allows one to avoid relative normalization uncertainties which inevitably arise when data from different experiments, or from different machine settings in one experiment, are combined.

The ISR measurements with a tagged photon have additional advantages. In many cases, particularly for final states with low invariant mass of the produced particles, the hadronic system is collimated along the direction opposite to the ISR photon. Therefore, the detection efficiency has low sensitivity to hadron angular distributions in the hadronic-system rest frame. In Fig. 7 the angular dependence of the detection efficiency is shown for the process $e^+e^- \to p\bar{p}\gamma$ (Aubert *et al.*, 2006a). The angular dependence is close to uniform. This reduces the model dependence of the cross section measurement due to the unknown relation between the values of the proton electric and magnetic form factors and significantly facilitates data analysis. Note that in conventional experiments at $e^+e^-$ or $p\bar{p}$ colliders the detector acceptance for the final $p\bar{p}$ or $e^+e^-$ systems falls to zero when $\cos\theta_p$ approaches $\pm 1$.

For ISR events the final hadrons have nonzero momenta at the production threshold and are therefore detected with full efficiency. In Fig. 12 the detection efficiency for the process $e^+e^- \to p\bar{p}\gamma$ (Aubert *et al.*, 2006a) is shown as a function of the $p\bar{p}$ invariant mass. No strong variation of the efficiency with mass is observed, while in direct $e^+e^-$ measurements the detection efficiency vanishes at the threshold because of the low momenta of the produced particles. This feature of ISR hadron production was successfully used at *BABAR* for the measurements of the $e^+e^- \to p\bar{p}$ (Aubert *et al.*, 2006a) and $e^+e^- \to \pi^+\pi^-$ (Aubert *et al.*, 2009a) cross sections in near-threshold mass regions.

For the measurement of the $e^+e^- \to \pi^+\pi^-$ cross section, particle identification plays a crucial role. In the ISR process $e^+e^- \to \pi^+\pi^-\gamma$ at $B$ factories most of the final pions have momenta larger than 1 GeV/$c$. For such pion momenta a good $\pi$-$\mu$-$e$ separation is provided which allows one to almost completely remove the $e^+e^- \to e^+e^-\gamma$ and $e^+e^- \to \mu^+\mu^-\gamma$ backgrounds (Aubert *et al.*, 2009a). This is in contrast with direct $e^+e^-$ measurements (Akhmetshin *et al.*, 2004a, 2007; Achasov *et al.*, 2006) in which it is difficult to separate $e^+e^- \to \pi^+\pi^-$ and $e^+e^- \to \mu^+\mu^-$ events in the most interesting $\rho$-meson mass region (0.60–0.95 GeV). As a result, a sum of the cross sections is measured. The contribution from the process $e^+e^- \to \mu^+\mu^-$ is then subtracted using its theoretically calculated

cross section. This leads to an increase of statistical and systematic errors of the measurement.

It should be noted that the advantages of tagged ISR discussed above (weak mass and angular dependences of the detection efficiency) are completely absent for untagged ISR. In this case the mass and angular dependences are even stronger than those for events of direct $e^+e^-$ annihilation.

A disadvantage of ISR is that the mass resolution and absolute mass scale calibration are much poorer than the beam energy spread and the accuracy of the beam energy setting in direct $e^+e^-$ annihilation experiments. The influence of the resolution effects on the ISR measurement is discussed in Sec. II.B.

The main disadvantage of the ISR measurements is the presence of a wide spectrum of background processes different from those in direct $e^+e^-$ experiments. For example, in $e^+e^-$ annihilation the main background process for $e^+e^- \to \pi^+\pi^-\pi^0$ is $e^+e^- \to \pi^+\pi^-\pi^0\pi^0$ with a lost $\pi^0$. For the ISR process $e^+e^- \to \pi^+\pi^-\pi^0\gamma$ with the $3\pi$ mass in the range $m_{3\pi} \pm \Delta m/2$, this background corresponds to a contribution of the process $e^+e^- \to \pi^+\pi^-\pi^0\pi^0\gamma$ with the $4\pi$ mass in the same range $m_{3\pi} \pm \Delta m/2$. The presence in ISR of $4\pi\gamma$ events with arbitrary masses, which may, in particular, be out of the $m_{3\pi} \pm \Delta m/2$ range, greatly increases background.

At the $\phi$ factory and in future ISR measurements at the tau-charm factory in Beijing the background from FSR processes should be taken into account when the ISR photon is detected. The FSR contribution to the $e^+e^- \to \pi^+\pi^-$ measurements at KLOE is calculated with the PHOKHARA generator, which models FSR for pions using scalar QED, and also takes into account the radiative $\phi$ decays to $\pi^+\pi^-\gamma$ via the $f_0(980)\gamma$ and $\rho\pi$ intermediate states. The pion electromagnetic form factor used in the generator is obtained from a fit to the $e^+e^- \to \pi^+\pi^-$ experimental data. In the case of the tau-charm factory, experimental information on exclusive hadronic cross sections in the energy range from 3.0 to 4.5 GeV obtained at $B$ factories can be used to estimate the FSR contribution. Additional theoretical input is required to estimate structure-dependent FSR.

Another background source is the non-ISR process of $e^+e^-$ annihilation into hadrons containing a high-energy $\pi^0$. In particular, the events of the $e^+e^- \to X\pi^0$ process with an undetected soft photon or merged photons from the $\pi^0$ decay may almost completely imitate the $e^+e^- \to X\gamma$ events. This background is usually subtracted statistically using for normalization selected $e^+e^- \to X\pi^0$ events with a reconstructed $\pi^0$. In tagged ISR measurements at $B$ factories the $e^+e^- \to X\pi^0$ process becomes the dominant background source at relatively high masses, about 2 GeV/$c^2$. It limits the mass region for ISR studies of light hadrons to masses below 4.0–4.5 GeV/$c^2$.

In ISR measurements with an untagged ISR photon, the background from $e^+e^- \to X\pi^0$ can be significantly suppressed by requiring that the missing momentum in an event be directed along the beam axis. For untagged ISR, the main sources of background are ISR processes and two-photon processes $e^+e^- \to e^+e^-\gamma^*\gamma^* \to e^+e^-X$ in which an initial electron and positron are scattered predominantly at small angles. The latter background can be suppressed by a condition on the missing mass, which should be close to zero for ISR events and has a wide distribution for two-photon events.

Background suppression and subtraction are the main sources of the systematic uncertainty on ISR measurements.

### E. Colliders and detectors using ISR

ISR processes were studied in many $e^+e^-$ experiments either as a source of useful physical information or as a source of background. For example, possibly the first study of the process $e^+e^- \to \pi^+\pi^-\gamma$ was performed more than 20 years ago with the ND detector at the VEPP-2M collider (Vasserman *et al.*, 1988; Dolinsky *et al.*, 1991). In this work, the FSR process $e^+e^- \to \rho \to \pi^+\pi^-\gamma$ was measured with the ISR process $e^+e^- \to \rho\gamma \to \pi^+\pi^-\gamma$ studied as a main source of background. Many interesting ISR studies have been performed with the CLEO detector; see, e.g., Adams *et al.* (2006). Below we give a brief description of only three detectors: *BABAR*, Belle, and KLOE, which made a great contribution to both development of the ISR technique and ISR measurements of hadronic cross sections.

### F. PEP-II and *BABAR*

The PEP-II $B$ factory at SLAC is a two-ring asymmetric-energy $e^+e^-$ collider with energies of 9 GeV for the electron and 3.1 GeV for the positron beam, operating at the c.m. energy of 10.58 GeV, at the maximum of the $\Upsilon(4S)$ resonance (Seeman *et al.*, 2001). The maximum luminosity achieved at PEP-II was slightly over $10^{34}$ cm$^{-2}$ s$^{-1}$. The principal goal of the PEP-II $B$ factory and the *BABAR* detector is studies of $CP$ violation in the $B$-meson system.

The *BABAR* detector (see Fig. 13) is described in detail elsewhere (Aubert *et al.*, 2002). Final states with charged particles are reconstructed in the *BABAR* tracking system, which comprises a five-layer silicon vertex tracker (SVT) and a 40-layer drift chamber (DCH) operating in a 1.5-T axial magnetic field. The vertex position is measured by the SVT

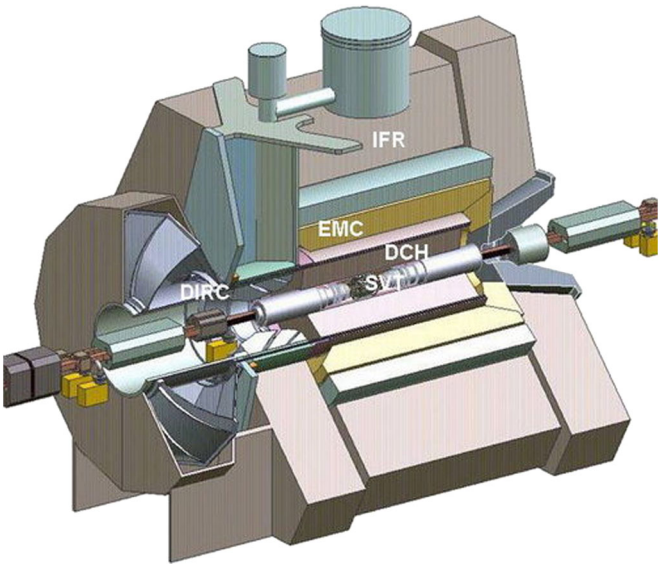


FIG. 13 (color online). View of the *BABAR* detector.

with the accuracy of 50 $\mu$m. The momentum resolution for 1 GeV/$c$ charged tracks is $\sigma_{p_t}/p_t = 0.5\%$. Charged-particle identification is provided by an internally reflecting ring-imaging Cherenkov detector (DIRC), and by energy loss measurements in the SVT and DCH. The hard ISR photon and photons from $\pi^0$ decays are detected in a CsI(Tl) electromagnetic calorimeter (EMC). The energy resolution for 1 GeV photons is about 3%; the angles of photons are measured with the 4 mrad accuracy. Muons are identified in the instrumented flux return (IFR) of the solenoid, which consists of iron plates interleaved with resistive plate chambers.

Experiments at the PEP-II collider with the *BABAR* detector were carried out from 1999 to 2008. The total integrated luminosity is close to 530 fb$^{-1}$. The ISR studies at *BABAR* started in 2001. The ISR research program includes a study of the light hadron production with a tagged ISR photon and charm and charmonium studies with an untagged photon.

### G. KEK-B and BELLE

The KEK $B$ factory, KEK-B, is an asymmetric-energy (similar to PEP-II) $e^+e^-$ collider with the 8-GeV electron and 3.5-GeV positron beams and a maximum luminosity of $2.1 \times 10^{34}$ cm$^{-2}$ s$^{-1}$ (Kurokawa and Kikutani, 2003). The main physical goal of this project is to perform a detailed study of $B$-meson properties, in particular, $CP$ violation.

The Belle detector (Abashian *et al.*, 2002) is configured inside a 1.5 T superconducting solenoid (see Fig. 14). The $B$-meson vertices are measured in a three-layer double-sided silicon vertex detector with about 50 $\mu$m impact parameter resolution for 1 GeV/$c$ momentum track at $\theta \simeq \pi/2$. Track momenta are measured in a 50-layer wire drift chamber with a 0.4% momentum resolution at 1 GeV/$c$. Particle identification is provided by $dE/dx$ measurements in the drift chamber, aerogel Cherenkov counters, and time-of-flight counters placed outside the drift chamber. Electromagnetic showers are detected in a CsI(Tl) calorimeter located inside the solenoid coil. The energy resolution is 2% for 1-GeV photons. An iron flux return located outside the coil is instrumented to detect $K_L$ mesons and identify muons.

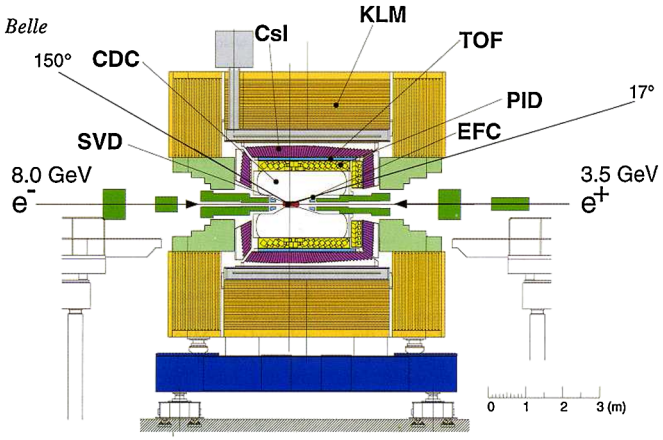


FIG. 14 (color online). Side view of the Belle detector.

Experiments with Belle started in 2000 and stopped in 2010. The Belle integrated luminosity reaches 1000 fb$^{-1}$. The ISR experiments are mainly devoted to the production of charm and charmonium hadronic states with mass above 4 GeV/$c^2$. ISR analysis of light mesons is in progress.

### H. DAΦNE and KLOE

DAΦNE, the Frascati $\phi$ factory (Franzini and Moulson, 2006), has been in operation since 1999. The main goal of the DAΦNE project is a study of neutral and charged kaons, intensively produced at the energy corresponding to the maximum of $\phi(1020)$ resonance. Similar to PEP-II and KEK-B, DAΦNE uses two separate rings for storing electron and positrons, but beams have equal energies. The DAΦNE design luminosity is $5 \times 10^{32}$ cm$^{-2}$ s$^{-1}$.

KLOE (Franzini and Moulson, 2006) is the main DAΦNE detector (see Fig. 15). The detector consists of a large-volume drift chamber surrounded by a hermetic EMC. A superconducting coil provides an axial magnetic field of 0.52 T. In order to reduce neutral kaon regeneration and charged-particle multiple scattering, the gas mixture of 90% helium and 10% isobutane is used in the drift chamber. Charged-track momenta are measured with $\sigma_p/p = 0.4\%$ accuracy. The lead-scintillation fiber calorimeter provides the energy resolution for electromagnetic showers of $\sigma_E/E = 5.7\%/\sqrt{E(\mathrm{GeV})}$, and the time resolution of $\sigma_t = 54\ \mathrm{ps}/\sqrt{E(\mathrm{GeV})} \oplus 140$ ps.

The total integrated luminosity accumulated with KLOE is about 3 fb$^{-1}$. The only, but important, ISR process studied at KLOE is $e^+e^- \to \pi^+\pi^-\gamma$.

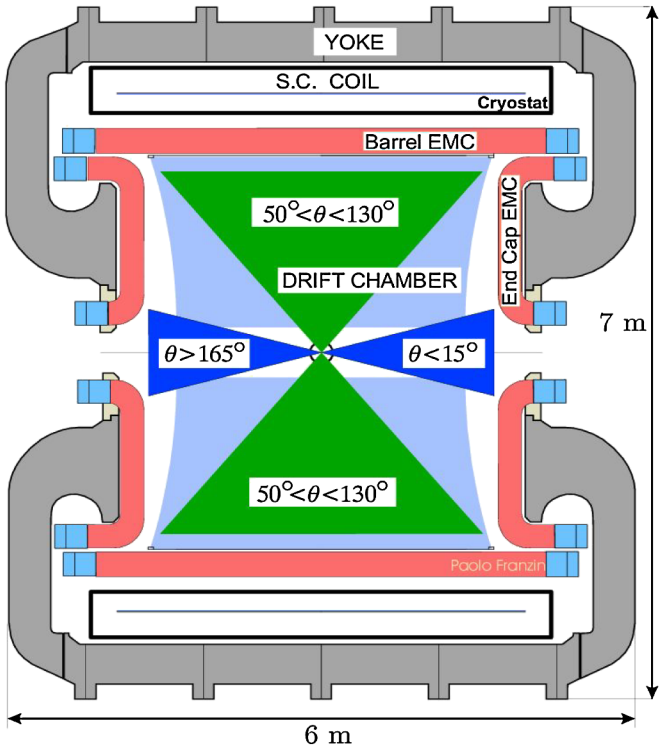


FIG. 15 (color online). KLOE detector (Muller, 2010). The polar-angle regions used to select tagged ($50° < \theta_\gamma < 130°$) and untagged ($\theta_\gamma < 15°$ or $\theta_\gamma > 165°$) ISR events are shown.

## III. PRODUCTION OF LIGHT QUARK MESONS

### A. Overview

As mentioned in the Introduction, $e^+e^-$ annihilation into hadrons at c.m. energies below 2 GeV plays an important role in many fundamental problems of particle physics. In particular, knowledge of its total cross section is mandatory for the calculation of the muon anomalous magnetic moment in the standard model (SM). For many years only $e^+e^-$ scan experiments provided information on this reaction and determined the uncertainty of the SM prediction of the muon anomaly (Davier *et al.*, 2003a, 2003b). The main information on light vector mesons has also been obtained in such measurements. Unfortunately, the collected data samples were not sufficient for a precise determination of parameters of excited vector mesons. Recently, due to a high luminosity of the $e^+e^-$ factories, DAΦNE, KEK-B, and PEP-II, the ISR technique became a powerful tool for an independent study of $e^+e^-$ annihilation at low energies.

The KLOE Collaboration used the ISR method at the $\phi$ meson energy to study the reaction $e^+e^- \to \pi^+\pi^-$ and measure the pion electromagnetic form factor (Aloisio *et al.*, 2005; Ambrosino *et al.*, 2009, 2011; Muller, 2010). Recently, results on this process were also reported by the *BABAR* Collaboration (Aubert *et al.*, 2009a).

A variety of high-multiplicity final states were studied at *BABAR*: $\pi^+\pi^-\pi^0$ (Aubert *et al.*, 2004b); $2(\pi^+\pi^-)$, $\pi^+\pi^-K^+K^-$, and $2(K^+K^-)$ (Aubert *et al.*, 2005b); $3(\pi^+\pi^-)$, $2(\pi^+\pi^-\pi^0)$, and $K^+K^-2(\pi^+\pi^-)$ (Aubert *et al.*, 2006b); $2(\pi^+\pi^-)\pi^0$, $2(\pi^+\pi^-)\eta$, $K^+K^-\pi^+\pi^-\pi^0$, and $K^+K^-\pi^+\pi^-\eta$ (Aubert *et al.*, 2007c); $K^+K^-\pi^+\pi^-$ and $K^+K^-\pi^0\pi^0$ (Aubert *et al.*, 2007b); $K^+K^-\pi^+\pi^-$, $K^+K^-\pi^0\pi^0$, and $K^+K^-K^+K^-$ (Aubert *et al.*, 2007b); and $K^\pm K_S^0\pi^\mp$, $K^+K^-\pi^0$, and $K^+K^-\eta$ (Aubert *et al.*, 2008b). The final $K^+K^-\pi^+\pi^-$ state was also investigated by Belle (Shen *et al.*, 2009).

Studies of the exclusive channels of $e^+e^-$ annihilation listed above allow one to determine such fundamental parameters such as mass, width, and leptonic width of various vector mesons. In addition to the low-lying resonances, such as $\rho$, $\omega$, and $\phi$, where ISR studies can independently provide meaningful and competitive information, they are indispensable for a much-more-precise-than-before investigation of the excited vector states.

Moreover, a detailed analysis of the dynamics shows that in many cases a multiparticle final state can be reached via different intermediate mechanisms. For example, four pions can be produced via $\omega\pi^0$, $a_1(1260)\pi$, $\rho^0 f_0$, etc. In the following sections we show a complexity of the internal substructures observed in some channels, which are often used to extract parameters of the resonances involved in the substructures.

In general, amplitudes corresponding to different intermediate mechanisms interfere, affecting the energy and angular distributions of the final particles. This interference should be taken into account to avoid additional systematic errors.

Unless otherwise stated, all cross sections in the following sections are corrected for effects of initial state radiation only. Neither final state radiation nor vacuum polarization corrections have been applied.

### B. $e^+e^- \to \pi^+\pi^-$

The reaction $e^+e^- \to \pi^+\pi^-$ was relatively well studied for c.m. energies up to 1.4 GeV in direct $e^+e^-$ experiments. The most precise measurements were performed with the CMD-2 (Akhmetshin *et al.*, 2004a, 2007) and SND (Achasov *et al.*, 2006) detectors at the VEPP-2M collider. The CMD-2 measurements have a systematic uncertainty in the 1% range.

The dominant contribution to this process comes from the $\rho(770)$ meson production. A measurement of the $e^+e^- \to \pi^+\pi^-$ cross section in the $\rho(770)$ mass region was performed by KLOE using the ISR method (Aloisio *et al.*, 2005; Ambrosino *et al.*, 2009, 2011; Muller, 2010). For the first time it was demonstrated that the cross section determined by this method could have smaller statistical errors than direct $e^+e^-$ measurements and could be competitive with them in a systematic uncertainty. Both untagged (Aloisio *et al.*, 2005; Ambrosino *et al.*, 2009) and tagged (Muller, 2010; Ambrosino *et al.*, 2011) ISR $\pi^+\pi^-\gamma$ events were studied with consistent results. While the tagged measurement has worse statistical errors and an additional source of the systematic uncertainty due to the FSR contribution, it covers the region of small invariant masses inaccessible for the untagged measurement. The result of the tagged measurement (Muller, 2010; Ambrosino *et al.*, 2011) represented as a pion electromagnetic form factor squared is shown in Fig. 16 (top) together with the results of the direct $e^+e^-$ measurements with the CMD-2 (Akhmetshin *et al.*, 2007) and SND (Achasov *et al.*, 2006) detectors. Comparison of the more precise untagged KLOE measurement (Ambrosino *et al.*, 2009) with the CMD-2 and SND data is given in Fig. 16 (bottom). At invariant masses corresponding to the maximum of the $\rho$ resonance and its high-mass tail the points from direct $e^+e^-$ measurements lie systematically higher than those from KLOE. In this mass region the difference between the CMD-2 and KLOE measurements is definitely larger than their combined systematic uncertainty. The KLOE systematic error includes the experimental (0.6%) and theoretical (0.6%) uncertainties. Two main sources of the former are tracking and luminosity measurement. The latter is determined mostly by the accuracy of the radiator function calculated with the PHOKHARA event generator. Note that the KLOE Collaboration performed a dedicated study to validate a calculation of FSR effects using forward-backward asymmetry arising from the interference between the ISR and FSR amplitudes (Muller, 2010). The study showed that the assumption of pointlike pions works reasonably well and can be used for the FSR calculation; see Fig. 17.

A structure seen at the top of the $\rho$-meson resonance is due to its interference with the much more narrow $\omega(782)$ resonance also decaying to $\pi^+\pi^-$. Because the $\omega(782)$ mass is known precisely, the position of this structure can be used to test the accuracy of the mass scale calibration. Unfortunately, neither KLOE nor *BABAR* (see below) reported the result of such a test.

The PEP-II $B$ factory also provided a large sample of the $e^+e^- \to \pi^+\pi^-\gamma$ events (about 530 000) and the

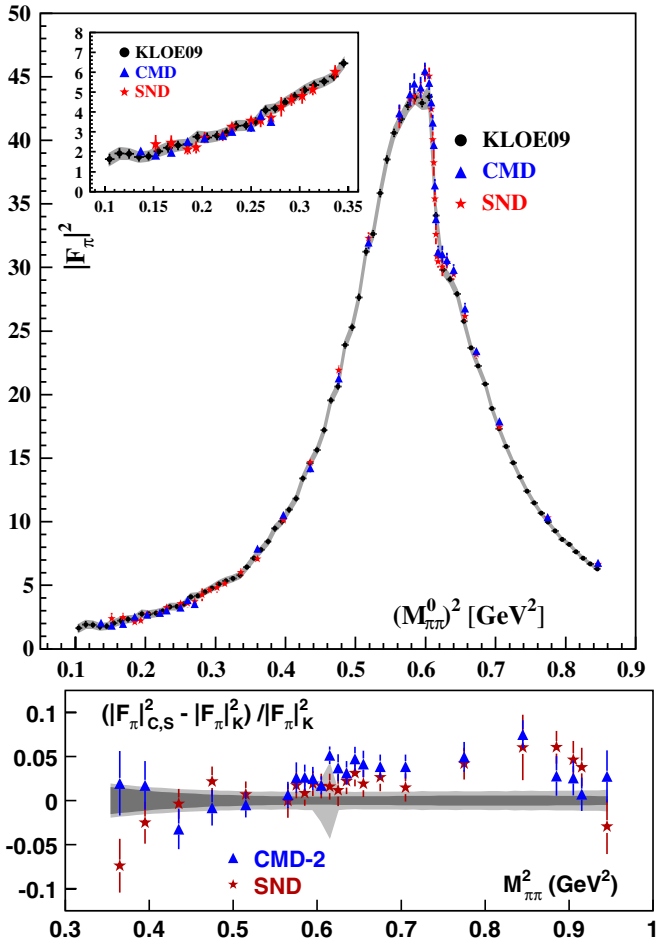


FIG. 16 (color online). Top: The pion form factor obtained by KLOE in the reaction $e^+e^- \to \pi^+\pi^-\gamma$ with a tagged ISR photon (Muller, 2010). Bottom: Relative difference between the KLOE result with an untagged ISR photon (Ambrosino *et al.*, 2009) and the direct $e^+e^-$ measurements by SND (Achasov *et al.*, 2006) and CMD-2 (Akhmetshin *et al.*, 2007). The dark (light) band indicates the KLOE uncertainty (statistical and systematic errors combined in quadrature). For the SND and CMD-2 data, the combined statistical and systematic errors are shown.

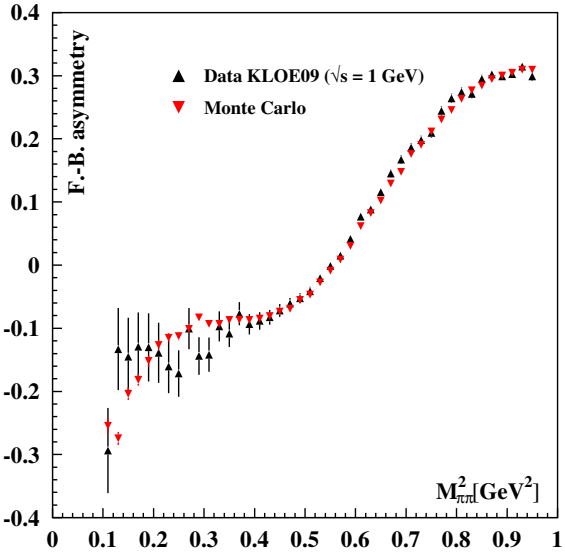


FIG. 17 (color online). Forward-backward asymmetry in the reaction $e^+e^- \to \pi^+\pi^-(\gamma)$ measured with the KLOE detector. From Muller, 2010.

$e^+e^- \to \pi^+\pi^-$ cross section (Aubert *et al.*, 2009a) was measured for the $e^+e^-$ c.m. energies up to 3.0 GeV. In this experiment the $e^+e^- \to \pi^+\pi^-$ cross section is obtained from the ratio of the $\pi^+\pi^-$ and $\mu^+\mu^-$ mass spectra. Because of the normalization to the cross section of the theoretically well-known process $e^+e^- \to \mu^+\mu^-\gamma$, the measurement becomes much less sensitive to the experimental uncertainties and to the theoretical uncertainty of the radiator function. A comparison of the measured $\mu^+\mu^-$ mass spectrum for the reaction $e^+e^- \to \mu^+\mu^-\gamma$ with the QED prediction is shown in Fig. 18 (top). The data and the prediction are consistent within the estimated systematic uncertainty of 1.1%, dominated by the accuracy of the integrated luminosity measurement. Using the bin-by-bin ratio to the cross section of the process $e^+e^- \to \mu^+\mu^-\gamma$, one minimizes theoretical uncertainties and reduces a systematic error at the $\rho$ peak to 0.5% dominated by pion identification and ISR luminosity. Previously such a test was performed in $e^+e^-$ scan experiments at the OLYA detector in the c.m. energy range from 640 to 1400 MeV (Kurdadze *et al.*, 1984) and at the CMD-2 detector from 370 to 520 MeV (Aulchenko *et al.*, 2006) with an achieved precision of comparison of 3% and 1%, respectively.

The measured cross section is shown in Fig. 18 (bottom). For the first time a relatively high-statistics measurement is performed for c.m. energies above 1 GeV. The cross section in this energy range shown in Fig. 19 demonstrates some statistically significant structures that can be possibly explained by the interference between the wide $\rho$-like excited states. Note that the cross section shown in Fig. 18 is bare and includes FSR effects.

The claimed subpercent level of systematic uncertainties on the $e^+e^- \to \pi^+\pi^-$ measurements can be verified by comparison of the results from these different experiments. Above we found that the difference between the KLOE and CMD-2 measurements is larger than their combined

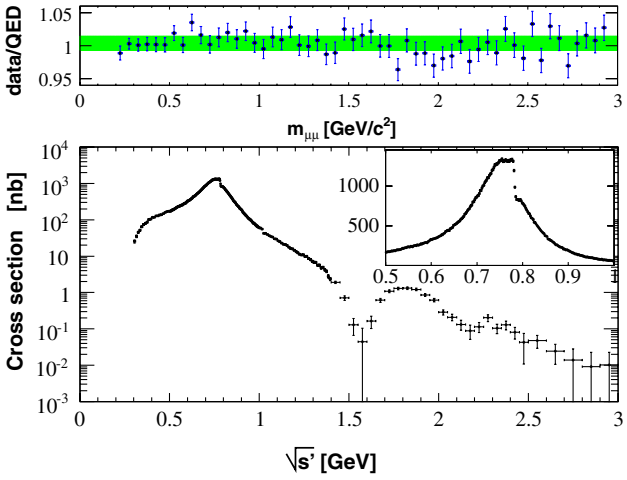


FIG. 18 (color online). Top: The QED test by the ratio of the $e^+e^- \to \mu^+\mu^-$ cross section in data to the theoretical one. Bottom: The $e^+e^- \to \pi^+\pi^-$ cross sections measured with the *BABAR* detector. From Aubert *et al.*, 2009a.

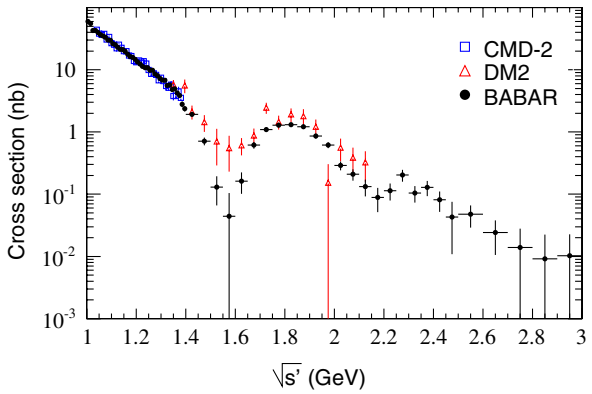


FIG. 19 (color online). The $e^+e^- \to \pi^+\pi^-$ cross section above 1 GeV measured with the *BABAR* detector (Wang, 2009). Comparison with the CMD-2 (Aulchenko *et al.*, 2005) and DM2 (Bisello *et al.*, 1989) measurements is shown.

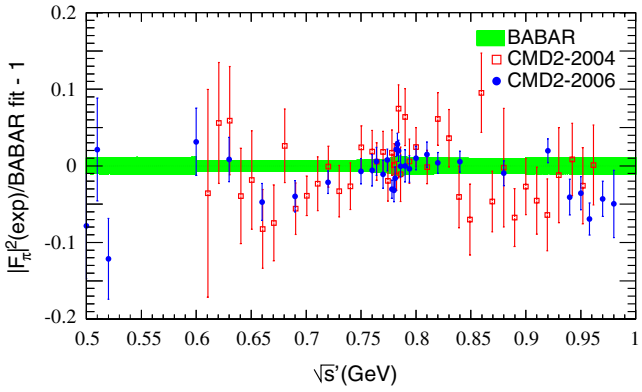


FIG. 21 (color online). The relative difference between the CMD-2 (Akhmetshin *et al.*, 2004a, 2007) and *BABAR* (Wang, 2009) measurements. The band corresponds to the *BABAR* statistical and systematic uncertainties combined in quadrature.

systematic uncertainty. Figure 20 shows a relative difference between the KLOE and *BABAR* measurements. Again the deviations larger than declared systematic errors are seen indicating a presence of unaccounted systematic uncertainties in one or both experiments. Comparison between the CMD-2 and *BABAR* shown in Fig. 21 also reveals some nonstatistical up to 5% deviations both below and above the $\rho$-resonance maximum. In the whole energy range *BABAR* data are in fair agreement with the SND (Achasov *et al.*, 2006) results within experimental uncertainties.

In Sec. VII we discuss the impact of these measurements on the problem of the muon anomaly.

### C. $e^+e^- \to \pi^+\pi^-\pi^0$

A study of the three-pion production in the ISR process was reported by *BABAR* (Aubert *et al.*, 2004b). The three-pion mass distribution for the $e^+e^- \to \pi^+\pi^-\pi^0\gamma$ reaction shown in Fig. 22 is dominated by the well-known $\omega(782)$, $\phi(1020)$, and $J/\psi$ resonances. For the $\omega(782)$ and $\phi(1020)$ resonances they determined the product of the leptonic width and the branching fraction to three pions consistent with other measurements and having comparable accuracy. Large data samples make possible the observation of two structures in the 1–2 GeV/$c^2$ mass region (see Fig. 23). The cross section below 1.4 GeV is in agreement with the SND measurement (Achasov *et al.*, 2002), but at higher energies a large deviation from the DM2 results (Antonelli *et al.*, 1992) is observed. The cross section in this region is fitted (see the inset in Fig. 23) assuming the presence of two excited $\omega$-like states, $\omega(1420)$ and $\omega(1650)$ (Amsler *et al.*, 2008). The

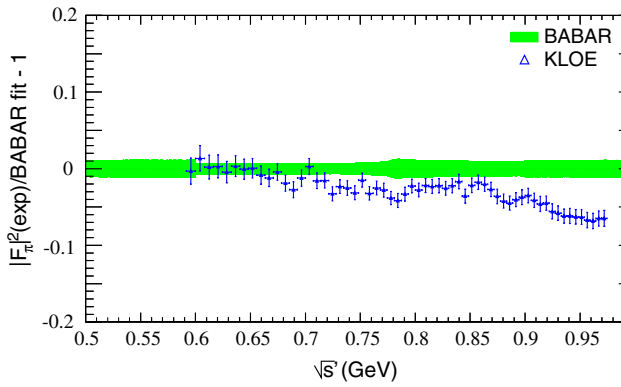


FIG. 20 (color online). The relative difference between the KLOE (Ambrosino *et al.*, 2009) and *BABAR* (Wang, 2009) measurements. The band corresponds to the *BABAR* statistical and systematic uncertainties combined in quadrature.

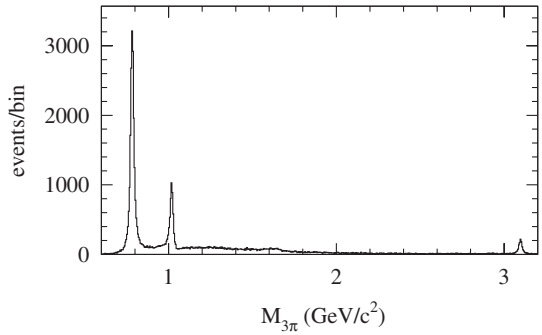


FIG. 22. The $m(\pi^+\pi^-\pi^0)$ distribution for the $e^+e^- \to \pi^+\pi^-\pi^0\gamma$ reaction measured with the *BABAR* detector. From Aubert *et al.*, 2004b.

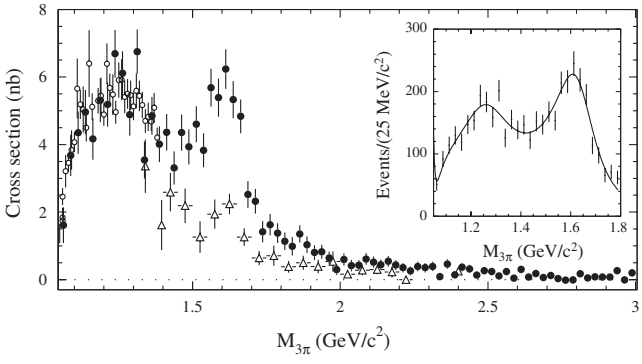


FIG. 23. The $e^+e^- \to \pi^+\pi^-\pi^0$ cross section measured with the *BABAR* detector (Aubert *et al.*, 2004b) (solid circles) in the 1–3 GeV/$c^2$ range compared with the SND (Achasov *et al.*, 2002) (open circles) and DM2 (Antonelli *et al.*, 1992) (triangles) data. The inset shows the mass distribution fitted with two resonances.

parameters of these states are still not well determined. In this case they strongly depend on relative phases between the corresponding amplitudes and their phase differences with the $\omega(782)$ and $\phi(1020)$ amplitudes. The latter resonances have a much larger decay rate to the $3\pi$ mode. The obtained parameters of the $\omega(1420)$ and $\omega(1650)$ amplitudes are discussed in Sec. III.H.

The three-body final state is a relatively simple process for a study of hadron dynamics. Its Dalitz plot analysis shows that the $\rho(770)^{\pm}\pi^{\mp}$ and $\rho(770)^0\pi^0$ intermediate states dominate at all energies. There is also a small contribution of the $\omega\pi$ intermediate state with $\omega$ decay to $\pi^+\pi^-$.

### D. $e^+e^- \to K^+K^-\pi^0$, $K_S^0K^{\pm}\pi^{\mp}$, and $K^+K^-\eta$

Figures 24 and 25 show the $e^+e^- \to K^+K^-\pi^0$ and $e^+e^- \to K_S^0K^{\pm}\pi^{\mp}$ cross sections measured in the *BABAR* experiment (Aubert *et al.*, 2008b) (top) and comparison of the *BABAR* results with DM1 (Buon *et al.*, 1982) and DM2 (Bisello *et al.*, 1991b) measurements below 2.4 GeV, where the previous data are available (bottom). The *BABAR* data are about 10 times more precise. The "spike" at 3.1 GeV is due to $J/\psi$ decays to these final states and will be discussed later.

In the $K^+K^-2\gamma$ final state the $\phi(1020)\eta$ and $\phi(1020)\pi$ intermediate states were also observed. The measured cross sections for these states, which were not previously studied, are shown in Figs. 26 and 27. The $e^+e^- \to \phi(1020)\eta$ is the best channel for a study of the excited $\phi$ state. The contributions of the $\omega$-like states to this channel should be suppressed by the Okubo-Zweig-Iizuka (OZI) rule.

The reaction $e^+e^- \to \phi(1020)\pi^0$ is promising for a search for exotic isovector resonances. Two fits to the data on the $\phi\pi^0$ cross section were performed. In the first one, $\phi\pi^0$ production through a single resonance was assumed, and

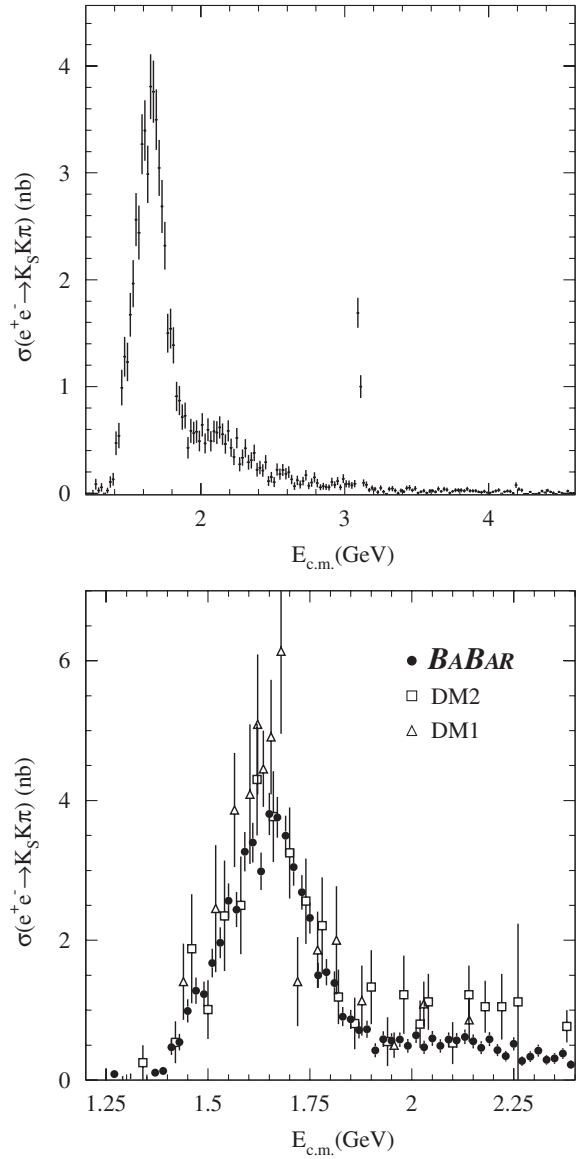


FIG. 24. The $e^+e^- \to K_S^0K^{\pm}\pi^{\mp}$ cross section measured by *BABAR* (Aubert *et al.*, 2008b) (top). Comparison of the *BABAR* measurement with the results of the previous DM1 (Buon *et al.*, 1982) and DM2 (Bisello *et al.*, 1991b) experiments (bottom).

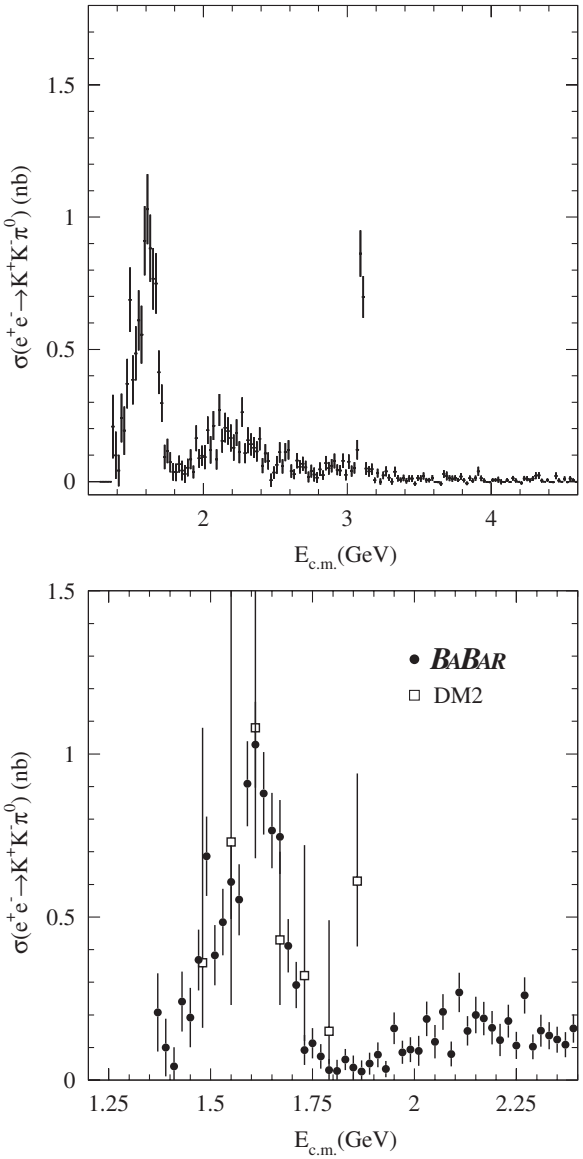


FIG. 25. The $e^+e^- \to K^+K^-\pi^0$ cross section measured by *BABAR* (Aubert *et al.*, 2008b) (top). Comparison of the *BABAR* measurement with the result of the DM2 experiment (Bisello *et al.*, 1991b) (bottom).

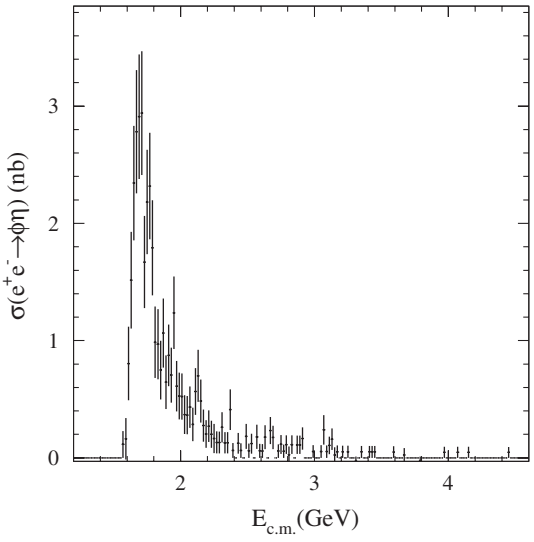


FIG. 26. The $e^+e^- \to \phi\eta$ cross sections measured with the *BABAR* detector. From Aubert *et al.*, 2008b.

the resonance mass and width of $1593 \pm 32$ MeV$/c^2$ and $203 \pm 97$ MeV, respectively, were obtained. These parameters are compatible with those of the $\rho(1700)$ (Amsler *et al.*, 2008). A somewhat better quality of the fit is achieved if two resonances are assumed. The obtained parameters of the first resonance are $1570 \pm 36 \pm 62$ MeV$/c^2$ for the mass and $144 \pm 75 \pm 43$ MeV for the width, i.e., consistent with those of the $C(1480)$ state observed by Bityukov *et al.* (1987). The mass and width for the second resonance are $1909 \pm 17 \pm 25$ MeV$/c^2$ and $48 \pm 17 \pm 2$ MeV, respectively, compatible with the dip already observed in other experiments, predominantly in multipion final states (Castro, 1988; Antonelli *et al.*, 1996; Frabetti *et al.*, 2001; Aubert *et al.*, 2006b). With the limited statistics currently available a firm conclusion cannot be drawn. So, an OZI-violating decay of the $\rho(1700)$ cannot be excluded.

Figure 28 shows the Dalitz plots for the $K^+K^-\pi^0$ and $K^0_SK^\pm\pi^\mp$ final states. It can be seen that the $K\bar{K}^*(892)$ and

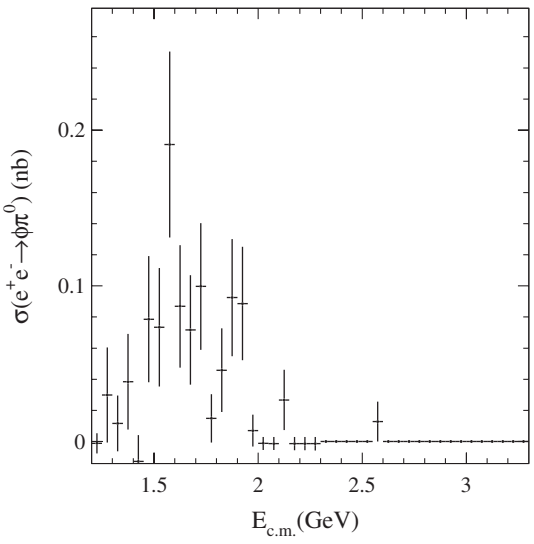


FIG. 27. The $\phi\pi^0$ cross sections measured with the *BABAR* detector. From Aubert *et al.*, 2008b.

$K\bar{K}_2^*(1430)$ intermediate states give the main contribution to the $K\bar{K}\pi$ production. For the $K^0_SK^\pm\pi^\mp$ final state both the neutral $K^0\bar{K}^{*0}$ and charged $K^\pm K^{*\mp}$ combinations are involved. Since the $K^0\bar{K}^{*0}$ and $K^\pm K^{*\mp}$ amplitudes are the sum and the difference of the isovector and isoscalar amplitudes, respectively, the Dalitz plot population for the $K^0_SK^\pm\pi^\mp$ mode is asymmetric and strongly depends on isospin composition. From the Dalitz plot analysis the moduli and relative phase of the isoscalar and isovector amplitudes for both the $K\bar{K}^*(892)$ and $K\bar{K}_2^*(1430)$ intermediate states were determined. The obtained isoscalar and isovector $e^+e^- \to K\bar{K}^*(892)$ cross sections are shown in Figs. 29(a) and 29(b).

The global fit to the $e^+e^- \to \phi(1020)\eta$ and $e^+e^- \to K^+K^-\pi^0$ cross sections, isovector and isoscalar $K\bar{K}^*(892)$ amplitudes, and their relative phase was performed to determine parameters of the $\phi$ and $\rho$ excitations decaying into these final states. The fit results are shown in Fig. 29 and summarized in Table I. The obtained mass and width of the $\phi'$ and $\rho'$ are in reasonable agreement with the parameters of the $\rho(1450)$ and $\phi(1680)$ resonances measured in other experiments [see Amsler *et al.* (2008) for references]. The parameters of the $\phi''$, which are seen in the $\phi\eta$ final state, are close to those for the $Y(2175)$ state observed in the $\phi f_0(980)$ final state. This state will be discussed in Sec. III.F.

### E. $e^+e^- \to \pi^+\pi^-\pi^+\pi^-$, $\pi^+\pi^-2\pi^0$

The reactions $e^+e^- \to \pi^+\pi^-\pi^+\pi^-$ and $\pi^+\pi^-2\pi^0$ have the largest cross sections in the energy region above the $\phi$-meson resonance. They were studied with the *BABAR* detector (Aubert *et al.*, 2005b; Druzhinin, 2007) in the energy region below 4.5 GeV. Figures 30 and 31 show comparison of the *BABAR* results with the previous direct $e^+e^-$ measurements; see Cosme *et al.* (1979), Bacci *et al.* (1980), Cordier *et al.* (1982a), Kurdadze *et al.* (1988), Bisello *et al.* (1991a), Dolinsky *et al.* (1991), Achasov *et al.* (2003), and Akhmetshin *et al.* (2004b) for $\pi^+\pi^-\pi^+\pi^-$ and Cosme *et al.* (1979), Bacci *et al.* (1981), Kurdadze *et al.* (1986), Bisello *et al.* (1991a), Dolinsky *et al.* (1991), Akhmetshin *et al.* (1999), and Achasov *et al.* (2003) for $\pi^+\pi^-2\pi^0$, in the energy range covered by these measurements. The large difference between the data sets from different experiments indicates that some previous measurements had large, up to 50%, unaccounted-for systematic errors. The *BABAR* systematic uncertainty on the $e^+e^- \to \pi^+\pi^-\pi^+\pi^-$ cross section is estimated to be about 5% in the 1–3 GeV energy range. For this channel the *BABAR* data are in good agreement with the recent SND (Achasov *et al.*, 2003) and CMD-2 (Akhmetshin *et al.*, 2004b) measurements at the energies below 1.4 GeV. The DM2 and *BABAR* data are also in reasonable agreement.

For the $\pi^+\pi^-2\pi^0$ channel the *BABAR* results are still preliminary. The estimated systematic uncertainty changes from 8% in the maximum of the cross section to 10% at 1 and 3 GeV.

At energies below 1.4 GeV the *BABAR* cross sections agree well with the results of the recent SND (Achasov *et al.*, 2003) and older OLYA (Kurdadze *et al.*, 1986) measurements, but

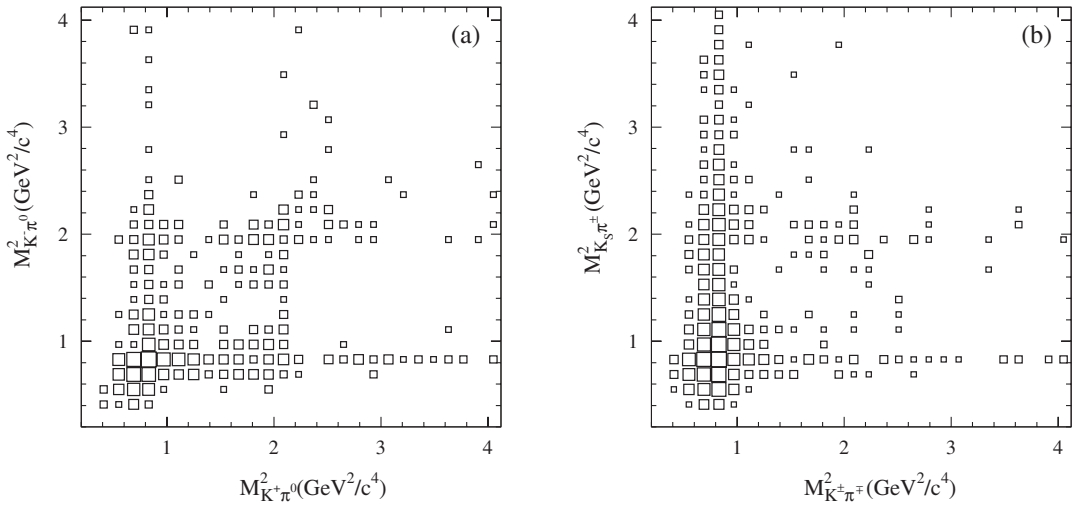


FIG. 28. The Dalitz plot distribution for the (a) $K^+K^-\pi^0$ and (b) $K^0_S K^\pm\pi^\mp$ final state. . A sum over all accessible c.m. energies of the hadronic final states is given. From Aubert *et al.*, 2008b.

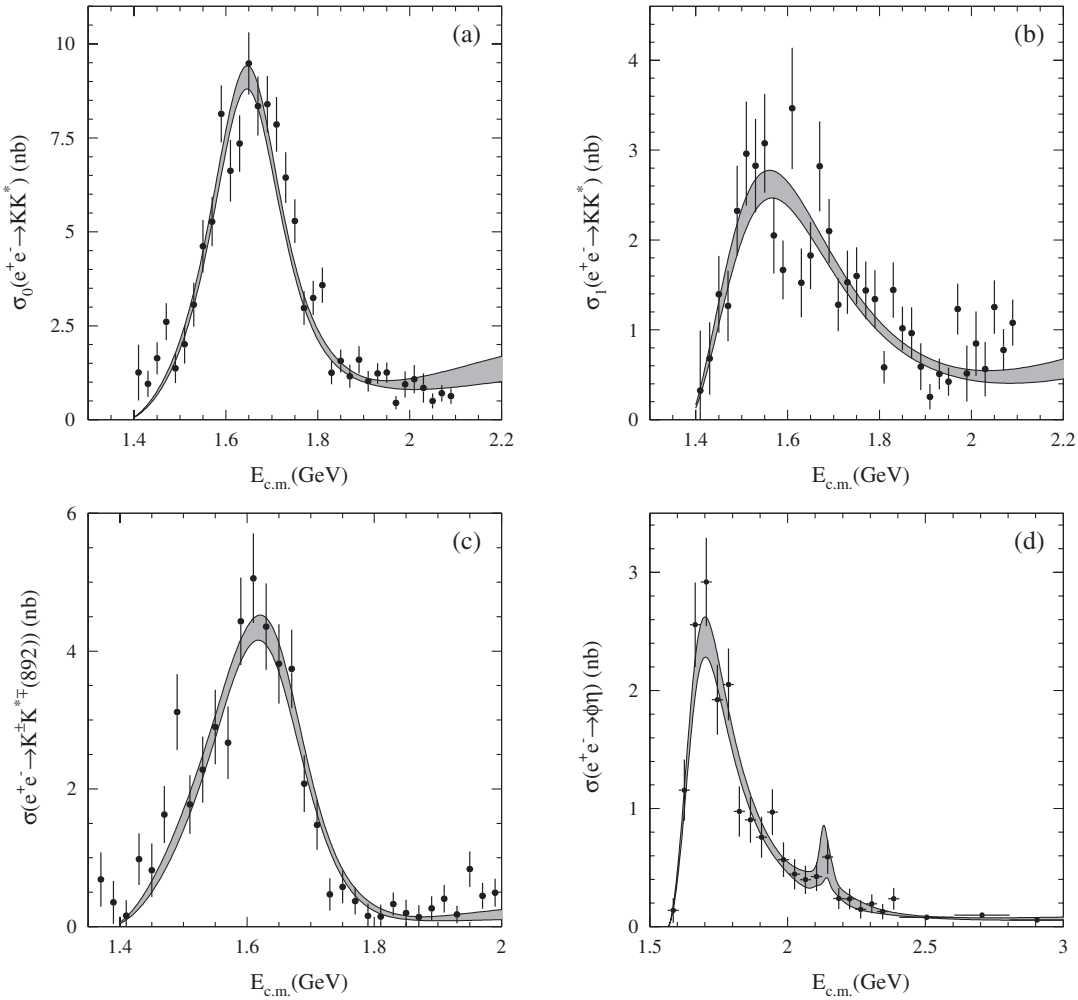


FIG. 29. (a) Isoscalar and (b) isovector components of the $e^+e^-\to K\bar{K}\pi$ cross section; (c) the $e^+e^-\to K^\pm K^*(892)^\mp$ cross section obtained using $e^+e^-\to K^+K^-\pi^0$ events, and (d) the $e^+e^-\to\phi\eta$ cross section. The points with error bars are data and the gray band represents the fit and its uncertainty. From Aubert *et al.*, 2008b.

TABLE I. Parameters of the isoscalar and isovector resonances obtained by Aubert *et al.* (2008b) from the global fit to the isoscalar and isovector amplitudes using the $e^+e^- \to K^\pm K^*(892)^\mp$, $K^0_S K^\pm \pi^\mp$, and $e^+e^- \to \phi\eta$ cross sections.

| $R$ with $I=0$ | $\phi'$ | $\phi''$ |
|---|---|---|
| $\Gamma^R_{ee}\mathcal{B}^R_{KK^*(892)}$ (eV) | $408 \pm 49$ | ... |
| $\Gamma^R_{ee}\mathcal{B}^R_{\phi\eta}$ (eV) | $172 \pm 31$ | $1.9 \pm 1.0$ |
| $m_R$ (MeV) | $1723 \pm 20$ | $2139 \pm 35$ |
| $\Gamma_R$ (MeV) | $371 \pm 75$ | $76 \pm 62$ |
| $R$ with $I=1$ | $\rho'$ | |
| $\Gamma^R_{ee}\mathcal{B}^R_{KK^*(892)}$ (eV) | $135 \pm 12$ | |
| $m_R$ (MeV) | $1506 \pm 16$ | |
| $\Gamma_R$ (MeV) | $437 \pm 24$ | |

not with the ND (Dolinsky *et al.*, 1991) and CMD-2 (Akhmetshin *et al.*, 1999) cross sections that may be affected by large unaccounted-for systematic errors as mentioned previously.

The shape of the cross sections for both reactions shows wide structures peaked at about 1.5 GeV. Different intermediate states contribute to the $e^+e^- \to 4\pi$ cross sections. The observed bumps are sums of the contributions from the $\rho(770)$, $\rho(1450)$, and $\rho(1700)$ decays into these intermediate states, which should be separated for a study of the excited $\rho$ properties. Unfortunately, such an analysis was performed at *BABAR* only at a qualitative level. The two- and three-pion mass distributions for the $\pi^+\pi^-\pi^+\pi^-$ final state are relatively well described by the model of the $a_1(1260)\pi$ intermediate state with a small contribution from the $f_0(1300)\rho$ state. This agrees with the $a_1\pi$ dominance hypothesis suggested by Akhmetshin *et al.* (1999) to describe the $4\pi$ dynamics at energies below 1.4 GeV. A strong deviation from this hypothesis is observed in the $\pi^+\pi^-2\pi^0$ channel. In addition to the expected $\omega\pi^0$ and $a_1\pi$ contributions, a surprisingly large contribution of the $\rho^+\rho^-$ intermediate state was observed. This is demonstrated in Fig. 32, where the $4\pi$ mass spectra for $\omega\pi$, non-$\omega\pi$, and $\rho^+\rho^-$ intermediate states are shown together with the total mass spectrum for the $e^+e^- \to \pi^+\pi^-2\pi^0$ reaction. The contributions of the different intermediate states were separated using simple conditions on $3\pi$ and $2\pi$ invariant masses. It can be seen that the $\rho^+\rho^-$ cross section is more than one-half of the non-$\omega\pi$ cross section at the energy about 1.7 GeV. For the $\pi^+\pi^-2\pi^0$ masses higher than 2.5 GeV/$c^2$ a clear signal of

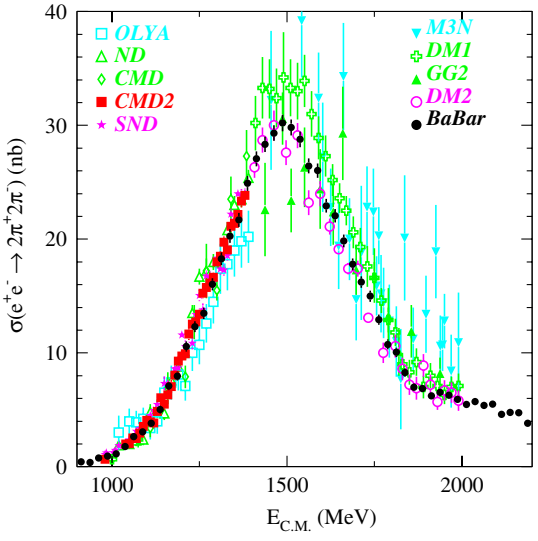


FIG. 30 (color online). Comparison of the *BABAR* results on the $e^+e^- \to \pi^+\pi^-\pi^+\pi^-$ cross section (Aubert *et al.*, 2005b) with the previous direct $e^+e^-$ measurements (Cosme *et al.*, 1979; Bacci *et al.*, 1980; Cordier *et al.*, 1982a; Kurdadze *et al.*, 1988; Bisello *et al.*, 1991a; Dolinsky *et al.*, 1991; Achasov *et al.*, 2003; Akhmetshin *et al.*, 2004b).

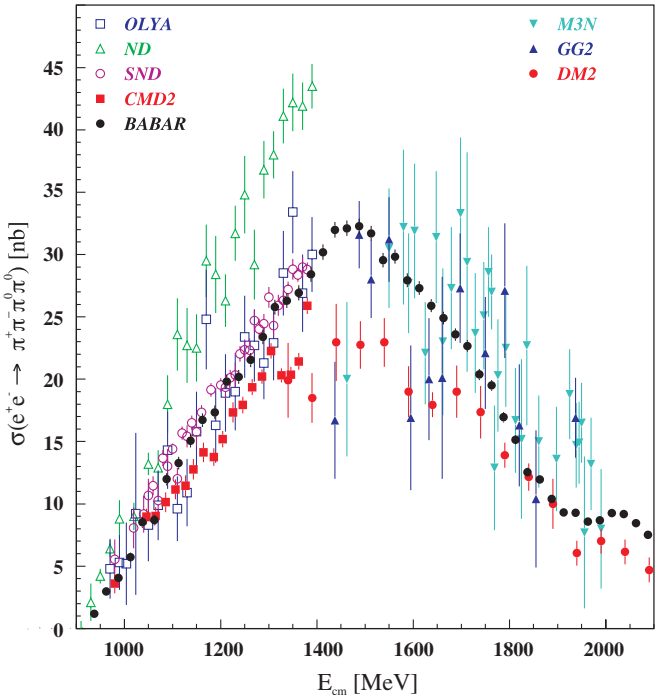


FIG. 31 (color online). Comparison of the *BABAR* results on the $e^+e^- \to \pi^+\pi^-2\pi^0$ cross section (Druzhinin, 2007) with the previous direct $e^+e^-$ measurements (Cosme *et al.*, 1979; Bacci *et al.*, 1981; Kurdadze *et al.*, 1986; Bisello *et al.*, 1991a; Dolinsky *et al.*, 1991; Akhmetshin *et al.*, 1999; Achasov *et al.*, 2003).

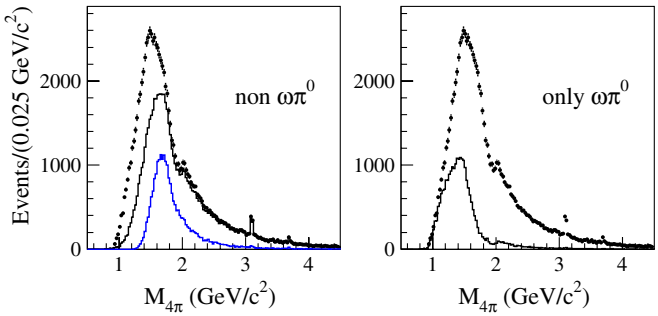


FIG. 32 (color online). The $4\pi$ invariant-mass spectrum for selected $e^+e^- \to \pi^+\pi^-2\pi^0$ events (points with error bars) in comparison with the spectrum for non-$\omega\pi^0$ events only (left) or with the spectrum for $\omega\pi^0$ events only (right). In the left plot the lowest histogram shows the contribution of the $\rho^+\rho^-$ intermediate state. From Druzhinin, 2007.

the $f_0(980)$ meson and a peak at the mass about 1.25 GeV/$c^2$ [probably from the $f_2(1270)$ meson] are seen in the $\pi^0\pi^0$ mass spectrum corresponding to the contributions of the $f_0(980)\rho$ and $f_2(1270)\rho$ intermediate states.

### F. $e^+e^- \to K^+K^-\pi^+\pi^-$, $K^+K^-\pi^0\pi^0$

The $e^+e^- \to K^+K^-\pi^0\pi^0$ reaction has never been studied before the *BABAR* experiment (Aubert *et al.*, 2007b; Lees *et al.*, 2011), while the fully charged mode was previously measured with the DM1 detector (Cordier *et al.*, 1982b) but with an $\approx 100$ times smaller data set. The measured cross sections are shown in Figs. 33 and 34. The systematic uncertainties for these measurements are estimated to be at the (5–9)% level. The structures seen in the cross section energy dependence cannot be understood without an analysis of intermediate states involved.

The distributions of the $K\pi$ invariant masses shown in Fig. 35 indicate that the $K^*(892)^0K^\pm\pi^\mp$ and $K^*(892)^\mp K^\pm\pi^0$ (similar plots are not shown) intermediate states dominate in these reactions. A small contribution from the $K_2^*(1430)K\pi$ state is also seen [Fig. 35(b)]. A special correlation study (Lees *et al.*, 2011) showed that the intermediate state with two $K^*$, $K^*(892)\bar{K}^*(892)$, $K^*(892)\bar{K}_2^*(1430)$, and $K_2^*(1430)\bar{K}_2^*(1430)$, contributes less than 1% to the total reaction yield [the associated $K^*(892)\bar{K}_2^*(1430)$ production is observed in $J/\psi$ decays]. Taking the numbers of events in the $K^*$ peaks for each c.m. energy interval, the "inclusive" $e^+e^- \to K^*(892)^0K\pi$ and $e^+e^- \to K_2^*(1430)^0K\pi$ cross sections shown in Fig. 36 were extracted. Figures 37(a) and 37(b) show scatter plots of the reconstructed $m(\pi^+\pi^-)$ and $m(\pi^0\pi^0)$ vs $m(K^+K^-)$ for selected events of the reactions $e^+e^- \to K^+K^-\pi^+\pi^-$ and $e^+e^- \to K^+K^-\pi^0\pi^0$, respectively. A clear $\phi(1020)$ signal is seen in the $K^+K^-$ invariant mass in both figures and is discussed in more detail below. A signal of the $\rho(770)$ is observed in the $\pi^+\pi^-$ invariant-mass distribution in Fig. 37(a). The $\pi^+\pi^-$ invariant-mass distribution for $K^+K^-\pi^+\pi^-$ events not containing the $K^*(892)$ meson is shown in Fig. 38(a). The $\rho(770)$ peak, probably corresponding to the intermediate $K_1(1230)^\pm$ and $K_1(1400)^\pm K^\mp$ states, is clearly seen in the $\pi^+\pi^-$ mass spectrum. In Fig. 38(b) the inclusive cross section for the $K^+K^-\rho(770)$ reaction is presented. It is obtained by fitting the $\rho(770)$ signal in the $\pi^+\pi^-$ invariant-mass distributions for each c.m. energy interval in Fig. 38.

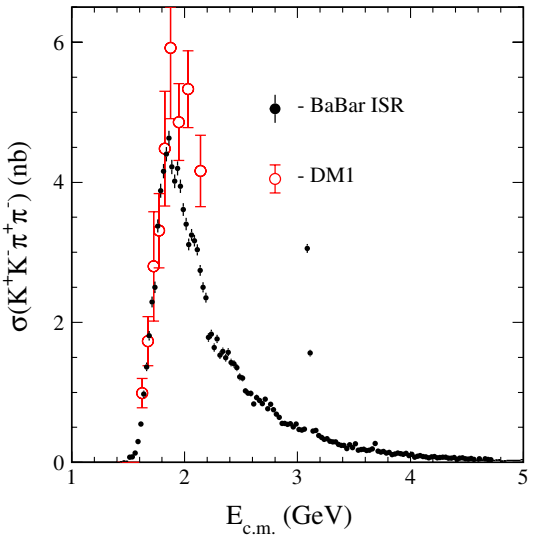


FIG. 33 (color online). The $e^+e^- \to K^+K^-\pi^+\pi^-$ cross section measured with the *BABAR* detector (Lees *et al.*, 2011) in comparison with the only previous measurement by DM1 (Cordier *et al.*, 1982b).

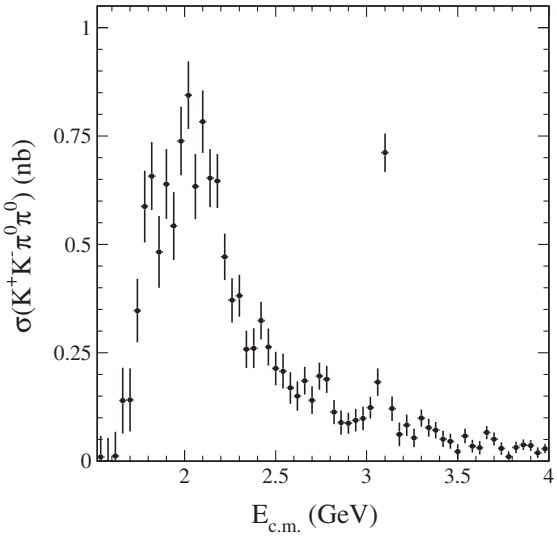


FIG. 34. The $e^+e^- \to K^+K^-\pi^0\pi^0$ cross section measured with the *BABAR* detector. From Lees *et al.*, 2011.

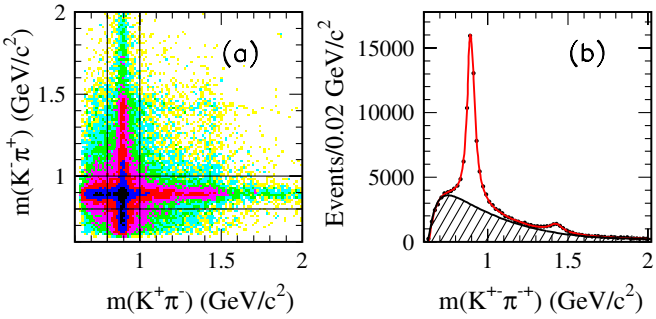


FIG. 35 (color online). (a) Scatter plots $m(K^-\pi^+)$ vs $m(K^+\pi^-)$, and (b) projection $m(K^\pm\pi^\mp)$ plot (two entries per event) for the reaction $e^+e^- \to K^+K^-\pi^+\pi^-$. A sum over all accessible c.m. energies is given. From Lees *et al.*, 2011.

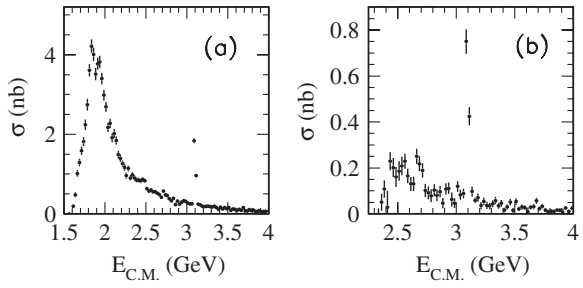


FIG. 36. (a) The $e^+e^- \to K^*(892)^0K\pi$, and (b) $K_2^*(1430)^0K\pi$ cross sections obtained from the $K^*(892)^0$ and $K_2^*(1430)^0$ signals of Fig. 35(b), respectively. From Lees *et al.*, 2011.

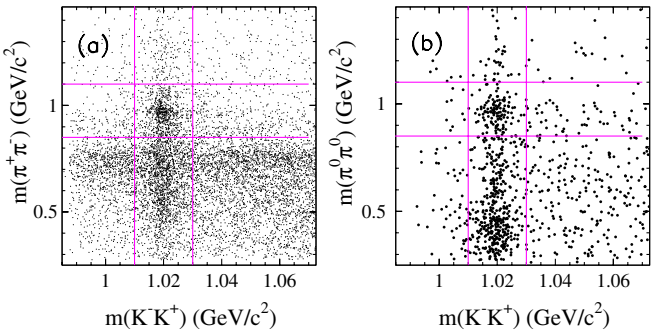


FIG. 37 (color online). The scatter plots of the reconstructed (a) $m(\pi^+\pi^-)$ and (b) $m(\pi^0\pi^0)$ vs $m(K^+K^-)$ for selected events in the data. The vertical (horizontal) lines bound a $\phi$ [$f_0(980)$] signal region. From Lees *et al.*, 2011.

One of the interesting ISR studies performed by *BABAR* (Aubert *et al.*, 2007b) and later reproduced by Belle (Shen *et al.*, 2009) is extracting relatively small contributions of the $\phi(1020)\pi^+\pi^-$, $\phi(1020)\pi^0\pi^0$, $(\phi \to K^+K^-)$ intermediate states. Since the $\phi(1020)$ resonance is relatively narrow, the clean sample of $\phi\pi\pi$ events can easily be separated. Figure 39 shows the $m(\pi^+\pi^-)$ distribution for these events demonstrating a clear signal from the $f_0(980)$ resonance and a bump at lower masses which can be interpreted as the $f_0(600)$ state. A similar plot is obtained for the $\pi^0\pi^0$ invariant mass. These invariant-mass distributions can be fitted with a superposition of two Breit-Wigner functions for the scalar $f_0(980)$ and $f_0(600)$ resonances as shown in Fig. 39. The $e^+e^- \to \phi(1020)\pi^+\pi^-$ cross section measured by *BABAR* and Belle is shown in Fig. 40. Two resonance structures are seen at 1.7 and 2.1 GeV. The *BABAR* Collaboration investigated decay mechanisms for these structures and concluded that the second structure decays only to the $\phi(1020)f_0(980)$ final state. The structure completely disappears if events associated with the $f_0(980)$ peak in the $m(\pi^+\pi^-)$ distribution are removed. The first structure is associated with the $\phi(1680)$, a radial excitation of the vector $s\bar{s}$ state. Its decays to $\phi(1020)f_0(600)$ and $\phi(1020)f_0(980)$ are not forbidden.

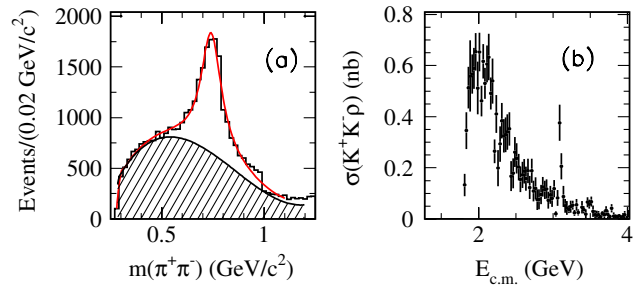


FIG. 38 (color online). (a) The $\pi^+\pi^-$ mass distribution for $K^+K^-\pi^+\pi^-$ events [$K^*(892)K\pi$ events are excluded]; the solid curve represents a fit using a signal Breit-Wigner function with $\rho(770)$ parameters and a polynomial background (hatched area). (b) The $e^+e^- \to K^+K^-\rho(770)$ cross section obtained using the fitted numbers of $\rho$-meson events in each 25 MeV c.m. energy interval. From Lees *et al.*, 2011.

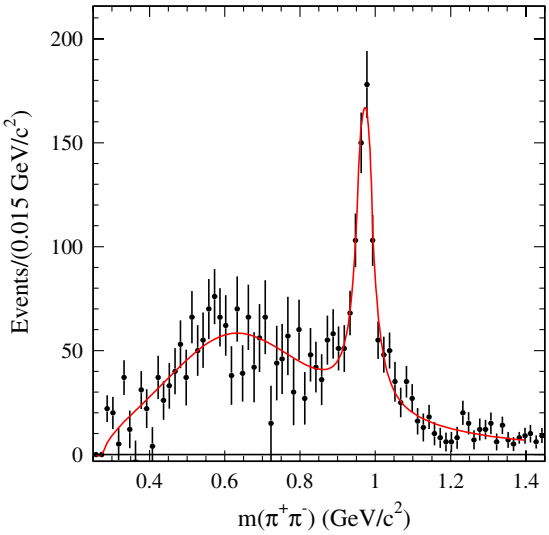


FIG. 39 (color online). The $m(\pi^+\pi^-)$ distribution for the $e^+e^- \to \phi(1020)\pi^+\pi^-$ reaction. From Lees *et al.*, 2011.

A simple model based on the vector meson dominance (VDM) was suggested to describe the observed $e^+e^- \to \phi(1020)\pi^+\pi^-$ cross section. The model assumes that two vector mesons contribute to the cross section; one resonance associated with the $\phi(1680)$ decays both to $\phi f_0(600)$ and to $\phi f_0(980)$, while another referred to as $Y(2175)$ decays to $\phi f_0(980)$ only. Since the nominal $\phi(1680)$ mass lies below the $\phi f_0(980)$ threshold, the $\phi(1680) \to \phi f_0(980)$ decay will reveal itself as a smooth bump in the energy dependence of the $e^+e^- \to \phi f_0(980)$ cross section above 2 GeV. The result of the fit to the $e^+e^- \to \phi(1020)\pi^+\pi^-$ cross section with this model is shown in Fig. 41. It is clearly seen that the data above 2 GeV cannot be described with a contribution of the $\phi(1680)$ resonance only. An additional relatively narrow resonance $Y(2175)$ is needed to do this. The tongue below 2 GeV in the cross section for the reaction $e^+e^- \to \phi(1680) \to \phi f_0(980)$ in Fig. 41 is due to the finite width of the $f_0(980)$ state.

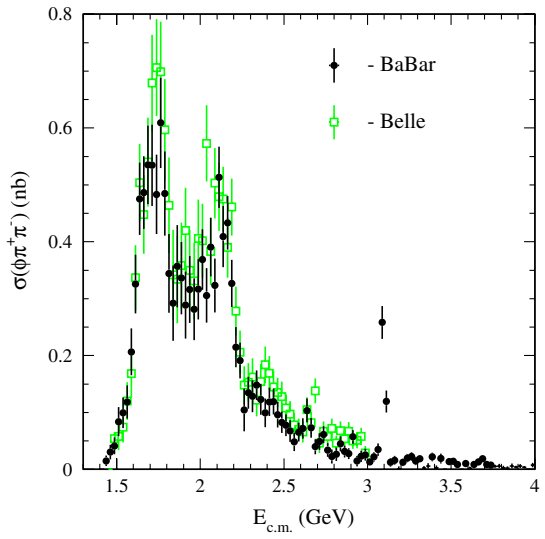


FIG. 40 (color online). The $e^+e^- \to \phi\pi^+\pi^-$ cross sections measured with the *BABAR* (Lees *et al.*, 2011) (circles) and Belle (Shen *et al.*, 2009) (squares) detectors.

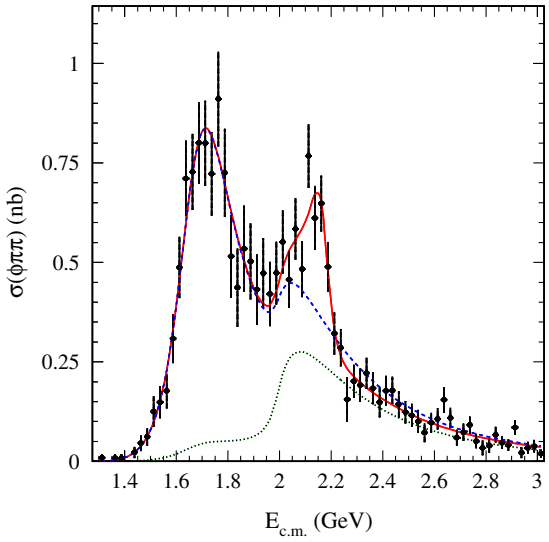


FIG. 41 (color online). The fit to the $e^+e^- \to \phi\pi^+\pi^-$ cross section in the two-resonance model described in the text (solid curve). The contribution of the first resonance [$\phi(1680)$] is shown by the dashed line. The dotted line shows the first resonance contribution in the $\phi f_0(980)$ decay mode only. From Lees *et al.*, 2011.

A relatively clean sample of $\phi f_0(980)$ events is selected using the requirement $0.85 < m(\pi\pi) < 1.1$ GeV/$c^2$. The cross section for events of the $K^+K^-\pi^+\pi^-$ mode, fitted with the model described above, is shown in Fig. 42. The contribution of the $Y(2175)$ is seen much better with this selection. The comparison of the $e^+e^- \to \phi f_0(980)$ cross sections measured by *BABAR* in two $f_0(980)$ decay modes, $\pi^+\pi^-$ and $\pi^0\pi^0$, is shown in Fig. 43. It can be seen that two measurements agree. The fit of two modes gives the peak cross section, mass, and width of the resonance:

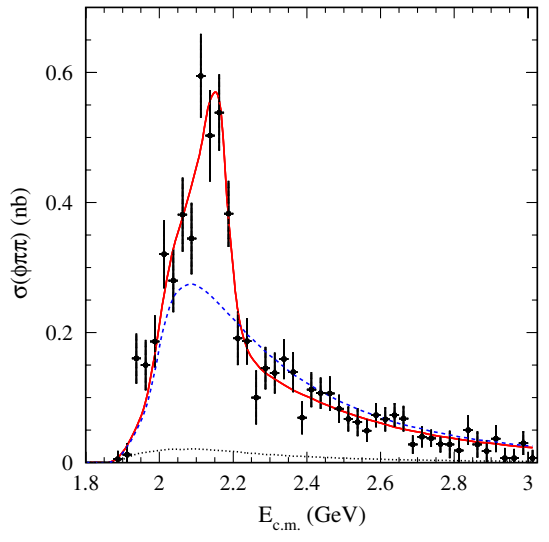


FIG. 42 (color online). The cross section for $e^+e^- \to \phi(1020)f_0(980)$ events selected with the cut $0.85 < m(\pi\pi) < 1.1$ GeV/$c^2$. The solid curve is the result of the two-resonance fit. The dashed and dotted curves are the contributions from the $\phi(1680) \to \phi f_0(980)$ and $\phi(1680) \to \phi f_0(600)$ decay channels, respectively. From Lees *et al.*, 2011.

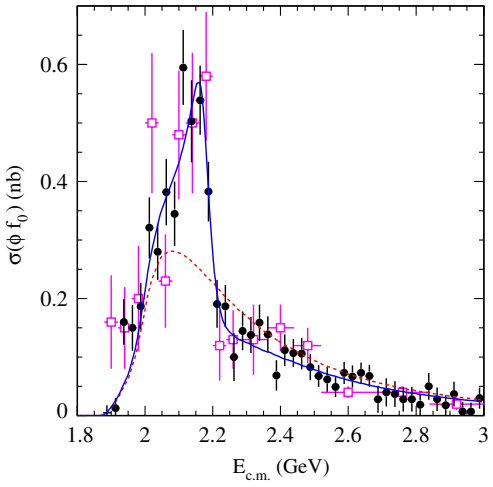


FIG. 43 (color online). The $e^+e^- \to \phi(1020)f_0(980)$ cross section measured in the $K^+K^-\pi^+\pi^-$ (circles) and $K^+K^-\pi^0\pi^0$ (squares) final states by *BABAR*. The solid and dashed curves represent the results of the two-resonance fit described in the text. From Lees *et al.*, 2011.

$$\sigma_Y = 0.104 \pm 0.025 \text{ nb},$$
$$m_Y = 2.179 \pm 0.009 \text{ GeV}/c^2,$$
$$\Gamma_Y = 0.079 \pm 0.017 \text{ GeV}.$$

The $e^+e^- \to \phi f_0(980)$ cross section measured in the Belle experiment (Shen *et al.*, 2009) is shown in Fig. 44 and also requires a resonance structure with similar parameters. Some properties of this resonance, a relatively small width and absence of the $\phi f_0(600)$ decay, are unusual.

The nature of this state is not clear (Napsuciale *et al.*, 2007; Gomez-Avila, Napsuciale, and Oset, 2009). One of the possible interpretations is that the $Y(2175)$ is a $s\bar{s}s\bar{s}$ four-quark state. Indeed, the $f_0(600)$ does not contain strange quarks, while the $f_0(980)$, strongly coupled with $K\bar{K}$, definitely contains them. For the $s\bar{s}s\bar{s}$ state, the observed

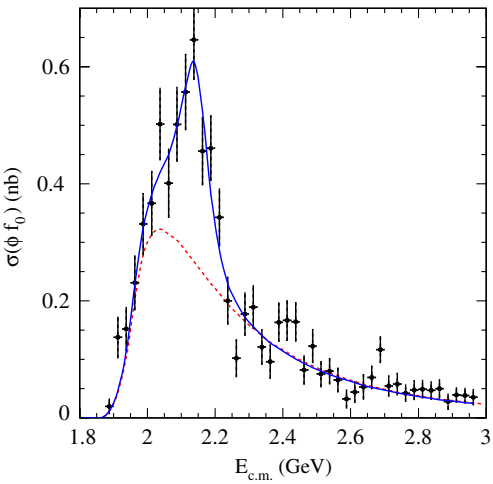


FIG. 44 (color online). The $e^+e^- \to \phi(1020)f_0(980)$ cross section measured by Belle. The solid and dashed curves represent the results of the two-resonance fit described in the text. From Shen *et al.*, 2009.

$Y(2175) \to \phi f_0(980)$ is natural decay, while the not seen $Y(2175) \to \phi f_0(600)$ transition is suppressed by the OZI rule. The observation of the $Y(2175)$ decay to the $\phi\eta$ final state containing four $s$ quarks also supports this hypothesis.

### G. $e^+e^- \to 2(K^+K^-)$

The reaction $e^+e^- \to 2(K^+K^-)$ was studied for the first time by *BABAR* (Aubert *et al.*, 2007b). The measured cross section is shown in Fig. 45. The most significant structure in the cross sections is due to the $J/\psi$ decay. It is natural to expect that intermediate states for this reaction contain the $\phi(1020)$ meson which has a large decay rate to $K^+K^-$. Indeed, the strong $\phi$ meson peak can be seen in the $K^+K^-$ invariant-mass distribution shown in Fig. 46. Since the $\phi$ meson is present in almost every four-kaon event, it is concluded that the reaction $e^+e^- \to 2(K^+K^-)$ is strongly dominated by the $\phi K^+K^-$ production.

A study of events containing the $\phi$ meson was performed by *BABAR*. The $K^+K^-$ pair forming the $\phi$ meson is selected by the requirement that its invariant mass is within $\pm 10$ MeV of the $\phi$ nominal mass. The invariant-mass distribution for the second $K^+K^-$ pair is shown in Fig. 47(a). Figures 47(b)–47(d) show the cross section for events with the $K^+K^-$ invariant mass in regions 1, 2, and 3 indicated in Fig. 47(a). An enhancement in the $K^+K^-$ invariant-mass spectrum near the $K^+K^-$ threshold can be interpreted as being due to the decay $f_0(980) \to K^+K^-$. Therefore, the cross section for region 1 is expected to have a structure similar to that observed in $e^+e^- \to \phi f_0 \to K^+K^-\pi\pi$ (see Sec. III.F). The bump at 2.175 GeV can indeed be seen in the cross section shown in Fig. 47(b), however, the data sample is too low to perform a quantitative analysis.

The relatively narrow region 2 with $1.06 < m(K^+K^-) < 1.2$ GeV/$c^2$ is responsible for the spike seen at 2.25 GeV in Fig. 45. The spike is much more significant in Fig. 47(c) showing the cross section for events from this mass region. There is no explanation of this structure.

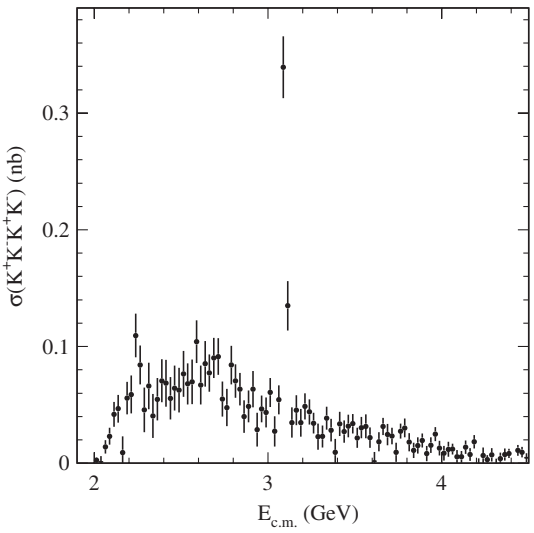


FIG. 45. The $e^+e^- \to 2(K^+K^-)$ cross section as a function of c.m. energy measured with the *BABAR* detector using ISR. From Aubert *et al.*, 2007b.

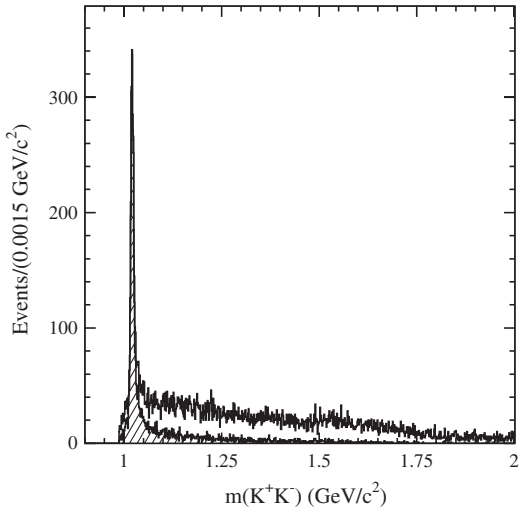


FIG. 46. The $K^+K^-$ invariant-mass distribution for selected $e^+e^- \to 2(K^+K^-)$ events (open histogram, four entries per event), and that for the combination in each event closest to the $\phi$-meson mass (hatched histogram). From Aubert *et al.*, 2007b.

The peak in the $K^+K^-$ mass spectrum near 1.5 GeV/$c^2$ is associated with the $f_2'(1525)$. Region 3 [$1.45 < m(K^+K^-) < 1.6$ GeV/$c^2$] is chosen to select $\phi f_2'(1525)$ events. The cross section for this mass region is shown in Fig. 47(d) and exhibits a broad structure at 2.7 GeV and a strong $J/\psi$ signal.

### H. $e^+e^-$ → five mesons

The *BABAR* detector studied a number of ISR reactions with five hadrons in the final state: $2(\pi^+\pi^-)\pi^0$, $2(\pi^+\pi^-)\eta$, $K^+K^-\pi^+\pi^-\pi^0$, and $K^+K^-\pi^+\pi^-\eta$ (Aubert *et al.*, 2007c).

The $e^+e^- \to 2(\pi^+\pi^-)\pi^0$ reaction has the largest cross section among the processes mentioned. In the $\pi^+\pi^-\pi^0$ invariant-mass spectrum for this reaction (see Fig. 48) clear signals of $\eta$ and $\omega$ mesons are seen corresponding to the $\omega\pi^+\pi^-$ and $\eta\pi^+\pi^-$ intermediate states. The cross sections for these reactions were measured in direct $e^+e^-$ experiments (Cordier *et al.*, 1981; Druzhinin *et al.*, 1986; Antonelli *et al.*, 1988, 1992; Akhmetshin *et al.*, 2000), but *BABAR* data are significantly more accurate. The $e^+e^- \to \eta\pi^+\pi^-$ and $e^+e^- \to \omega\pi^+\pi^-$ cross sections measured by *BABAR* and in direct $e^+e^-$ experiments are shown in Figs. 49 and 50, respectively.

The two pions from the reaction $e^+e^- \to \eta\pi^+\pi^-$ predominantly form the $\rho(770)$. In the two-pion invariant-mass spectrum for the $e^+e^- \to \omega\pi^+\pi^-$ reaction shown in Fig. 51 a clear $f_0(980)$ signal is observed. The contribution of the $\omega f_0(980)$ intermediate state was extracted, and the cross section $e^+e^- \to \omega f_0(980)$ was measured for the first time (see Fig. 52). The $e^+e^- \to \omega\pi^+\pi^-$ cross section after subtraction of the $\omega f_0(980)$ contribution is shown in Fig. 53. The cross section is fitted with a sum of two resonances. The fit result is shown in Fig. 53 and listed in Table II. The parameters obtained are in good agreement with those obtained for the $\pi^+\pi^-\pi^0$ channel (see Sec. III.J).

The $\omega\pi^+\pi^-$ and $\eta\pi^+\pi^-$ intermediate states do not saturate the total $e^+e^- \to 2(\pi^+\pi^-)\pi^0$ cross section as shown in Fig. 54. The $m(\pi^+\pi^-)$ and $m(\pi^\pm\pi^0)$ distributions

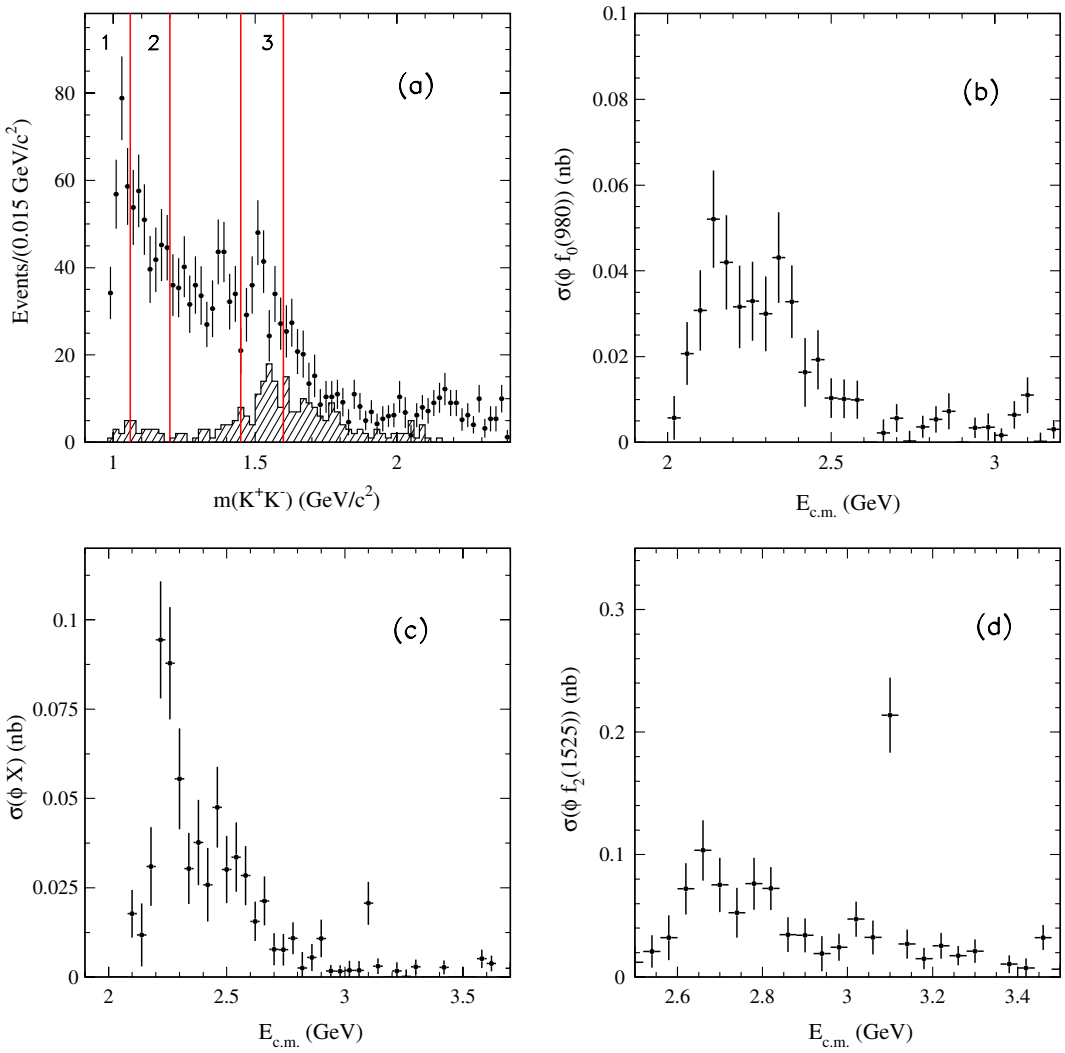


FIG. 47 (color online). The $K^+K^-$ invariant-mass distribution for $\phi K^+K^-$ events. (a) Events from the $J/\psi \to \phi K^+K^-$ decay are excluded from the spectrum shown by the open histogram. The hatched histogram is for events from the $J/\psi$ decay. The numbered regions of the $K^+K^-$ mass spectrum are used to calculate the cross sections shown in (b), (c), and (d) for the regions 1, 2, and 3, respectively. From Aubert *et al.*, 2007b.

for $e^+e^- \to 2(\pi^+\pi^-)\pi^0$ events with the $\omega\pi^+\pi^-$ and $\eta\pi^+\pi^-$ contributions excluded are shown in Fig. 55. From the analysis of these two-pion mass distributions it was concluded that the dominant intermediate state for these events is $\rho^0\rho^\pm\pi^\mp$. The $\rho\pi$ mass spectrum also exhibits a resonance structure with the following parameters:

$$m_X = 1.243 \pm 0.012 \pm 0.020 \text{ GeV}/c^2,$$
$$\Gamma_X = 0.410 \pm 0.031 \pm 0.030 \text{ GeV}.$$

The yield of the $X(1240)$ state is consistent with the complete dominance of the quasi-two-body reaction $e^+e^- \to \rho(770)X(1240) \to \rho^0\rho^\pm\pi^\mp$. The best candidates for $X(1240)$ are the $\pi(1300)$ or $a_1(1260)$ resonances (Amsler *et al.*, 2008).

The $e^+e^- \to 2(\pi^+\pi^-)\eta$ reaction was studied for the first time by *BABAR*. The measured cross section is shown in Fig. 56. A rich internal structure is expected for the $4\pi\eta$ final state. The four-pion mass distribution exhibits a wide resonance structure which can be a mixture of the known $\rho(1450)$

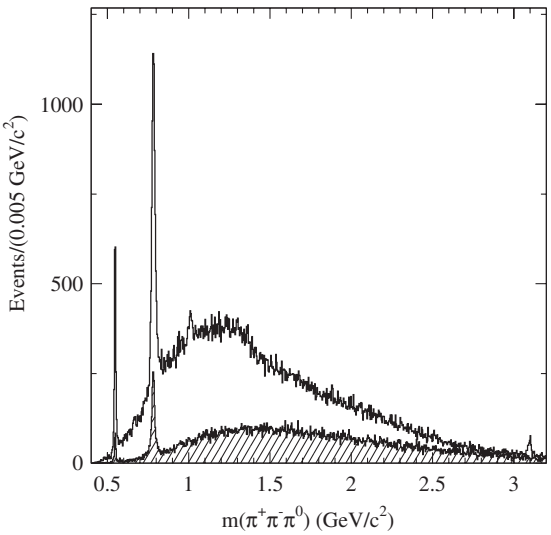


FIG. 48. The $m(\pi^+\pi^-\pi^0)$ distribution for $2(\pi^+\pi^-)\pi^0$ events. From Aubert *et al.*, 2007c.

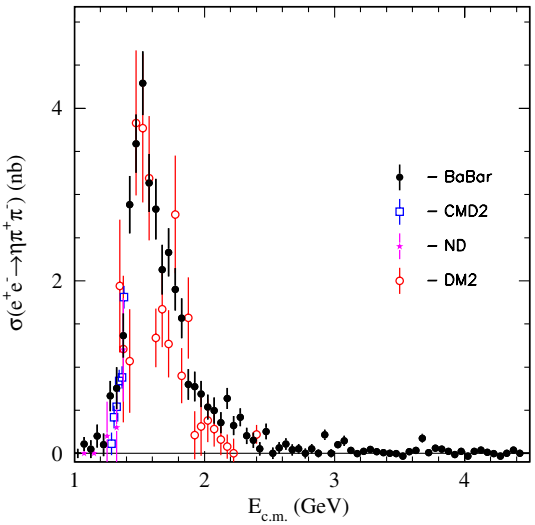


FIG. 49 (color online). The $e^+e^- \to \eta\pi^+\pi^-$ cross section measured by *BABAR* (Aubert *et al.*, 2007c) in comparison with the direct $e^+e^-$ measurements (Druzhinin *et al.*, 1986; Antonelli *et al.*, 1992; Akhmetshin *et al.*, 2000).

and $\rho(1700)$ resonances. Figure 57(a) shows the $\eta\pi^+\pi^-$ mass distribution with two narrow peaks. The lowest mass peak corresponds to $\eta'(958)$. The measured $e^+e^- \to \eta'(958)\pi^+\pi^-$ cross section is shown in Fig. 57(b). The resonancelike structure observed in the cross section energy dependence is fitted with a single Breit-Wigner function. The fitted resonance parameters are

$$\sigma_0 = 0.18 \pm 0.07 \text{ nb},$$
$$m_x = 1.99 \pm 0.08 \text{ GeV}/c^2,$$
$$\Gamma_x = 0.31 \pm 0.14 \text{ GeV}.$$

There is no entry for these parameters in the current PDG tables (Amsler *et al.*, 2008). Taking into account possible large systematic uncertainties on mass and width, the observed resonance can be interpreted as the $\rho(2150)$, extensively discussed in the past (Amsler *et al.*, 2008).

Another clear structure seen in the $\eta\pi^+\pi^-$ mass distribution [Fig. 57(a)] and shown in detail in Fig. 58(a) was interpreted as the $f_1(1285)$ meson. The measured $e^+e^- \to f_1(1285)\pi^+\pi^-$ cross section is shown in Fig. 58(b). The observed resonance structure has the following parameters:

$$\sigma_0 = 1.00 \pm 0.18 \pm 0.15 \text{ nb},$$
$$m_x = 2.15 \pm 0.04 \pm 0.05 \text{ GeV}/c^2,$$
$$\Gamma_x = 0.35 \pm 0.04 \pm 0.05 \text{ GeV}.$$

The mass and width are close to those measured in the reaction $e^+e^- \to \eta'(958)\pi^+\pi^-$, but the cross section is

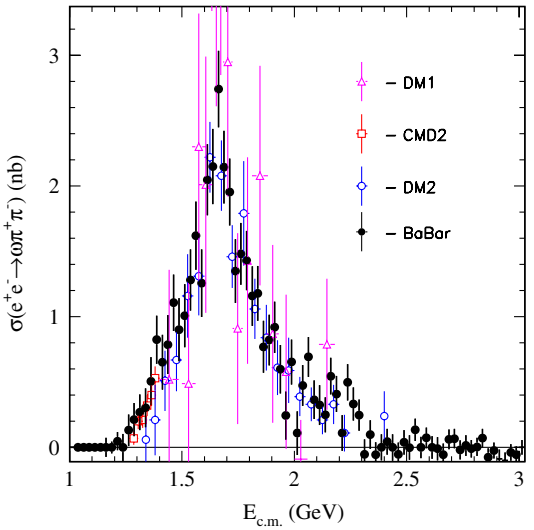


FIG. 50 (color online). The $e^+e^- \to \omega\pi^+\pi^-$ cross section measured by *BABAR* (Aubert *et al.*, 2007c) in comparison with the direct $e^+e^-$ measurements (Cordier *et al.*, 1981; Antonelli *et al.*, 1988; Akhmetshin *et al.*, 2000).

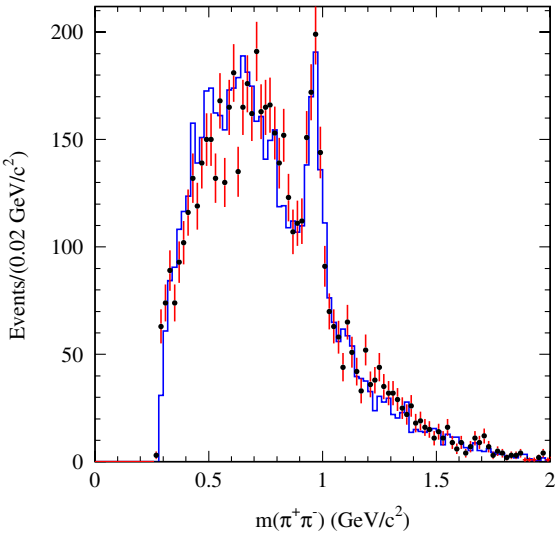


FIG. 51 (color online). The $m(\pi^+\pi^-)$ distribution for selected $\omega\pi^+\pi^-$ events in data (points with error bars) and in simulation (histogram). From Aubert *et al.*, 2007c.

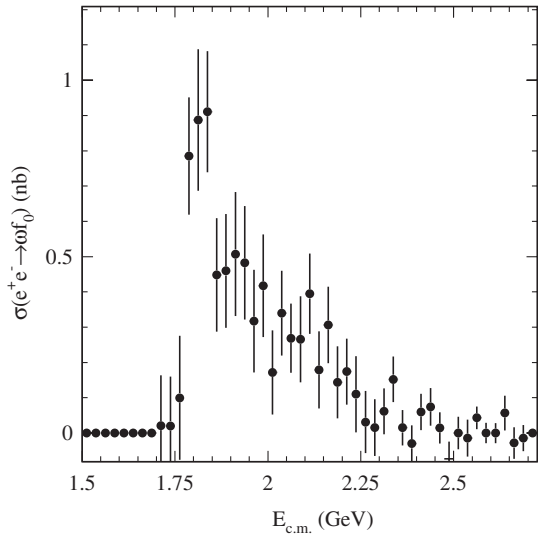


FIG. 52. The $e^+e^- \to \omega f_0(980)$ cross section measured by *BABAR*. From Aubert *et al.*, 2007c.

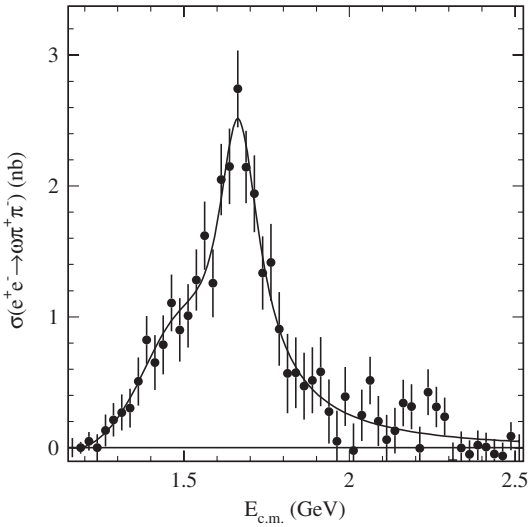


FIG. 53. The fit with two Breit-Wigner functions to the $\omega\pi^+\pi^-$ cross section with the $\omega f_0(980)$ contribution subtracted. From Aubert *et al.*, 2007c.

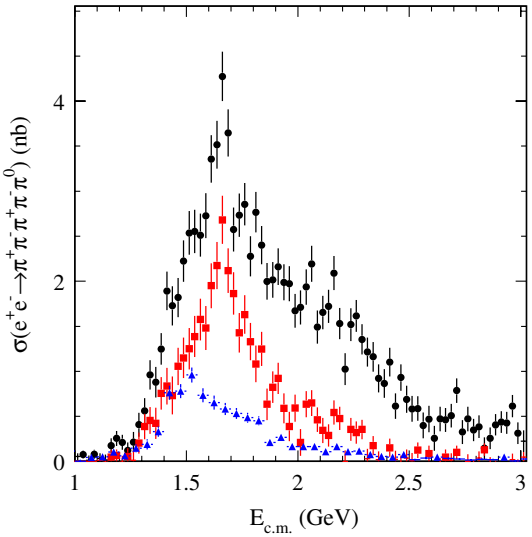


FIG. 54 (color online). The $e^+e^- \to 2(\pi^+\pi^-)\pi^0$ cross section (circles) and contributions from $\omega\pi^+\pi^-$ (squares) and $\eta\pi^+\pi^-$ (triangles). From Aubert *et al.*, 2007c.

significantly larger. The observed structure can also be assigned to the $\rho(2150)$ resonance.

The cross section for the reaction $e^+e^- \to K^+K^-\pi^+\pi^-\pi^0$ shown in Fig. 59 was also measured by *BABAR* for the first time. The three-pion and two-kaon invariant-mass spectra for this reaction are shown in Fig. 60. Clear $\eta$ and $\omega$ signals can be seen in the three-pion mass distribution and a strong $\phi$ signal in the $K^+K^-$ mass distribution. Figure 61 shows the calculated cross sections for the (a) $e^+e^- \to \phi\eta$ and (b) $e^+e^- \to \omega K^+K^-$ subprocesses. The former is in good agreement with that obtained in the $\eta \to \gamma\gamma$ mode (Aubert *et al.*, 2008b). It is a first observation of the process $e^+e^- \to \omega K^+K^-$.

The reaction $e^+e^- \to K^+K^-\pi^+\pi^-\eta$ was also studied by *BABAR* (Aubert *et al.*, 2007c). The measured cross section is small and rises from threshold to a maximum value of about 0.2 nb at 2.8 GeV, followed by a monotonic decrease with increasing energy. The clear signal of the $\phi\eta'(958)$ intermediate state is observed in the $K^+K^-$ and $\pi^+\pi^-\eta$ mass distributions. Unfortunately, the $\phi\eta'(958)$ invariant-mass spectrum is not shown in Aubert *et al.* (2007c). This spectrum is interesting since for the four-quark $Y(2175)$ resonance (see Sec. III.F), the decay to $\phi\eta'(958)$, is expected.

### I. $e^+e^- \to 3(\pi^+\pi^-)$, $2(\pi^+\pi^-\pi^0)$

The reactions $e^+e^- \to 3(\pi^+\pi^-)$ and $e^+e^- \to 2(\pi^+\pi^-\pi^0)$ were studied before in a number of direct $e^+e^-$ experiments, but with limited data samples (Cosme *et al.*, 1979; Bacci *et al.*, 1981; Bisello *et al.*, 1981; Esposito *et al.*, 1981; Castro, 1988). The *BABAR* detector studied the six-pion production using the ISR method from the threshold to 4.5 GeV (Aubert *et al.*, 2006b). As a result, the statistical and systematic uncertainties on the cross sections were dramatically reduced.

An interesting feature of the $3(\pi^+\pi^-)$ final state is the presence, among many $\pi^+\pi^-$ combinations, of only one $\rho(770)^0$ per event. No other intermediate resonance signals were observed. For the $2(\pi^+\pi^-\pi^0)$ final state also one

TABLE II. Summary of the $\omega(1420)$ ($\omega'$) and $\omega(1650)$ ($\omega''$) resonance parameters obtained from the fits described in the text. The values without errors were fixed in the fits.

| Fit | $\omega\eta$ (Aubert *et al.*, 2006b) | $\omega\pi^+\pi^-$ (Aubert *et al.*, 2007c) | $3\pi$ (Aubert *et al.*, 2004b) | PDG (Amsler *et al.*, 2008) |
|---|---|---|---|---|
| $\sigma_{0\omega'}$ (nb) | ... | $1.01 \pm 0.29$ | ... | ... |
| $B_{ee}B_{\omega' f} \times 10^6$ | ... | $0.13 \pm 0.04$ | $0.82 \pm 0.08$ | ... |
| $\Gamma_{ee}B_{\omega' f}$ (eV) | ... | $17.5 \pm 5.4$ | 369 | ... |
| $m_{\omega'}$ (GeV/$c^2$) | ...- | $1.38 \pm 0.02 \pm 0.07$ | $1.350 \pm 0.030$ | 1.40–1.45 |
| $\Gamma_{\omega'}$ (GeV) | ... | $0.13 \pm 0.05 \pm 0.01$ | $0.450 \pm 0.140$ | 0.180–0.250 |
| $\phi_{\omega'}$ (rad) | ... | $\pi$ | $\pi$ | ... |
| $\sigma_{0\omega''}$ (nb) | $3.08 \pm 0.33$ | $2.47 \pm 0.18$ | ... | ... |
| $B_{ee}B_{\omega'' f} \times 10^6$ | ... | $0.47 \pm 0.04$ | $1.3 \pm 0.2$ | ... |
| $\Gamma_{ee}B_{\omega'' f}$ (eV) | ... | $103.5 \pm 8.3$ | 286 | ... |
| $m_{\omega''}$ (GeV/$c^2$) | $1.645 \pm 0.008$ | $1.667 \pm 0.013 \pm 0.006$ | $1.660 \pm 0.011$ | $1.670 \pm 0.030$ |
| $\Gamma_{\omega''}$ (GeV) | $0.114 \pm 0.014$ | $0.222 \pm 0.025 \pm 0.020$ | $0.220 \pm 0.040$ | $0.315 \pm 0.035$ |
| $\phi_{\omega''}$ (rad) | 0 | 0 | 0 | ... |
| $\sigma_{0\omega}$ (nb) | 0 | $102 \pm 67$ | PDG | ... |
| $\chi^2$/ndf | ... | 34.9/48 | ... | ... |

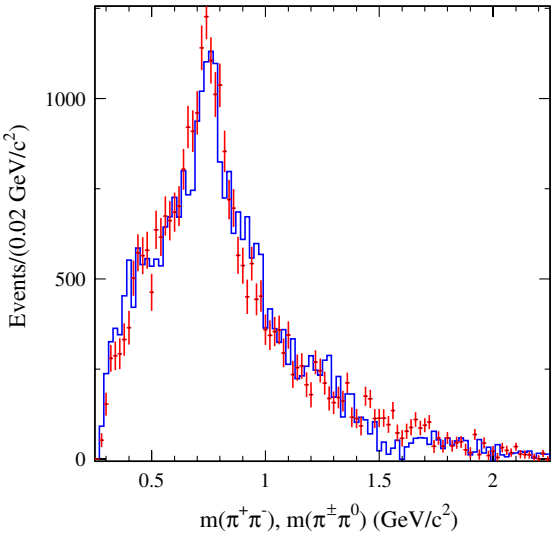


FIG. 55 (color online). The $m(\pi^+\pi^-)$ (points) and $m(\pi^\pm\pi^0)$ (histogram) distributions for $2(\pi^+\pi^-)\pi^0$ events with the $\omega\pi^+\pi^-$ and $\eta\pi^+\pi^-$ contributions excluded. From Aubert *et al.*, 2007c.

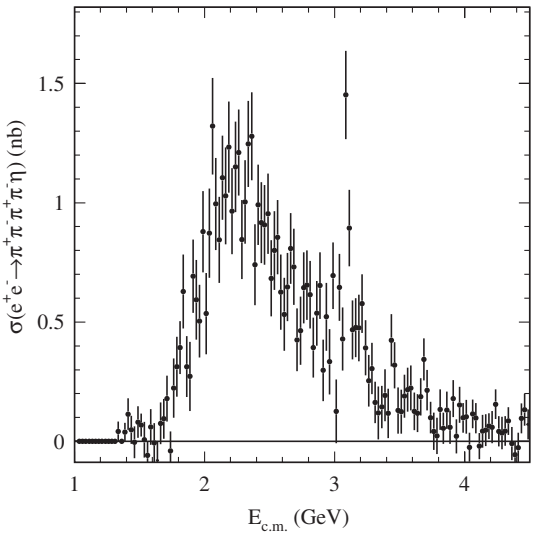


FIG. 56. The $e^+e^- \to 2(\pi^+\pi^-)\eta$ cross section measured by *BABAR*. From Aubert *et al.*, 2007c.

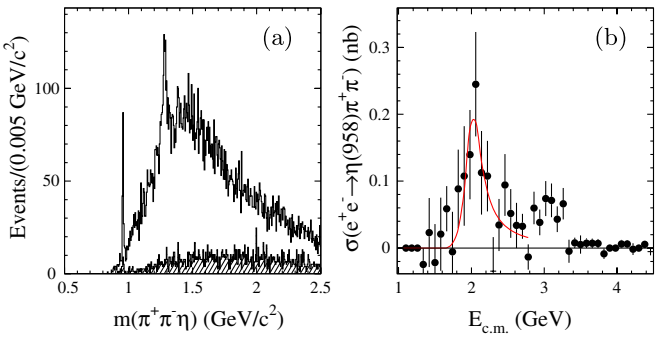


FIG. 57 (color online). (a) The $m(\eta\pi^+\pi^-)$ distribution for $2(\pi^+\pi^-)\eta$ events. (b) The $e^+e^- \to \eta(958)\pi^+\pi^-$ cross section and the result of the Breit-Wigner fit. From Aubert *et al.*, 2007c.

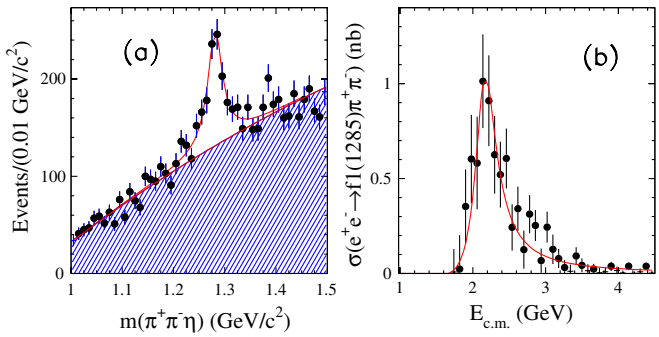


FIG. 58 (color online). (a) The $m(\eta\pi^+\pi^-)$ distribution for $2(\pi^+\pi^-)\eta$ events. (b) The $e^+e^- \to f_1(1285)\pi^+\pi^-$ cross section and the result of the Breit-Wigner fit. From Aubert *et al.*, 2007c.

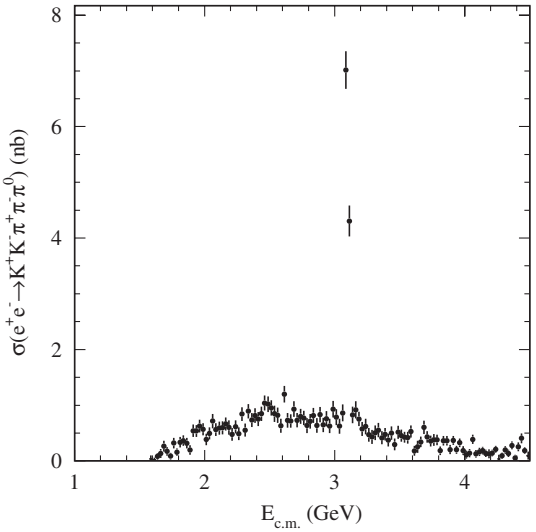


FIG. 59. The $e^+e^- \to K^+K^-\pi^+\pi^-\pi^0$ cross section measured by *BABAR*. From Aubert *et al.*, 2007c.

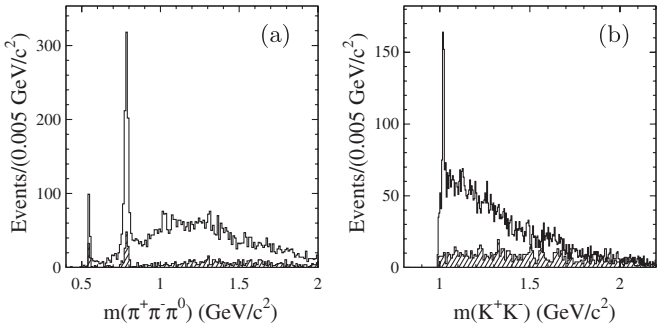


FIG. 60. (a) The $m(\pi^+\pi^-\pi^0)$ and (b) $m(K^+K^-)$ distributions for $K^+K^-\pi^+\pi^-\pi^0$ events. The hatched histogram represents the estimated non-ISR background. From Aubert *et al.*, 2007c.

$\rho(770)$ only, neutral or charged, per event is observed in the expected proportion 1:2.

In the $2(\pi^+\pi^-\pi^0)$ final state, $\eta$ and $\omega$ signals are seen in the $\pi^+\pi^-\pi^0$ invariant-mass distribution. A small fraction of events corresponds to the associated production of the $\eta$ and $\omega$. Selecting these $\eta\omega$ events the $e^+e^- \to \omega\eta$ cross section

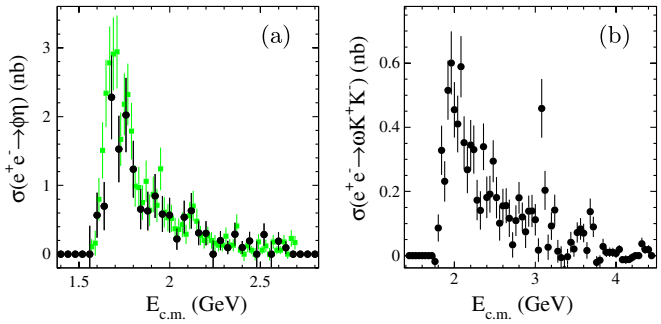


FIG. 61 (color online). (a) The $e^+e^- \to \phi\eta$ cross section measured by *BABAR* in the $K^+K^-\pi^+\pi^-\pi^0$ (Aubert *et al.*, 2007c) (circles) and $K^+K^-\gamma\gamma$ (squares) (Aubert *et al.*, 2008b) final states. (b) The cross sections for the $e^+e^- \to \omega K^+K^-$ process measured by *BABAR* (Aubert *et al.*, 2007c).

shown in Fig. 62 (left) was measured for the first time. The observed resonance structure which is expected to be the $\omega(1650)$ is fitted with a Breit-Wigner function. The fitted curve is shown in Fig. 62 (left). The obtained resonance parameters are listed in Table II together with the resonance parameters obtained from the fits to $e^+e^- \to 3\pi$ and $e^+e^- \to \omega\pi\pi$ cross sections (see Sec. III.J). Comparison of the $\omega 3\pi$ and $\omega(782)\eta$ contributions with the total $e^+e^- \to 2(\pi^+\pi^-\pi^0)$ cross section is shown in Fig. 62 (right).

The total $e^+e^- \to 2(\pi^+\pi^-\pi^0)$ and $e^+e^- \to 3(\pi^+\pi^-)$ cross sections shown in Fig. 63 have similar energy dependence. The ratio of the cross sections is almost constant over the energy range under study. Its average value is equal to $3.98 \pm 0.06 \pm 0.41$. A dip structure just below 2 GeV in the six-pion cross section was observed in the DM2 experiment (Castro, 1988) and then confirmed in the diffractive photoproduction of six pions in the FOCUS experiment (Frabetti *et al.*, 2001). Such a dip at 1.9 GeV was also observed in the total cross section of $e^+e^-$ annihilation into hadrons by the FENICE detector (Antonelli *et al.*, 1996). This structure in *BABAR* data is fitted using the Breit-Wigner function coherent with the smooth nonresonant background. The fitted curves for both cross sections are shown in Fig. 63. The following "resonance" parameters are obtained:

$$m_{6\pi} = 1.88 \pm 0.03\ \text{GeV}/c^2,$$
$$m_{4\pi 2\pi^0} = 1.86 \pm 0.02\ \text{GeV}/c^2,$$
$$\Gamma_{6\pi} = 0.13 \pm 0.03\ \text{GeV},$$
$$\Gamma_{4\pi 2\pi^0} = 0.16 \pm 0.02\ \text{GeV}.$$

The parameter values seem to be essentially independent of the final-state charge combination. These values may also be compared with those obtained in the FOCUS experiment (Frabetti *et al.*, 2001): $m = 1.91 \pm 0.01\ \text{GeV}/c^2$, $\Gamma = 0.037 \pm 0.013$ GeV. The mass values are consistent, but the widths obtained by *BABAR* are substantially larger. Note that typical widths of known isovector resonances with mass near $2\ \text{GeV}/c^2$ are 200–300 MeV. Since the obtained mass of the resonance structure is close to the double proton mass, it may be interpreted as a proton-antiproton subthreshold bound state (Datta and O'Donnell, 2003).

### J. Summary

The *BABAR* ISR study covers the low-energy range of $e^+e^-$ interactions from the $2\pi$ threshold to 4.0–4.5 GeV with exclusively measured cross sections for many processes. Figure 64 shows all exclusive cross sections measured by *BABAR* in a single plot. One can see that in most of the cases cross sections strongly depend on energy and their central values vary by 5 orders of magnitude.

One of the purposes of the *BABAR* ISR program was to measure the total hadronic cross section in the energy range below 2 GeV with improved accuracy (Druzhinin, 2007). To finalize this program, the cross sections at least for the $\pi^+\pi^-3\pi^0$, $\pi^+\pi^-4\pi^0$, $K^+K^-$, $K_SK_L$, $K_SK_L\pi\pi$, and $K_SK^\pm\pi^\mp\pi^0$ final states should be additionally measured.

Note that the total cross section value is not the direct sum of the cross sections shown in Fig. 64. Each channel has internal subprocesses which include different resonances with

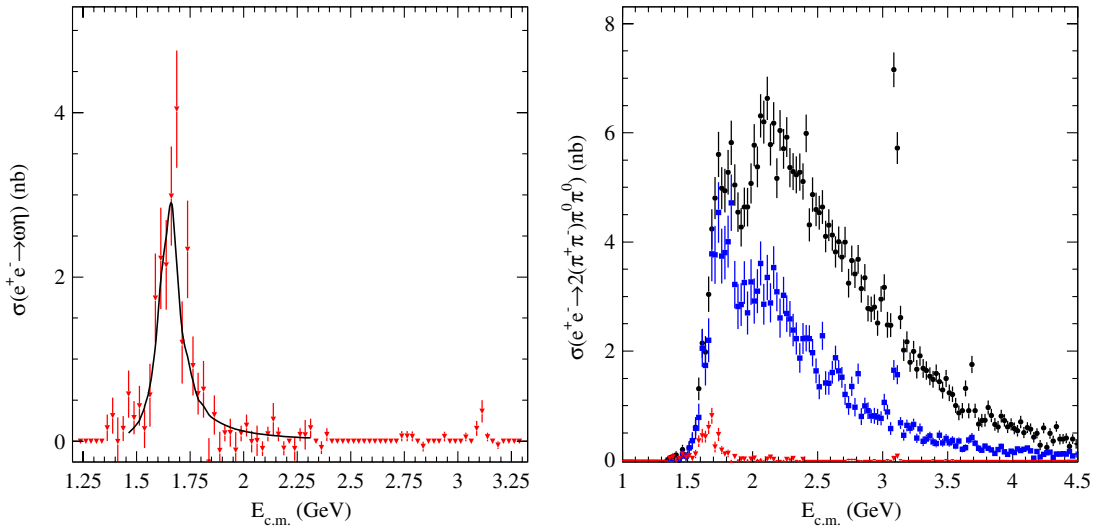


FIG. 62 (color online). The $e^+e^- \to \omega\eta$ cross section (left) and contribution of $e^+e^- \to \omega\pi^+\pi^-\pi^0$ (squares) and $e^+e^- \to \omega\eta$ (triangles) cross sections to all $e^+e^- \to 2(\pi^+\pi^-\pi^0)$ events (right). From Aubert *et al.*, 2006b.

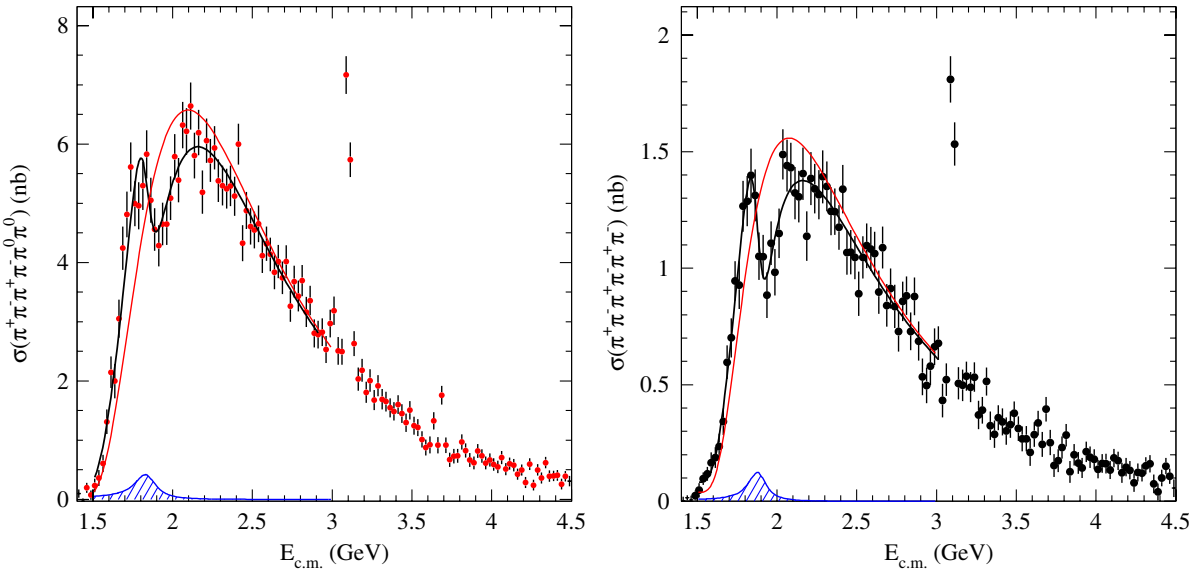


FIG. 63 (color online). The $e^+e^- \to 2(\pi^+\pi^-\pi^0)$ cross section (left) and the $e^+e^- \to 3(\pi^+\pi^-)$ cross section (right) with a fit to the (anti) resonance function. A resonance responsible for the "dip" is shown shaded. From Aubert *et al.*, 2006b.

different branching fractions to the observed final states. To perform a correct summation, each subchannel should be extracted separately and corrected for the decay rate of an internal resonance.

The exclusive ISR study of hadron production allows one to investigate and improve our knowledge of excited states for light vector mesons. For most of them the parameters are still rather imprecise and new investigations are needed.

For multihadron final states it may be difficult to isolate the contributions of particular vector resonances due to the presence of many interfering intermediate states. An example is the reaction $e^+e^- \to \pi^+\pi^-\pi^0\pi^0$, where the $\omega\pi^0$, $a_1\pi$, and $\rho^+\rho^-$ intermediate states give dominant contributions. The two latter states contain wide resonances and strongly interfere. A partial-wave analysis is required to separate the subprocesses of the $e^+e^- \to \pi^+\pi^-\pi^0\pi^0$ and $e^+e^- \to \pi^+\pi^-\pi^+\pi^-$ reactions. We hope that *BABAR* has enough data to perform such an analysis. This is necessary to separate contributions of two excited $\rho$ states, $\rho(1450)$ and $\rho(1700)$, and determine their parameters. A detailed study of intermediate mechanisms strongly benefits from the quasi-two-body character of some final states, but is much more difficult for multibody final states.

The *BABAR* ISR data on isoscalar channels already allow one to improve parameters of excited $\phi$ and $\omega$ states. A global fit to the isovector and isoscalar components for the

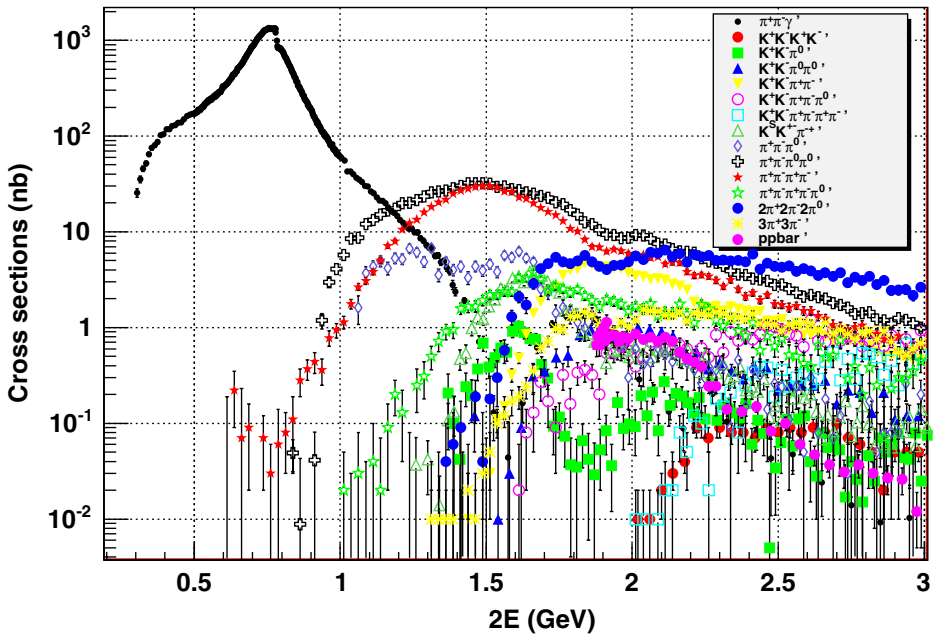


FIG. 64 (color online). The cross sections of $e^+e^- \to$ hadrons measured with the *BABAR* detector via ISR. The results on $e^+e^- \to \pi^+\pi^-\pi^0\pi^0$ are preliminary.

process $e^+e^- \to K^*(892)\bar{K}$, and the $e^+e^- \to \phi\eta$ cross section (Buon *et al.*, 1982) was used to determine parameters of the $\phi(1680)$ resonance (see Table I).

In Table II we summarize the results of the fits to the $e^+e^- \to 3\pi$, $e^+e^- \to \omega\pi\pi$, and $e^+e^- \to \omega\eta$ cross sections performed by *BABAR* (Aubert *et al.*, 2004b, 2006b, 2007c) and compare them with the corresponding PDG (Amsler *et al.*, 2008) parameters. A simultaneous fit to all three channels could significantly improve the results and give additional information on relative decay rates.

Because of numerous extensive studies of various exclusive cross sections, we have learned a lot about the total cross section of $e^+e^-$ annihilation into hadrons and its components allowing a more precise estimation of hadronic vacuum polarization effects to be performed (see also Sec. VII).

## IV. BARYON FORM FACTORS

### A. General formulas

The cross section of the process $e^+e^- \to \mathcal{B}\bar{\mathcal{B}}$, where $\mathcal{B}$ is a spin-1/2 baryon, is given by (Renard, 1981)

$$\frac{d\sigma}{d\Omega} = \frac{\alpha^2\beta C}{4s}\left(|G_M(s)|^2(1+\cos^2\theta) + \frac{1}{\tau}|G_E(s)|^2\sin^2\theta\right), \tag{11}$$

where $\beta = \sqrt{1-4m_{\mathcal{B}}^2/s}$ and $m_{\mathcal{B}}$ are the baryon velocity ($v/c$) and mass, $C = y/(1-e^{-y})$ with $y = \pi\alpha m_{\mathcal{B}}/\beta\sqrt{s}$ is the Coulomb correction factor (Tzara, 1970) for charged baryons ($C = 1$ for neutral baryons), $\tau = s/4m_{\mathcal{B}}^2$ is the inverse helicity suppression factor, and $G_M$ and $G_E$ are the baryon magnetic and electric form factors. The number of form factors corresponds to two $\mathcal{B}\bar{\mathcal{B}}$ states with different angular momenta: $^3S_1$ and $^3D_1$. At the $\mathcal{B}\bar{\mathcal{B}}$ threshold the $D$-wave state vanishes, and $|G_E| = |G_M|$. At high $\sqrt{s}$ the terms containing $G_E$ are suppressed by the helicity factor $1/\tau$. With unpolarized beams the total cross section is

$$\sigma(s) = \frac{4\pi\alpha^2\beta C}{3s}\left[|G_M(s)|^2 + \frac{1}{2\tau}|G_E(s)|^2\right]. \tag{12}$$

As discussed previously (see Secs. II.A and II.D and Fig. 7), the detection efficiency in the ISR measurement with a tagged photon has weak dependence on the angular distributions of final hadrons. In the case of the dibaryon production this allows one to measure the total cross section [Eq. (12)] independently of the relation between the electric and magnetic form factors. The ratio of the form factors can then be determined from an analysis of the baryon angular distribution. In direct $e^+e^-$ or $p\bar{p}$ experiments the range of the accessible polar angles is limited by the detector acceptance. In this case the cross section cannot be measured in a model-independent way. The detection efficiency is determined, and the proton magnetic form factor $|G_M|$ is extracted, usually under the assumption that $|G_M| = |G_E|$. In the *BABAR* paper (Aubert *et al.*, 2006a) on the ISR study of the reaction $e^+e^- \to p\bar{p}$, the effective form factor is introduced as a linear combination of $|G_M|^2$ and $|G_E|^2$:

$$|F(s)|^2 = \frac{2\tau|G_M(s)|^2 + |G_E(s)|^2}{2\tau+1}. \tag{13}$$

With the effective form factor the total cross section looks like

$$\sigma_0(s) = \frac{4\pi\alpha^2\beta C}{3s}\left(1+\frac{1}{2\tau}\right)|F(s)|^2. \tag{14}$$

The effective form factor defined in such a way allows an easy comparison of the results of the model-independent ISR measurement with $|G_M|$ obtained in direct $e^+e^-$ and $p\bar{p}$ experiments under the assumption that $|G_M| = |G_E|$.

The modulus of the ratio of the electric and magnetic form factors can be determined from the analysis of the baryon polar-angle distribution. This distribution can be presented as a sum of the terms proportional to $|G_M|^2$ and $|G_E|^2$. For the $e^+e^- \to p\bar{p}\gamma$ cross section the fully differential formula can be found in Czyż *et al.* (2004). In this process the $\theta_p$ dependences of the $G_E$ and $G_M$ terms are not strongly different from $\sin^2\theta_p$ and $1+\cos^2\theta_p$, describing the angular distributions for the electric and magnetic form factors in Eq. (11). Note that in direct $e^+e^-$ experiments with transversely polarized beams a study of the proton azimuthal angle distribution can improve $G_E/G_M$ separation [see Eq. (13)].

A nonzero relative phase between the electric and magnetic form factors manifests itself in a polarization of the outgoing baryons. In the reaction $e^+e^- \to \mathcal{B}\bar{\mathcal{B}}$ this polarization is perpendicular to the production plane (Dubnickova, Dubnicka, and Rekalo, 1996). For the ISR process $e^+e^- \to \mathcal{B}\bar{\mathcal{B}}\gamma$ the polarization observables are analyzed by Czyż, Grzelinska, and Kühn (2007) and Kardapoltzev (2007). In the case of the $\Lambda\bar{\Lambda}$ final state the $\Lambda \to p\pi^-$ decay can be used to measure the $\Lambda$ polarization and hence the phase between the form factors.

### B. Measurement of timelike baryon form factors

Measurements of the $e^+e^- \to p\bar{p}$ cross section have been performed in $e^+e^-$ experiments (Castellano *et al.*, 1973; Delcourt *et al.*, 1979; Bisello *et al.*, 1983, 1990; Antonelli *et al.*, 1998; Ablikim *et al.*, 2005; Pedlar *et al.*, 2005) with a (20–30)% precision. The cross section and the proton form factor were deduced assuming $|G_E| = |G_M|$. More precise measurements of the proton form factor have been performed in $p\bar{p} \to e^+e^-$ experiments (Armstrong *et al.*, 1993; Bardin *et al.*, 1994; Ambrogiani *et al.*, 1999). In the PS170 experiment (Bardin *et al.*, 1994) at LEAR, the proton form factor was measured from threshold ($p\bar{p}$ annihilation at rest) up to a mass of 2.05 GeV/$c^2$. The ratio $|G_E/G_M|$ was measured using the angular dependence of the cross section and was found to be compatible with unity. The LEAR data show a strong dependence of the form factor on $p\bar{p}$ mass near threshold, and a weak dependence in the range 1.95–2.05 GeV/$c^2$. The Fermilab experiments, E760 (Armstrong *et al.*, 1993) and E835 (Ambrogiani *et al.*, 1999), showed that the form factor decreases rapidly at higher masses, in agreement with the perturbative QCD prediction $G_M \propto \alpha_s^2(m^2)/m^4$.

Experimental information on the reactions $e^+e^- \to \Lambda\bar{\Lambda}$, $\Sigma^0\bar{\Sigma}^0$, and $\Lambda\bar{\Sigma}^0$ is scarce. The $e^+e^- \to \Lambda\bar{\Lambda}$ cross section is

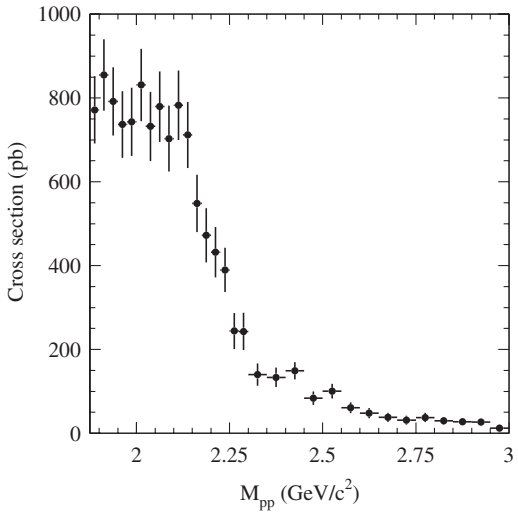


FIG. 65. The $e^+e^- \to p\bar{p}$ cross section measured by *BABAR*. From Aubert *et al.*, 2006a.

measured to be $100^{+65}_{-35}$ pb at 2.386 GeV, and at the same energy the upper limits for $e^+e^- \to \Sigma^0\bar{\Sigma}^0$ ($< 120$ pb) and $e^+e^- \to \Lambda\bar{\Sigma}^0$ ($< 75$ pb) cross sections have been obtained (Bisello *et al.*, 1990).

### C. $e^+e^- \to p\bar{p}\gamma$

The first ISR baryon experiment was the measurement of the proton-antiproton production cross section (Aubert *et al.*, 2006a) by *BABAR*. The measured $e^+e^- \to p\bar{p}$ cross section shown in Figs. 65 and 66 is almost flat near the threshold and then decreases from 1 nb to about 1 pb at 4.5 GeV. There are two rapid drops of the cross section near 2.15 and 2.9 GeV. The *BABAR* proton form factor data presented in Fig. 67, in general, agree with the previous measurements. Figure 68 shows an expanded view of the near-threshold region. The *BABAR* measurement confirms the PS170 observation (Bardin *et al.*, 1994) of the significant increase in the form factor for energies approaching the $p\bar{p}$ threshold. The proton form factor reaches about 0.6 at the threshold.

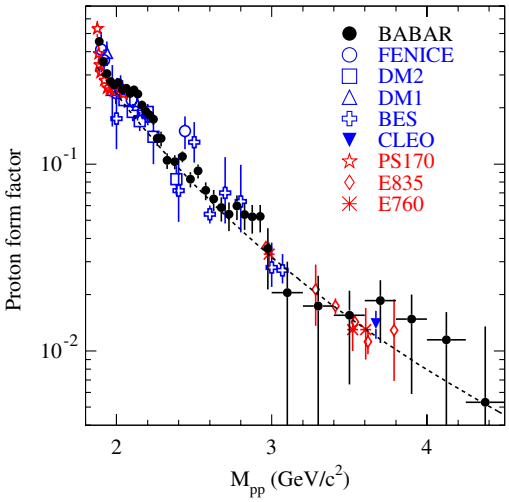


FIG. 67 (color online). The proton form factor measured in different experiments (Delcourt *et al.*, 1979; Bisello *et al.*, 1983; Armstrong *et al.*, 1993; Bardin *et al.*, 1994; Antonelli *et al.*, 1998; Ambrogiani *et al.*, 1999; Ablikim *et al.*, 2005; Pedlar *et al.*, 2005; Aubert *et al.*, 2006a). The dashed line represents the QCD fit described in the text.

A study of the proton angular distribution allows one to extract the value of the ratio of the electric and magnetic form factors $|G_E/G_M|$. The results of the *BABAR* $|G_E/G_M|$ measurement are shown in Fig. 69 in comparison with the data obtained at LEAR (Bardin *et al.*, 1994). In disagreement with the LEAR result, the *BABAR* data indicate that $|G_E/G_M|$ significantly exceeds unity in the energy range between threshold and 2.1 GeV.

### D. $e^+e^- \to \Lambda\bar{\Lambda}\gamma$

The $e^+e^- \to \Lambda\bar{\Lambda}$ cross section measured by the *BABAR* detector (Aubert *et al.*, 2007d) is shown in Fig. 70 in

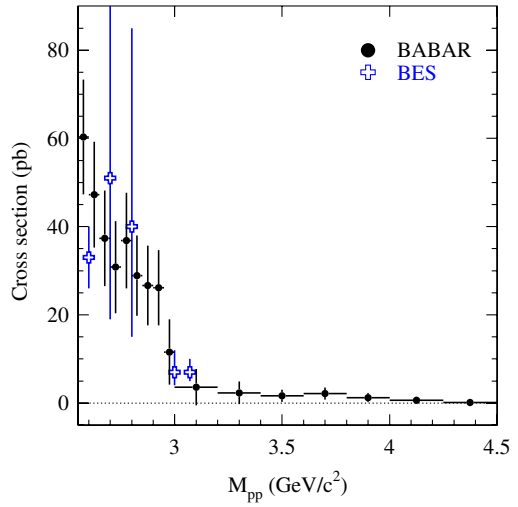


FIG. 66 (color online). The $e^+e^- \to p\bar{p}$ cross section measured by *BABAR* (Aubert *et al.*, 2006a) in comparison with the BES data (Ablikim *et al.*, 2005).

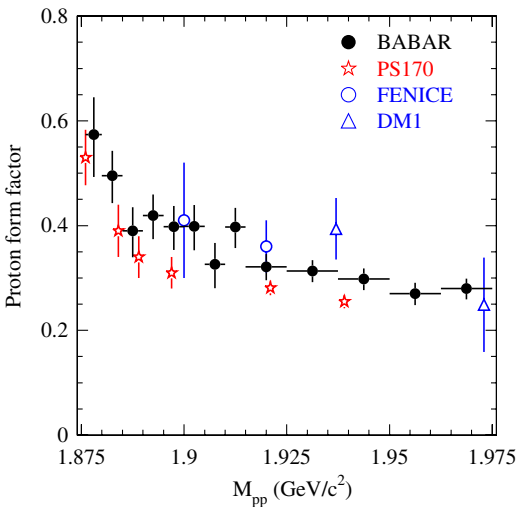


FIG. 68 (color online). The proton form factor in the near-threshold region (Delcourt *et al.*, 1979; Bardin *et al.*, 1994; Antonelli *et al.*, 1998; Aubert *et al.*, 2006a).

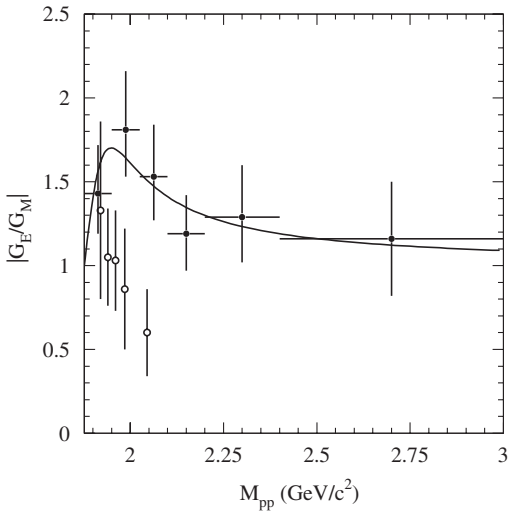


FIG. 69. The proton $|G_E/G_M|$ ratio measured by *BABAR* (Aubert *et al.*, 2006a) (solid circles) compared with LEAR data (Bardin *et al.*, 1994) (open circles).

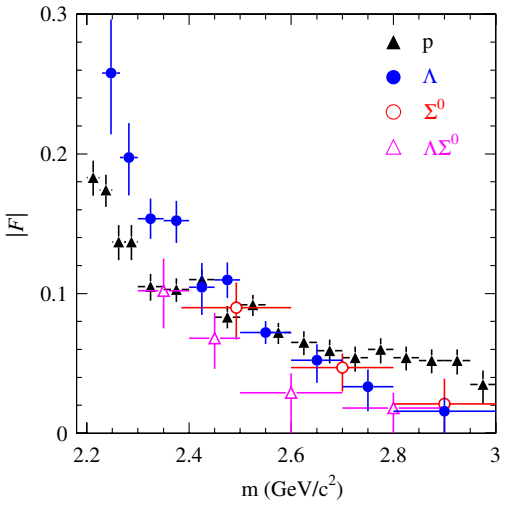


FIG. 71 (color online). The baryon form factors measured by *BABAR* (Aubert *et al.*, 2006a, 2007d) vs the dibaryon invariant mass.

comparison with the only previous measurement (Bisello *et al.*, 1990). The *BABAR* measurement is based on about 200 $\Lambda\bar{\Lambda}$ events selected in the decay mode $\Lambda \to p\pi$.

The measured $\Lambda$ effective form factor is shown in Fig. 71. The ratio $|G_E/G_M|$ is found to be consistent with unity. The use of the $\Lambda \to p\pi$ decay allows one to measure the relative phase $\phi_\Lambda$ between the complex $G_E$ and $G_M$ form factors. A nonzero $\phi_\Lambda$ leads to polarization $\zeta$ of the outgoing baryons. The value of $\zeta$ is extracted from the analysis of the proton angular distribution in the $\Lambda \to p\pi$ decay. The measured $\cos\theta_{p\zeta}$ distribution, where $\theta_{p\zeta}$ is the angle between the $\Lambda$ polarization vector and the proton momentum in the $\Lambda$ rest frame, is shown in Fig. 72. No $\cos\theta_{p\zeta}$ distribution asymmetry corresponding to the nonzero polarization is seen. Because of the limited data sample only a weak limit on the phase between $G_E$ and $G_M$ has been set for the $\Lambda$ hyperon $-0.76 < \sin\phi_\Lambda < 0.98$.

### E. $e^+e^- \to \Sigma^0\bar{\Sigma}^0$, $\Lambda\bar{\Sigma}^0(\Sigma^0\bar{\Lambda})$

The *BABAR* measurement of the $\Sigma^0$ and $\Sigma^0\Lambda$ form factors is described by Aubert *et al.* (2007d). The decay chain $\Sigma^0 \to \Lambda\gamma \to p\pi\gamma$ is used to reconstruct $\Sigma^0$. About 20 candidate events were selected for each of the ISR reactions $e^+e^- \to \Sigma^0\bar{\Sigma}^0\gamma$ and $e^+e^- \to \Sigma^0\bar{\Lambda}\gamma$. The effective $\Sigma^0$ and $\Sigma^0\Lambda$ form factors are shown in Fig. 71. The corresponding values of the $e^+e^- \to \Sigma^0\bar{\Sigma}^0$ and $e^+e^- \to \Sigma^0\bar{\Lambda}$ cross sections are about 40 pb near the reaction thresholds. It can be seen that the $\Lambda$, $\Sigma^0$, and $\Sigma^0\Lambda$ form factors are of the same order.

### F. Summary

The baryon form factors are a subject of various phenomenological models [see Baldini *et al.* (2009) and references therein]. QCD predicts for the baryon form factor the asymptotic behavior $F(q^2) \sim \alpha_s^2(q^2)/q^4$ (Chernyak and Zhitnitsky,

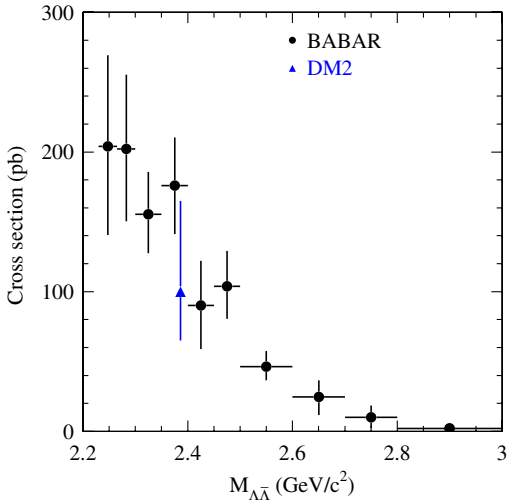


FIG. 70 (color online). The $e^+e^- \to \Lambda\bar{\Lambda}$ cross section measured by *BABAR* (Aubert *et al.*, 2007d) in comparison with the DM2 measurement (Bisello *et al.*, 1990).

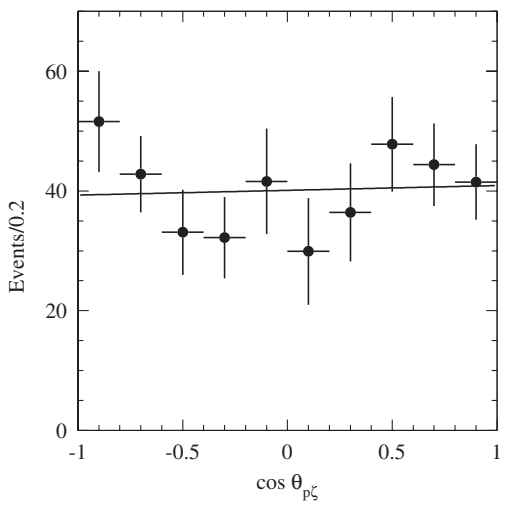


FIG. 72. The $\cos\theta_{p\zeta}$ distribution in the $e^+e^- \to \Lambda\bar{\Lambda}$ process. The line represents the result of the fit to data with a first-order polynomial. From Aubert *et al.*, 2007d.

1977). Comparison of this prediction with the data on the proton form factor is shown in Fig. 67. It can be seen that the asymptotic regime is reached at energies higher than 3 GeV.

The remarkable feature of the process $e^+e^- \to p\bar{p}$ is a nearly flat cross section in the 200-MeV region above the $p\bar{p}$ threshold. This feature is explained by Baldini *et al.* (2009) by the opposite trends in the energy dependence of the $S$- and $D$-wave contributions.

A natural explanation for the sharp increase of the proton form factor in the vicinity of the $p\bar{p}$ threshold is the final state interaction of the proton and antiproton [see Dmitriev and Milstein (2007) and references therein]. Another possibility is a contribution of the vector-meson state located just below the $p\bar{p}$ threshold. This state is observed in the reaction $e^+e^- \to 6\pi$ (Castro, 1988; Frabetti *et al.*, 2001; Aubert *et al.*, 2006b).

The rapid drop of the cross section at 2.15 GeV may be a manifestation of the isovector state $\rho(2150)$, which is seen in the reactions $e^+e^- \to \eta'\pi^+\pi^-$ and $e^+e^- \to f_1(1285)\pi^+\pi^-$ (Aubert *et al.*, 2007c). The drop in the cross section near 2.9 GeV is still not understood.

The $e^+e^- \to \Lambda\bar{\Lambda}$ cross section has some features similar to those for the process $e^+e^- \to p\bar{p}$. In the energy region of about 200 MeV above threshold the $\Lambda\bar{\Lambda}$ cross section is flat; the $G_E/G_M$ ratio is consistent with that measured by *BABAR* for the $e^+e^- \to p\bar{p}$. An attempt to explain the unusual energy dependence of the $e^+e^- \to \Lambda\bar{\Lambda}$ cross section was made by Baldini *et al.* (2009). A fit to the $\Lambda$ form factor with the power-law function const$/q^n$ (see Fig. 73) gives $n = 9.2 \pm 0.3$. This $n$ value strongly differs from the QCD asymptotic prediction $n = 4$. Similar to the $p\bar{p}$ case, the asymptotic regime is not reached for $e^+e^- \to \Lambda\bar{\Lambda}$ at the energies below 3 GeV.

The cross sections of the processes $e^+e^- \to \Sigma^0\bar{\Sigma}^0$ and $e^+e^- \to \Lambda\bar{\Sigma}^0(\Sigma^0\bar{\Lambda})$ have been measured with large uncertainties. The corresponding $\Sigma^0$ and $\Sigma^0\Lambda$ form factors (see Fig. 71) show a monotonic decrease starting just from the threshold. A fit to form factor data with the power-law function gives $n > 4$ but with large errors.

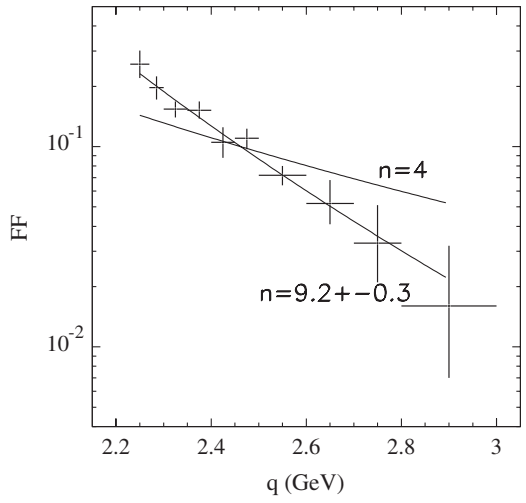


FIG. 73. A fit of the $\Lambda$ form factor with the power-law function $F \sim \text{const}/q^n$ and with the QCD-inspired function $F \sim \text{const}/q^4$. From Aubert *et al.*, 2007d.

It is interesting to compare the measured form factors with each other and with the QCD prediction for the asymptotic form factor ratios (Chernyak *et al.*, 1989): $F_p = 4.1F_\Lambda$, $F_{\Sigma^0} = -1.18F_\Lambda$, and $F_{\Sigma^0\Lambda} = -2.34F_\Lambda$. From comparison of the form factors in Fig. 71, it can be seen that the prediction works only for the ratios of the $\Lambda$ and $\Sigma^0$ form factors. The ratio $F_\Lambda/F_p$ decreases with energy. In the highest-energy interval 2.8–3.00 GeV the ratio is equal to $0.3^{+0.2}_{-0.3}$ and agrees with the asymptotic value of 0.24. This is an indication that the asymptotic regime is reached just above 3 GeV.

The *BABAR* experiment shows that the ISR method is well suited for the measurement of baryon form factors. Future Super $B$ factories as well as an already running BEPC $e^+e^-$ collider will make it possible for measurements of the form factors, especially for the proton, with unprecedented accuracy. High-precision measurements of the proton form factor are also planned in the PANDA experiment.

## V. DECAYS OF THE $J/\psi$ AND $\psi(2S)$

For all processes described in the previous sections, clear narrow peaks are seen in the energy dependence of the cross sections corresponding to the $J/\psi$ and $\psi(2S)$ decays. The Born cross section for the ISR production of a narrow resonance, for example, the $J/\psi$, decaying to the final state $h$ can be calculated using (Aubert *et al.*, 2004a)

$$\sigma_{J/\psi} = \frac{12\pi^2\Gamma(J/\psi \to e^+e^-)\mathcal{B}(J/\psi \to h)}{sm_{J/\psi}} W_0(\theta_0, x_{J/\psi}), \tag{15}$$

where $m_{J/\psi}$ and $\Gamma(J/\psi \to e^+e^-)$ are the mass and electronic width of the $J/\psi$ meson, $x_{J/\psi} = 1 - m^2_{J/\psi}/s$, and $\mathcal{B}(J/\psi \to h)$ is the branching fraction for the $J/\psi$ decay to the final state $h$. The function $W_0$ is described in Sec. I.C by Eq. (7). Therefore, a measurement of the number of $J/\psi \to h$ decays in the ISR process $e^+e^- \to h\gamma$ determines the product of the electronic width and the branching fraction $\Gamma(J/\psi \to e^+e^-)\mathcal{B}(J/\psi \to h)$.

The total cross section for the process $e^+e^- \to \gamma J/\psi$ with a tagged ISR photon ($\theta_0 = 30°$) is about 3.4 pb. With the integrated luminosity of ~500 fb$^{-1}$ collected by the *BABAR* detector it corresponds to about $1.7 \times 10^6$ produced $J/\psi$'s. This number is significantly smaller than, for example, about $60 \times 10^6$ $J/\psi$'s produced in the BESII experiment at the BEPC $e^+e^-$ collider. However, the general quality of the *BABAR* detector and its particle identification, in particular, are much better compared to the BESII detector. As a result, the detector efficiency and the integrated luminosity are determined with lower systematic errors. A typical systematic uncertainty of the *BABAR* measurement is 3%–5%, while BESII usually quotes 10%–15%. The lower systematic error makes ISR results on many $J/\psi$ decays competitive with BESII and other previous measurements. Practically all decays with rates about $10^{-3}$ and higher can be measured via ISR with better overall accuracy. Moreover, because of excellent particle identification, many $J/\psi$ and $\psi(2S)$ decays with kaons in the final state have been studied using ISR for the first time.

In the *BABAR* experiment the ISR method enables one to measure a few tens of $J/\psi$ and $\psi(2S)$ decays with the best-to-date accuracy and discover about 20 new decays of these resonances.

### A. Leptonic decays

The *BABAR* (Aubert *et al.*, 2004a) and CLEO (Adams *et al.*, 2006) Collaborations performed a study of the $J/\psi$ production in the reaction $e^+e^- \to \mu^+\mu^-\gamma$. The dimuon mass spectrum for this reaction obtained by *BABAR* is shown in Fig. 74. The signal of the ISR $J/\psi$ production is seen well in the mass spectrum. The nonresonant spectrum is due to muon pair production in the process $e^+e^- \to \mu^+\mu^-\gamma$, where a photon can be emitted by both initial electrons and final muons. Since the dimuon decay of the $J/\psi$ meson proceeds through a single-photon transition, $J/\psi \to \gamma^* \to \mu^+\mu^-$, the angular and momentum distributions for events from the $J/\psi$ peak are completely identical to those for the ISR part of nonresonant events. The idea of the *BABAR* measurement is to determine the ratio of the number of $J/\psi$ events to the level of the nonresonant spectrum which is well known theoretically. The dimuon spectrum of Fig. 74 has been fit with a function taking into account the energy dependence of the nonresonant cross section and the experimental $J/\psi$ line shape. The ratio

$$r = \frac{N_{J/\psi}}{(dN/dm)\Delta m} \tag{16}$$

was the main fit parameter. After substituting cross sections for the numbers of events, this ratio can be rewritten as

$$r = \frac{\sigma^{\rm Born}_{J/\psi}}{(d\sigma^{\rm Born}_{\rm ISR}/dm)\Delta m}\frac{1}{K}, \qquad K = \frac{d\sigma^{\rm vis}_{\rm Total}/dm}{d\sigma^{\rm vis}_{\rm ISR}/dm}. \tag{17}$$

Detector acceptances and ISR radiative corrections, which are the same for the nonresonant ISR and $J/\psi$ contributions to the reaction $e^+e^- \to \mu^+\mu^-\gamma$, cancel in the ratio. The total nonresonant cross section includes the FSR contribution, which is parametrized in terms of $K$, the ratio of the visible nonresonant total and ISR-only (FSR switched off) cross sections. Since *BABAR* selects events with the photon emitted at a large angle, the FSR contribution is relatively large. Using simulated events, the coefficient $K = 1.11 \pm 0.01$ (statistical error only) is determined for the selection criteria used.

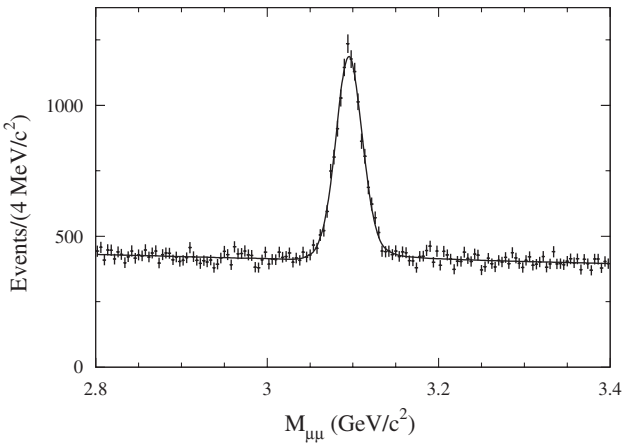


FIG. 74. The $\mu^+\mu^-$ mass spectrum in the $J/\psi$ region for selected events of the reaction $e^+e^- \to \mu^+\mu^-\gamma$. The curve is the result of the fit described in the text. From Aubert *et al.*, 2004a.

The result of the fit is shown in Fig. 74. The value $r = 18.94 \pm 0.44$ is found with $\chi^2/\text{ndf} = 122/144$. From the product $rK = 21.03 \pm 0.49 \pm 0.47$, the cross section $\sigma_{J/\psi} = 2124 \pm 49 \pm 47$ fb and the product of the $J/\psi$ parameters

$$\Gamma_{ee}B_{\mu\mu} = 0.3301 \pm 0.0077 \pm 0.0073 \text{ keV}$$

are determined. The main sources of the systematic error quoted are uncertainties in the $J/\psi$ line shape and the coefficient $K$, both due to imperfect simulation of the detector response.

Using the values for $B_{ee}$ and $B_{\mu\mu}$ (Eidelman *et al.*, 2004), which are well measured in the cascade $\psi(2S) \to J/\psi\pi^+\pi^-$ decays (Bai *et al.*, 1998), the electronic and total widths of the $J/\psi$ meson were derived,

$$\Gamma_{ee} = 5.61 \pm 0.20 \text{ keV}, \qquad \Gamma = 94.7 \pm 4.4 \text{ keV}.$$

These were the best-to-date measurements of the $J/\psi$ parameters.

The *BABAR* measurement was improved by CLEO. With an integrated luminocity of 281 pb$^{-1}$ collected at $\sqrt{s} = 3.77$ GeV about $13 \times 10^3$ ISR-produced $J/\psi \to \mu^+\mu^-$ events were selected (compared to $8 \times 10^3$ $J/\psi \to \mu^+\mu^-$ events in the *BABAR* measurement based on a 88 fb$^{-1}$ data sample). Since CLEO used the untagged approach, the FSR contribution to the nonresonant cross section was significantly reduced. The second important improvement of the method was that the $J/\psi$ line shape was extracted from data. To do this, the data collected by CLEO at the $\psi(2S)$ resonance were used to select a clean sample of $\psi(2S) \to J/\psi\pi^+\pi^-$, $J/\psi \to \mu^+\mu^-$ events. The CLEO result for the product of the $J/\psi$ parameters is

$$\Gamma_{ee}\mathcal{B}_{\mu\mu} = 0.3384 \pm 0.0058 \pm 0.0071 \text{ keV}.$$

Despite the analysis improvements described above, the systematic error of the CLEO result was not reduced compared to the *BABAR* measurement. However, the sources of the systematic uncertainties are different for the two measurements. As such the results can be considered as completely independent.

The data collected at $\sqrt{s} = 3.77$ GeV were used by CLEO to study $\psi(2S)$ ISR production (Adam *et al.*, 2006). ISR $\psi(2S)$ events were selected in the decay modes $\psi(2S) \to \pi^+\pi^- J/\psi$, $\pi^0\pi^0 J/\psi$, and $\eta J/\psi$ with the $J/\psi$ decaying to the lepton pair, $e^+e^-$ or $\mu^+\mu^-$. From the number of the $\psi(2S)$ events the products $\Gamma(\psi(2S) \to e^+e^-)\mathcal{B}(\psi(2S) \to XJ/\psi)$, where $X = \pi^+\pi^-$, $\pi^0\pi^0$, and $\eta$, were obtained. Since the branching fractions for these decay modes are known with 1.5%–2% accuracy (Amsler *et al.*, 2008), the measurement of the products can by used to improve accuracy of the $\psi(2S)$ electronic width. The CLEO result dominates in the current PDG value $\Gamma(\psi(2S) \to e^+e^-) = 2.36 \pm 0.04$ keV (Amsler *et al.*, 2008).

### B. Decays to light mesons and baryons

A systematic study of the $J/\psi$ and $\psi(2S)$ decays to light hadrons was performed in the *BABAR* experiment (Aubert *et al.*, 2004b, 2005b, 2006a, 2006b, 2007c, 2007d). An example of the $J/\psi$ signal for $J/\psi \to \pi^+\pi^-\pi^0$, one of the most probable $J/\psi$ decay modes, is shown in Fig. 75 (Aubert *et al.*, 2004b). It can be seen that the nonresonant background is small. From the number of events at the peak, the product $\Gamma(J/\psi \to e^+e^-)B(J/\psi \to 3\pi) = 0.122 \pm 0.005 \pm 0.008$ keV was determined. Using the $J/\psi$ electronic width value, known from the ISR study of the $J/\psi \to \mu^+\mu^-$ decay, the branching fraction $B(J/\psi \to 3\pi) = (2.18 \pm 0.19)\%$ was calculated, which differed by about 50% from the PDG value, $(1.47 \pm 0.13)\%$, available when the analysis (Aubert *et al.*, 2004b) was carried out. A similar deviation was observed in the BES experiment (Bai *et al.*, 2004), where $B(J/\psi \to 3\pi) = (2.10 \pm 0.11)\%$ was obtained.

Another example of a $J/\psi$ decay mode with a rather high probability, which was studied using ISR, is shown in Fig. 76, where the signals of $J/\psi \to 2(\pi^+\pi^-)\pi^0$ and $\psi(2S) \to 2(\pi^+\pi^-)\pi^0$ are clearly seen (Aubert *et al.*, 2007c). Again, by determining the number of peak events over the nonresonant background and using Eq. (15), the product $\Gamma(J/\psi \to e^+e^-)B(J/\psi \to \pi^+\pi^-\pi^+\pi^-\pi^0) = (3.03 \pm 0.05 \pm 0.18) \times 10^{-4}$ keV was determined. The value of the $J/\psi \to \pi^+\pi^-\pi^+\pi^-\pi^0$ branching fraction obtained from this product, $(5.46 \pm 0.09 \pm 0.34)\%$, differed by about $5\sigma$ from the PDG value, $(3.37 \pm 0.26)\%$, available when the analysis (Aubert *et al.*, 2007c) was carried out. As shown in Sec. III.H, the five-pion final state includes production of many intermediate resonances. All of them are seen in the $J/\psi \to 5\pi$ decay. This may be a source of the systematic error unaccounted for in previous measurements of the decay. The detection efficiency in the ISR method with a tagged photon is weakly sensitive to the dynamics of the $J/\psi \to 5\pi$ decay. The model uncertainty in the detection efficiency for the *BABAR* measurement (Aubert *et al.*, 2007c) was estimated from the difference in efficiency values for phase-space generated five-pion events and events generated for the $\omega\pi^+\pi^-$ or $\eta\pi^+\pi^-$ final states. It was found to be less than 3%.

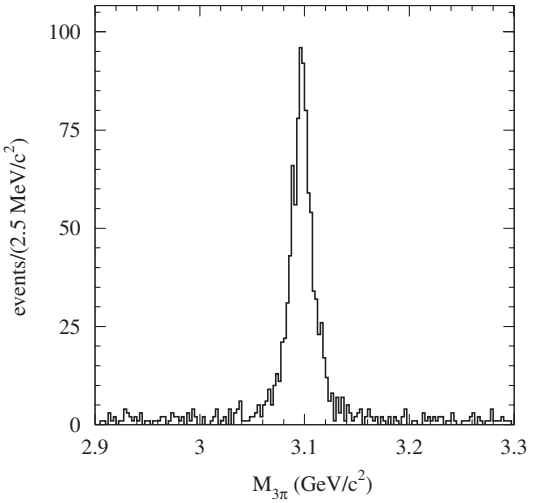


FIG. 75. The $3\pi$ mass spectrum for selected $e^+e^- \to \pi^+\pi^-\pi^0\gamma$ data events in the vicinity of the $J/\psi$ resonance. From Aubert *et al.*, 2004b.

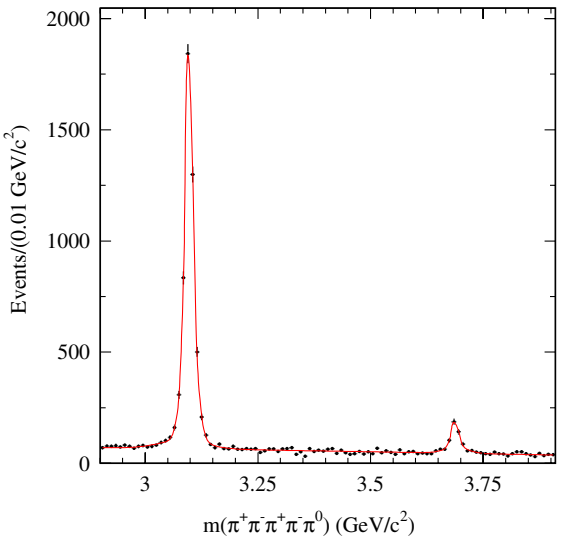


FIG. 76 (color online). The $2(\pi^+\pi^-)\pi^0$ mass distribution for ISR $e^+e^- \to 2(\pi^+\pi^-)\pi^0\gamma$ events in the $J/\psi$–$\psi(2S)$ mass region. From Aubert *et al.*, 2007c.

A part of events from the $\psi(2S)$ peak comes from the decay chain $\psi(2S) \to J/\psi\pi^+\pi^- \to 2(\pi^+\pi^-)\pi^0$ with the $J/\psi$ decaying to three pions. To select these events, the $\pi^+\pi^-\pi^0$ combination with the invariant mass closest to the $J/\psi$ mass is chosen. Figure 77(a) shows the scatter plot of this three-pion mass versus the five-pion mass. A clear signal from the above decay chain can be seen. The five-pion mass spectrum for events with the $\pi^+\pi^-\pi^0$ mass within the $\pm 0.05$ GeV/$c^2$ window around the $J/\psi$ mass is shown in Fig. 77(b). From the fit to the mass spectrum with a double-Gaussian function the number of detected $\psi(2S) \to J/\psi\pi^+\pi^- \to 2(\pi^+\pi^-)\pi^0$ events was determined to be $256 \pm 17$, and the triple product

$$\mathcal{B}(\psi(2S) \to J/\psi\pi^+\pi^-)\mathcal{B}(J/\psi \to \pi^+\pi^-\pi^0) \times \Gamma(\psi(2S) \to e^+e^-) = (1.86 \pm 0.12 \pm 0.11) \times 10^{-2} \text{ keV}$$

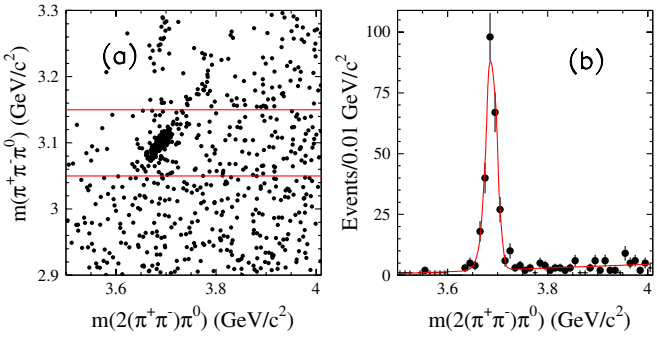


FIG. 77 (color online). (a) The three-pion combination closest to $J/\psi$ mass vs five-pion mass. (b) The five-pion mass for events with the three-pion mass in the $\pm 50$ MeV window around $J/\psi$ mass. From Aubert *et al.*, 2007c.

TABLE III. Measurements of the $J/\psi$ and $\psi(2S)$ branching fractions via ISR at *BABAR* (Aubert *et al.*, 2004b, 2005b, 2006a, 2006b, 2007c, 2007d) compared to the current world-average values (Nakamura *et al.*, 2010).

| Measured quantity | Measured value (eV) | $J/\psi$ or $\psi(2S)$ branching fraction ($10^{-3}$) *BABAR* | PDG-2010 |
|---|---|---|---|
| $\Gamma_{ee}^{J/\psi}\mathcal{B}_{J/\psi\to\pi^+\pi^-\pi^0}$ | $122 \pm 5 \pm 8$ | $21.8 \pm 1.0 \pm 1.6$ | $20.7 \pm 1.2 (S = 1.2)$[a] |
| $\Gamma_{ee}^{J/\psi}\mathcal{B}_{J/\psi\to 2(\pi^+\pi^-)}$ | $19.5 \pm 1.4 \pm 1.3$ | $3.70 \pm 0.26 \pm 0.37$ | $3.55 \pm 0.23$ |
| $\Gamma_{ee}^{J/\psi}\mathcal{B}_{J/\psi\to 2(\pi^+\pi^-)\pi^0}$ | $303 \pm 5 \pm 18$ | $54.6 \pm 0.9 \pm 3.4$ | $41 \pm 5 (S = 2.4)$ |
| $\Gamma_{ee}^{J/\psi}\mathcal{B}_{J/\psi\to 3(\pi^+\pi^-)}$ | $23.7 \pm 1.6 \pm 1.4$ | $4.40 \pm 0.29 \pm 0.29$ | $4.3 \pm 0.4$ |
| $\Gamma_{ee}^{J/\psi}\mathcal{B}_{J/\psi\to 2(\pi^+\pi^-\pi^0)}$ | $89 \pm 5 \pm 10$ | $16.5 \pm 1.0 \pm 1.8$ | $16.2 \pm 2.1$ |
| $\Gamma_{ee}^{J/\psi}\mathcal{B}_{J/\psi\to K^+K^-\pi^+\pi^-}$ | $37.9 \pm 0.8 \pm 1.1$ | $6.84 \pm 0.15 \pm 0.27$ | $6.6 \pm 0.5$ |
| $\Gamma_{ee}^{J/\psi}\mathcal{B}_{J/\psi\to K^+K^-\pi^0\pi^0}$ | $11.8 \pm 0.8 \pm 0.9$ | $2.12 \pm 0.15 \pm 0.18$ | $2.45 \pm 0.32$ |
| $\Gamma_{ee}^{J/\psi}\mathcal{B}_{J/\psi\to K^+K^-K^+K^-}$ | $4.00 \pm 0.33 \pm 0.29$ | $0.72 \pm 0.06 \pm 0.05$ | $0.76 \pm 0.09$ |
| $\Gamma_{ee}^{J/\psi}\mathcal{B}_{J/\psi\to K^+K^-\pi^+\pi^-\pi^0}$ | $107 \pm 4 \pm 6$ | $19.2 \pm 0.8 \pm 1.5$ | $17.9 \pm 2.9 (S = 2.2)$ |
| $\Gamma_{ee}^{J/\psi}\mathcal{B}_{J/\psi\to K^+K^-2(\pi^+\pi^-)}$ | $27.5 \pm 2.3 \pm 1.7$ | $5.09 \pm 0.42 \pm 0.35$ | $4.7 \pm 0.7 (S = 1.3)$ |
| $\Gamma_{ee}^{J/\psi}\mathcal{B}_{J/\psi\to\omega\pi^+\pi^-}\mathcal{B}_{\omega\to 3\pi}$ | $47.8 \pm 3.1 \pm 3.2$ | $9.7 \pm 0.6 \pm 0.6$ | $8.6 \pm 0.7 (S = 1.1)$ |
| $\Gamma_{ee}^{J/\psi}\mathcal{B}_{J/\psi\to\omega\pi^+\pi^-\pi^0}\mathcal{B}_{\omega\to 3\pi}$ | $22 \pm 3 \pm 2$ | $4.1 \pm 0.6 \pm 0.4$ | $4.0 \pm 0.7$ |
| $\Gamma_{ee}^{J/\psi}\mathcal{B}_{J/\psi\to\eta\pi^+\pi^-}\mathcal{B}_{\eta\to 3\pi}$ | $0.51 \pm 0.22 \pm 0.03$ | $0.40 \pm 0.17 \pm 0.03$ | $0.40 \pm 0.17$ |
| $\Gamma_{ee}^{J/\psi}\mathcal{B}_{J/\psi\to 2(\pi^+\pi^-)\eta}\mathcal{B}_{\eta\to\gamma\gamma}$ | $5.16 \pm 0.85 \pm 0.39$ | $2.35 \pm 0.39 \pm 0.20$ | $2.29 \pm 0.24$ |
| $\Gamma_{ee}^{J/\psi}\mathcal{B}_{J/\psi\to\phi\eta}\mathcal{B}_{\phi\to K^+K^-}\mathcal{B}_{\eta\to 3\pi}$ | $0.84 \pm 0.37 \pm 0.05$ | $1.4 \pm 0.6 \pm 0.1$ | $0.75 \pm 0.08 (S = 1.5)$ |
| $\Gamma_{ee}^{J/\psi}\mathcal{B}_{J/\psi\to K^+K^-\eta}\mathcal{B}_{\eta\to 2\gamma}$ | $4.8 \pm 0.7 \pm 0.3$ | $0.87 \pm 0.13 \pm 0.07$ | $0.87 \pm 0.15$ |
| $\Gamma_{ee}^{J/\psi}\mathcal{B}_{J/\psi\to\omega K^+K^-}\mathcal{B}_{\omega\to 3\pi}$ | $3.3 \pm 1.3 \pm 0.2$ | $1.36 \pm 0.50 \pm 0.10$ | $1.36 \pm 0.51$ |
| $\Gamma_{ee}^{J/\psi}\mathcal{B}_{J/\psi\to K^+K^-\pi^+\pi^-\eta}\mathcal{B}_{\eta\to\gamma\gamma}$ | $10.2 \pm 1.3 \pm 0.8$ | $4.7 \pm 0.6 \pm 0.4$ | $4.67 \pm 0.70$ |
| $\Gamma_{ee}^{J/\psi}\mathcal{B}_{J/\psi\to(K^{*0}\bar{K}_2^{*0}+\text{c.c.})}\mathcal{B}_{K^{*0}\to K\pi}\mathcal{B}_{K_2^{*0}\to K\pi}$ | $8.59 \pm 0.36 \pm 0.27$ | $6.98 \pm 0.29 \pm 0.21$ | $6.0 \pm 0.6$ |
| $\Gamma_{ee}^{J/\psi}\mathcal{B}_{J/\psi\to(K^0\bar{K}^*(892)^0+\text{c.c.})}$ | $26.6 \pm 2.5 \pm 1.5$ | $4.8 \pm 0.5 \pm 0.3$ | $4.39 \pm 0.31$ |
| $\Gamma_{ee}^{J/\psi}\mathcal{B}_{J/\psi\to(K^+\bar{K}^*(892)^-+\text{c.c.})}$ | $29.0 \pm 1.7 \pm 1.3$ | $5.2 \pm 0.3 \pm 0.2$ | $5.12 \pm 0.30$ |
| $\Gamma_{ee}^{J/\psi}\mathcal{B}_{J/\psi\to K^{*0}\bar{K}^{*0}}\mathcal{B}_{K^{*0}\to K^+\pi^-}\mathcal{B}_{\bar{K}^{*0}\to K^-\pi^+}$ | $0.57 \pm 0.15 \pm 0.03$ | $0.23 \pm 0.06 \pm 0.01$ | $0.23 \pm 0.07$ |
| $\Gamma_{ee}^{J/\psi}\mathcal{B}_{J/\psi\to\phi\pi^+\pi^-}\mathcal{B}_{\phi\to K^+K^-}$ | $2.19 \pm 0.23 \pm 0.07$ | $0.81 \pm 0.08 \pm 0.03$ | $0.94 \pm 0.09 (S = 1.2)$ |
| $\Gamma_{ee}^{J/\psi}\mathcal{B}_{J/\psi\to\phi\pi^0\pi^0}\mathcal{B}_{\phi\to K^+K^-}$ | $1.36 \pm 0.27 \pm 0.07$ | $0.50 \pm 0.10 \pm 0.03$ | $0.56 \pm 0.16$ |
| $\Gamma_{ee}^{J/\psi}\mathcal{B}_{J/\psi\to\phi K^+K^-}\mathcal{B}_{\phi\to K^+K^-}$ | $2.26 \pm 0.26 \pm 0.16$ | $1.67 \pm 0.19 \pm 0.12$[b] | $1.83 \pm 0.24$ |
| $\Gamma_{ee}^{J/\psi}\mathcal{B}_{J/\psi\to\phi f_0}\mathcal{B}_{\phi\to K^+K^-}\mathcal{B}_{f_0\to\pi^+\pi^-}$ | $0.69 \pm 0.11 \pm 0.05$ | $0.38 \pm 0.06 \pm 0.02$ | $0.32 \pm 0.09 (S = 1.9)$ |
| $\Gamma_{ee}^{J/\psi}\mathcal{B}_{J/\psi\to\phi f_0}\mathcal{B}_{\phi\to K^+K^-}\mathcal{B}_{f_0\to\pi^0\pi^0}$ | $0.48 \pm 0.12 \pm 0.05$ | $0.53 \pm 0.13 \pm 0.05$ | $0.32 \pm 0.09 (S = 1.9)$ |
| $\Gamma_{ee}^{J/\psi}\mathcal{B}_{J/\psi\to\phi 2(\pi^+\pi^-)}\mathcal{B}_{\phi\to K^+K^-}$ | $4.7 \pm 0.9 \pm 0.9$ | $1.77 \pm 0.35 \pm 0.12$ | $1.66 \pm 0.23$ |
| $\Gamma_{ee}^{\psi(2S)}\mathcal{B}_{\psi(2S)\to 2(\pi^+\pi^-)\pi^0}$ | $29.7 \pm 2.2 \pm 1.8$ | $12.0 \pm 0.9 \pm 0.7$ | $2.9 \pm 1.0 (S = 4.6)$ |
| $\Gamma_{ee}^{\psi(2S)}\mathcal{B}_{\psi(2S)\to 2(\pi^+\pi^-\pi^0)}$ | $11.2 \pm 3.3 \pm 1.3$ | $5.3 \pm 1.6 \pm 0.6$ | $5.3 \pm 1.7$ |
| $\Gamma_{ee}^{\psi(2S)}\mathcal{B}_{\psi(2S)\to K^+K^-2(\pi^+\pi^-)}$ | $4.4 \pm 2.1 \pm 0.3$ | $2.1 \pm 1.0 \pm 0.2$ | $1.9 \pm 0.9$ |
| $\Gamma_{ee}^{\psi(2S)}\mathcal{B}_{\psi(2S)\to J/\psi\pi^+\pi^-}\mathcal{B}_{J/\psi\to 3\pi}$ | $18.6 \pm 1.2 \pm 1.1$ | $23.6 \pm 1.6 \pm 1.6$ | $20.7 \pm 1.2 (S = 1.2)$[c] |
| $\Gamma_{ee}^{\psi(2S)}\mathcal{B}_{\psi(2S)\to\omega\pi^+\pi^-}\mathcal{B}_{\omega\to 3\pi}$ | $2.69 \pm 0.73 \pm 0.16$ | $1.22 \pm 0.33 \pm 0.07$ | $0.73 \pm 0.12$ |
| $\Gamma_{ee}^{\psi(2S)}\mathcal{B}_{\psi(2S)\to J/\psi\eta}\mathcal{B}_{\eta\to 3\pi}\mathcal{B}_{J/\psi\to\mu^+\mu^-}$ | $1.11 \pm 0.33 \pm 0.07$ | $33.4 \pm 9.9 \pm 2.0$ | $32.8 \pm 0.7$ |
| $\Gamma_{ee}^{\psi(2S)}\mathcal{B}_{\psi(2S)\to 2(\pi^+\pi^-)\eta}\mathcal{B}_{\eta\to\gamma\gamma}$ | $1.13 \pm 0.55 \pm 0.08$ | $1.2 \pm 0.6 \pm 0.1$ | $1.2 \pm 0.6$ |
| $\Gamma_{ee}^{\psi(2S)}\mathcal{B}_{\psi(2S)\to K^+K^-\pi^+\pi^-\pi^0}$ | $4.4 \pm 1.3 \pm 0.3$ | $1.8 \pm 0.5 \pm 0.1$ | $1.26 \pm 0.09 (S = 1.2)$ |
| $\Gamma_{ee}^{\psi(2S)}\mathcal{B}_{\psi(2S)\to K^+K^-\pi^+\pi^-\eta}\mathcal{B}_{\eta\to\gamma\gamma}$ | $1.2 \pm 0.7 \pm 0.1$ | $1.3 \pm 0.7 \pm 0.1$ | $1.3 \pm 0.7$ |
| $\Gamma_{ee}^{\psi(2S)}\mathcal{B}_{\psi(2S)\to K^+K^-\pi^+\pi^-}$ | $1.92 \pm 0.30 \pm 0.06$ | $0.81 \pm 0.13 \pm 0.03$ | $0.75 \pm 0.09 (S = 1.9)$ |
| $\Gamma_{ee}^{\psi(2S)}\mathcal{B}_{\psi(2S)\to K^+K^-\pi^0\pi^0}$ | $0.60 \pm 0.31 \pm 0.03$ | $0.25 \pm 0.13 \pm 0.02$ | $0.25 \pm 0.13$ |
| $\Gamma_{ee}^{\psi(2S)}\mathcal{B}_{\psi(2S)\to K^+K^-K^+K^-}$ | $0.22 \pm 0.10 \pm 0.02$ | $0.09 \pm 0.04 \pm 0.01$ | $0.060 \pm 0.014$ |
| $\Gamma_{ee}^{\psi(2S)}\mathcal{B}_{\psi(2S)\to\phi\pi^+\pi^-}\mathcal{B}_{\phi\to K^+K^-}$ | $0.27 \pm 0.09 \pm 0.02$ | $0.35 \pm 0.12 \pm 0.01$ | $0.117 \pm 0.029 (S = 1.7)$ |
| $\Gamma_{ee}^{\psi(2S)}\mathcal{B}_{\psi(2S)\to\phi f_0}\mathcal{B}_{\phi\to K^+K^-}\mathcal{B}_{f_0\to\pi^+\pi^-}$ | $0.17 \pm 0.06 \pm 0.02$ | $0.22 \pm 0.08 \pm 0.02$ | $0.068 \pm 0.024 (S = 1.1)$ |

[a] $S$ is a PDG scale factor.
[b] $\mathcal{B}_{J/\psi\to\phi K\bar{K}}$.
[c] $\mathcal{B}_{J/\psi\to 3\pi}$.

was obtained. By using the world-average $\Gamma(\psi(2S)\to e^+e^-)$ and $\mathcal{B}(\psi(2S)\to J/\psi\pi^+\pi^-)$ values (Amsler *et al.*, 2008), the branching fraction $\mathcal{B}(J/\psi\to\pi^+\pi^-\pi^0) = (2.36 \pm 0.16 \pm 0.16)\%$ was obtained, which is in good agreement with the *BABAR* measurement in the $3\pi$ final state $\mathcal{B}(J/\psi\to\pi^+\pi^-\pi^0) = (2.18 \pm 0.19)\%$ (Aubert *et al.*, 2004b). This, in particular, confirms the correctness of the normalization procedure used for the measurement of $\mathcal{B}(J/\psi\to 5\pi)$.

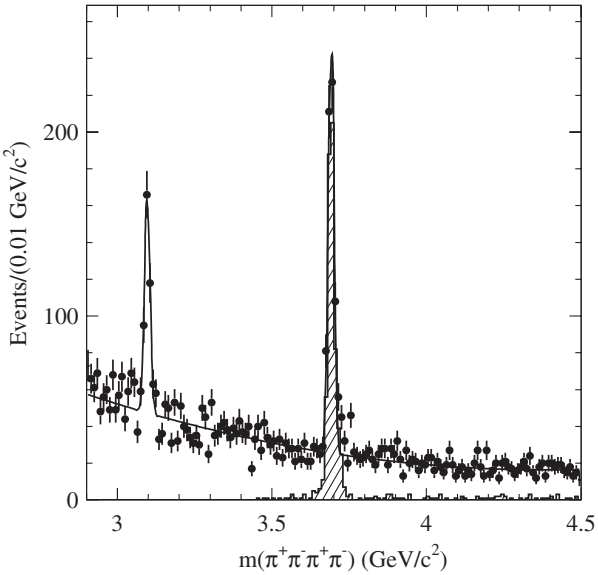


FIG. 78. The $2(\pi^+\pi^-)$ mass distribution for ISR-produced $e^+e^- \to 2(\pi^+\pi^-)$ events in the mass region around the $J/\psi$ and $\psi(2S)$; there are clear signals at the $J/\psi$ and $\psi(2S)$ mass positions. The latter is dominated by the $\psi(2S) \to J/\psi\pi^+\pi^- \to \mu^+\mu^-\pi^+\pi^-$ transition; selected events with two muons from the $J/\psi$ decays are shown by the shaded histogram. From Aubert *et al.*, 2005b.

Table III presents measurements of the $J/\psi$ and $\psi(2S)$ decay rates performed with the *BABAR* detector via ISR for many multihadron final states. The current PDG values are shown in the last column (Nakamura *et al.*, 2010). In most of the cases these values are close to those of *BABAR* emphasizing their importance. Note also that in a few cases the scale factor is significantly higher than 1 indicating a large difference between the *BABAR* measurement and previous results.

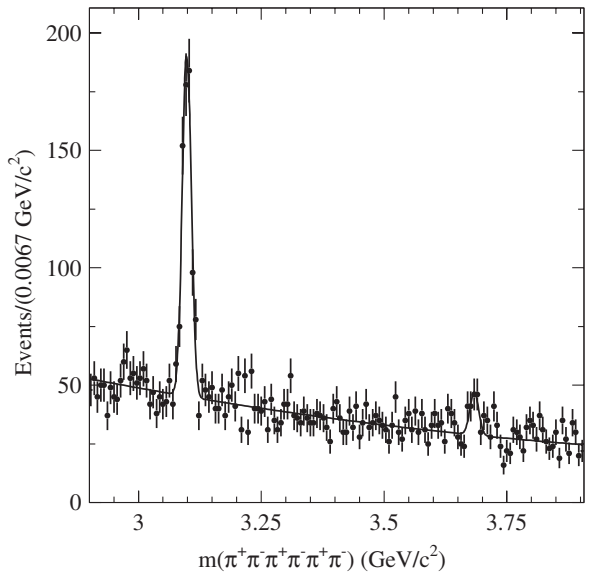


FIG. 79. The $3(\pi^+\pi^-)$ mass distribution for ISR-produced $e^+e^- \to 3(\pi^+\pi^-)$ events in the mass region around the $J/\psi$ and $\psi(2S)$; there are clear signals at the $J/\psi$ and $\psi(2S)$ mass positions. From Aubert *et al.*, 2006b.

TABLE IV. Ratios of the $J/\psi$ partial production rates to continuum cross sections $R_{J/\psi}$ [see Eq. (18)]. The result for $\mu^+\mu^-$ is from Aubert *et al.* (2004a). The result for $3(\pi^+\pi^-)$ is from Aubert *et al.* (2006b) and the results for $2(\pi^+\pi^-)$, $K^+K^-\pi^+\pi^-$, and $K^+K^-K^+K^-$ are from Aubert *et al.* (2005b).

| Final state | $R_{J/\psi}$ (MeV) |
|---|---|
| $2(\pi^+\pi^-)$ | $85.1 \pm 7.9$ |
| $3(\pi^+\pi^-)$ | $106 \pm 10$ |
| $2(\pi^+\pi^-\pi^0)$ | $99.1 \pm 6.5$ |
| $K^+K^-2(\pi^+\pi^-)$ | $122 \pm 10$ |
| $K^+K^-\pi^+\pi^-$ | $166 \pm 19$ |
| $K^+K^-K^+K^-$ | $138 \pm 32$ |
| $\mu^+\mu^-$ | $84.12 \pm 2.69$ |

As can be seen from Table III, the $J/\psi$ decay rates to even numbers of pions ($4\pi$, $6\pi$, etc.) are much smaller compared to the decays to odd numbers of pions. Indeed, a strong decay of the $J/\psi$ to an even number of pions is forbidden by $G$-parity conservation. It is expected that this decay is dominated by a single-photon transition $J/\psi \to \gamma^* \to n\pi$. No such suppression occurs for the strong $J/\psi$ decays to other modes, such as to three or five pions, which mainly proceed through three gluons. The $2(\pi^+\pi^-)$ and $3(\pi^+\pi^-)$ mass spectra for events of the ISR processes $e^+e^- \to 2(\pi^+\pi^-)\gamma$ and $e^+e^- \to 3(\pi^+\pi^-)\gamma$, in the mass regions of the $J/\psi$ and $\psi(2S)$ resonances, are shown in Figs. 78 and 79, respectively. From the fits to the mass spectra the numbers of $J/\psi$ and $\psi(2S)$ events and also the level of the nonresonant background are determined. The latter is proportional to the value of the nonresonant $e^+e^- \to 2(\pi^+\pi^-)$ or $e^+e^- \to 3(\pi^+\pi^-)$ cross section. In the *BABAR* paper (Aubert *et al.*, 2006b), the ratio

$$R_{J/\psi} = \frac{6\pi^2\Gamma(J/\psi \to e^+e^-)\mathcal{B}(J/\psi \to f)/m^2_{J/\psi}}{\sigma_{e^+e^-\to f}(m_{J/\psi})} \quad (18)$$

is calculated, where $\sigma_{e^+e^-\to f}$ is the value of the nonresonant cross section to the final state $f$ at the $J/\psi$ mass. The numerator of the ratio represents the integral over the $J/\psi$ excitation curve. The $R_{J/\psi}$ values for the $4\pi$, $6\pi$, $2K2\pi$, $2K4\pi$, and $4K$ final states are listed in Table IV together with the $R_{J/\psi}$ value obtained for the $\mu^+\mu^-$ final state. The $R_{J/\psi}$ values for the $4\pi$ and $6\pi$ final states are closer to that for $\mu^+\mu^-$ compared to the final states with kaons and indicate that the single-photon exchange dominates for the $J/\psi$ decays into these modes. For the $J/\psi$ decays to the final states with kaons, which can contain a sizable isoscalar component, the single-photon transition is expected to be less dominant, as indicated by the larger central values of the ratios.

## VI. ISR STUDIES IN THE CHARMONIUM REGION

In this section we discuss recent progress in the charmonium spectroscopy mainly achieved due to the application of the ISR method; see also recent reviews by Pakhlova, Pakhlov, and Eidelman (2010) and Brambilla *et al.* (2011). We start with a description of the open-charm final states addressing later so-called charmoniumlike states, presumably states with hidden charm.

### A. Final states with open charm

For a quarter of a century our knowledge of the vector charmonia above the threshold of open-charm production (throughout this section referred to as $\psi$ states) was based on the pioneer experiments of Mark-I (Siegrist *et al.*, 1976) and DASP (Brandelik *et al.*, 1978). Even such basic parameters of the $\psi$ mesons as mass, width, and leptonic width were known with large uncertainties mainly determined by low statistics of the old experiments. Seth (2005) made an attempt to use the updated information on the $R$ values from Crystal Ball (Osterheld *et al.*, 1986) and BES (Bai *et al.*, 2002) to improve these parameters. Finally, the BES Collaboration performed a global fit of the data on $R$ collected by BES in the energy range from 3.7 to 5 GeV (Ablikim *et al.*, 2008). In some cases the obtained values of mass, width, and leptonic width for the $\psi$ states differ significantly from the older values and still suffer from large uncertainties caused by insufficient statistics and model dependence primarily due to numerous thresholds of charm production opening in this energy region. It became clear that serious progress would be possible after tedious exclusive studies, which recently became possible due to ISR analyses of *BABAR* and Belle based on large integrated luminosities.

Exclusive $e^+e^-$ cross sections for hadronic final states containing charm mesons in the $\sqrt{s} = 3.7$–$5$ GeV$/c^2$ energy range were measured by *BABAR* (Aubert *et al.*, 2007e, 2009b) and Belle (Pakhlova *et al.*, 2007, 2008a, 2008b, 2008c, 2009) using ISR to reach the charmonium region. Note that in these analyses Belle systematically employed a partial reconstruction technique to increase the detection efficiency and suppress background.

The $D\bar{D}$ cross sections in the entire charm energy range from Belle (Pakhlova *et al.*, 2008a) and *BABAR* (Aubert *et al.*, 2007e) are shown in Figs. 80(a) and 80(b) and are consistent with each other. Both exhibit clear evidence of structures near 4.1 and 4.4 GeV$/c^2$. They also observe a structure [Figs. 80(a) and 80(b)] at 3900 MeV which must be taken into account to describe the $D\bar{D}$ cross section and $R$ in the region between the $\psi(3770)$ and $\psi(4040)$. This enhancement is not considered as a new $c\bar{c}$ resonance, as it is qualitatively consistent with the energy dependence of the sum of the cross sections for various channels opening in this energy range predicted in a coupled-channel model (Eichten *et al.*, 1980). The $D\bar{D}^*$ cross sections from Belle (Pakhlova *et al.*, 2007) and *BABAR* (Aubert *et al.*, 2009b) shown in Figs. 80(c) and 80(d) exhibit a single broad peak near threshold [close to the $\psi(4040)$ position], whereas the $D^*\bar{D}^*$ results from Belle (Pakhlova *et al.*, 2007) and *BABAR* (Aubert *et al.*, 2009b) [Figs. 80(e) and 80(f)] feature several local maxima and minima in this energy range.

*BABAR* (Aubert *et al.*, 2009b) performed unbinned maximum likelihood fits to the $D\bar{D}$, $D\bar{D}^*$, and $D^*\bar{D}^*$ spectra. The expected $\psi$ signals were parametrized by $p$-wave relativistic Breit-Wigner (RBW) functions with their parameters fixed to the PDG08 values (Amsler *et al.*, 2008). An interference between the resonances and the nonresonant contributions was required in the fit. The computed ratios of the branching fractions for the $\psi$ resonances and the quark model predictions are presented in Table V. The *BABAR* results deviate from some of the theoretical expectations, which often differ from each other.

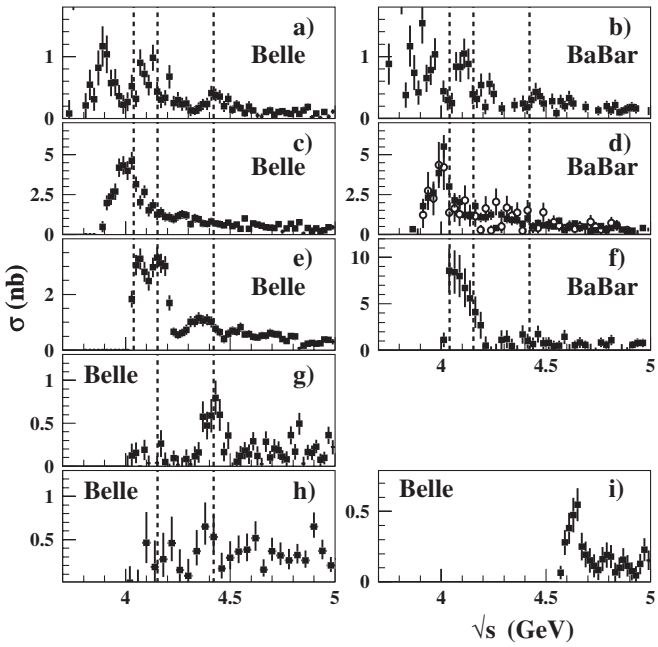


FIG. 80. Measured $e^+e^-$ exclusive open-charm cross sections for $\sqrt{s} = 3.7$–$5.0$ GeV$/c^2$ from Belle and *BABAR*, showing (a) $D\bar{D}$ (Pakhlova *et al.*, 2008a); (b) $D\bar{D}$ (Aubert *et al.*, 2007e); (c) $D^+D^{*-}$ (Pakhlova *et al.*, 2007); (d) $D\bar{D}^*$ for $D = D^0$ (solid squares) and $D = D^{\pm}$ (open circles) (Aubert *et al.*, 2009b); (e) $D^{*+}D^{*-}$ (Pakhlova *et al.*, 2007); (f) $D^*\bar{D}^*$ (Aubert *et al.*, 2009b); (g) $D^0D^-\pi^+$ (Pakhlova *et al.*, 2008b); (h) $D^0D^{*-}\pi^+$ (Pakhlova *et al.*, 2009); (i) $\Lambda_c\bar{\Lambda}_c$ (Pakhlova *et al.*, 2008c). Vertical dashed lines indicate $\psi$ masses in the region.

The $e^+e^- \to D^0D^-\pi^+$ cross section measured by Belle (Pakhlova *et al.*, 2008b) is shown in Fig. 80(g) and exhibits an unambiguous $\psi(4415)$ signal. A study of the resonant structure shows clear signals for the $\bar{D}_2^*(2460)^0$ and $D_2^*(2460)^+$ mesons and constructive interference between the neutral $D^0\bar{D}_2^*(2460)^0$ and the charged $D^-D_2^*(2460)^+$ decay amplitudes. Belle performed a likelihood fit to the $D^0D^-\pi^+$ mass distribution with a $\psi(4415)$ signal parametrized by an $S$-wave RBW function. The significance for the signal is $\sim 10\sigma$ and the peak mass and total width are in good agreement with the PDG06 (Yao *et al.*, 2006) values and the BES fit results (Ablikim *et al.*, 2008). The product

TABLE V. Ratios of branching fractions for the $\psi(4040)$, $\psi(4160)$, and $\psi(4415)$ resonances from *BABAR* (Aubert *et al.*, 2009b). Theoretical expectations are from models denoted $^3P_0$ (Barnes, Godfrey, and Swanson, 2005), $C^3$ (Eichten *et al.*, 2006), and $\rho K\rho$ (Swanson, 2006).

| State | Ratio | Measured | $^3P_0$ | $C^3$ | $\rho K\rho$ |
|---|---|---|---|---|---|
| $\psi(4040)$ | $D\bar{D}/D\bar{D}^*$ | $0.24 \pm 0.05 \pm 0.12$ | 0.003 | | 0.14 |
| | $D^*\bar{D}^*/D\bar{D}^*$ | $0.18 \pm 0.14 \pm 0.03$ | 1.0 | | 0.29 |
| $\psi(4160)$ | $D\bar{D}/D^*\bar{D}^*$ | $0.02 \pm 0.03 \pm 0.02$ | 0.46 | 0.08 | |
| | $D\bar{D}^*/D^*\bar{D}^*$ | $0.34 \pm 0.14 \pm 0.05$ | 0.011 | 0.16 | |
| $\psi(4415)$ | $D\bar{D}/D^*\bar{D}^*$ | $0.14 \pm 0.12 \pm 0.03$ | 0.025 | | |
| | $D\bar{D}^*/D^*\bar{D}^*$ | $0.17 \pm 0.25 \pm 0.03$ | 0.14 | | |

of the branching fractions $\mathcal{B}(\psi(4415) \to D\bar{D}_2^*(2460)) \times \mathcal{B}(\bar{D}_2^*(2460) \to D\pi^+)$ was found to be between 10% and 20% depending on the $\psi(4415)$ parametrization. The nonresonant $D^0D^-\pi^+$ branching fraction was found to be <22% of $\mathcal{B}(\psi(4415) \to D\bar{D}_2^*(2460) \to D^0D^-\pi^+)$. Similarly, the energy dependence of the cross section of the $D^0D^{*-}\pi^+$ final state, shown in Fig. 80(h), was measured by Belle (Pakhlova *et al.*, 2009); a marginal signal of the $\psi(4415)$ is found ($3.1\sigma$), and its branching fraction was limited to <10.6%. Recently *BABAR* (del Amo Sanchez *et al.*, 2010) and Belle (Pakhlova *et al.*, 2011) reported consistent results on the cross sections of $D_s^+D_s^-$, $D_s^+D_s^{*+}$ and $D_s^{*+}D_s^{*-}$.

The Belle Collaboration also measured the cross section of the process $e^+e^- \to \Lambda_c^+\Lambda_c^-$ (Pakhlova *et al.*, 2008c). Because of the large number of the $\Lambda_c$ decay channels with small branching fractions full reconstruction of both $\Lambda_c$ is not effective. The strategy of a search for $\Lambda_c^+\Lambda_c^-\gamma$ events at Belle (Pakhlova *et al.*, 2008c) was the following: One of the $\Lambda_c$ baryons was reconstructed using three decay modes $pK_S^0$, $pK^-\pi^+$, and $\Lambda\pi^+$. Then in the spectrum of masses recoiling against the $\Lambda_c^+\gamma$ system, a peak at the $\Lambda_c^-$ mass was searched for. This peak presumably corresponded to the process $e^+e^- \to \Lambda_c^+\Lambda_c^-\gamma$. The resulting exclusive cross section of the process $e^+e^- \to \Lambda_c^+\Lambda_c^-$ is shown in Fig. 80(i). The cross section is nearly flat from the threshold up to 5.4 GeV$/c^2$ except the region just above threshold, where a peak with the mass $M = 4634^{+10}_{-30}$ MeV$/c^2$, width $\Gamma = 92^{+40}_{-27}$ MeV$/c^2$, and significance of $8.2\sigma$ is observed. The state is denoted as $X(4630)$, and the product of the branching fractions measured for it is $\mathcal{B}(e^+e^-) \times \mathcal{B}(\Lambda_c\bar{\Lambda}_c) = (0.68 \pm 0.33) \times 10^{-6}$. The nature of this enhancement remains unclear. Although both mass and width of the $X(4630)$ are consistent within errors with those of another Belle state $Y(4660)$, that was found in $\psi(2S)\pi\pi$ decays via ISR and is described in the next section (Wang *et al.*, 2007), this could be coincidence and does not exclude other interpretations.

Although in general the energy behavior of the exclusive cross sections from *BABAR* and Belle qualitatively follows the expectations of the coupled-channel model (Eichten *et al.*, 1980), some features are not reproduced by theory. This is confirmed by the measurement of CLEO (Cronin-Hennessy *et al.*, 2009), which scanned the energy range between 3.97 and 4.26 GeV and reported the cross sections for final states consisting of two charm mesons ($D\bar{D}$, $D^*\bar{D}$, $D^*\bar{D}^*$, $D_s^+D_s^-$, $D_s^{*+}D_s^-$ and $D_s^{*+}D_s^{*-}$) as well as for those in which the charm-meson pair is accompanied by a pion. The updated potential model predictions of Eichten *et al.* (1980, 2006) fail to describe many features of the data.

### B. New charmoniumlike states

The first observation of an unexpected vector charmoniumlike state was made by *BABAR* (Aubert *et al.*, 2005a) in ISR production of $Y(4260) \to J/\psi\pi^+\pi^-$, which was later updated (Aubert *et al.*, 2008a) with twice the data, as shown in Fig. 81. CLEO (He *et al.*, 2006) and Belle (Yuan *et al.*, 2007) confirmed the *BABAR* result, but Belle also found a smaller, broader structure at 4008 MeV$/c^2$, as seen in Fig. 82. Aside from the lower mass state, for which the updated *BABAR* (Aubert *et al.*, 2008a) analysis placed an upper limit, the

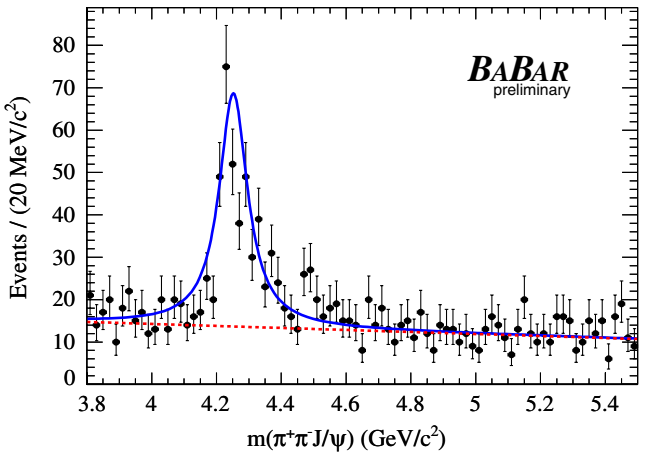


FIG. 81 (color online). The invariant mass of $J/\psi\pi^+\pi^-$ candidates produced in initial state radiation, $e^+e^- \to \gamma_{\rm ISR}J/\psi\pi^+\pi^-$. Points with error bars represent data, and the curves show the fit (solid line) to a signal plus a linear background (dashed line). From Aubert *et al.*, 2008a.

three sets of measurements were quite consistent in mass and width, as shown in Table VI, but only roughly so in strength. *BABAR* (Aubert *et al.*, 2007a) found one more apparent enhancement $Y(4360)$ in $\psi(2S)\pi^+\pi^-$, which Belle (Wang *et al.*, 2007) measured with somewhat larger mass and smaller width, as seen in Table VII. Belle also found a second structure near 4660 MeV$/c^2$ in the same final state, as seen in Fig. 83. [A combined fit (Liu, Qin, and Yuan, 2008) to Belle and *BABAR* $\psi(2S)\pi^+\pi^-$ data found consistency between them.] Because dipion transitions between vector quarkonia are commonplace for charmonium and bottomonium, it was natural to ascribe the $Y$'s to excited vector charmonia. A number of additional features of these states are in conflict with this hypothesis. Only one, $Y(4660)$, is remotely near a

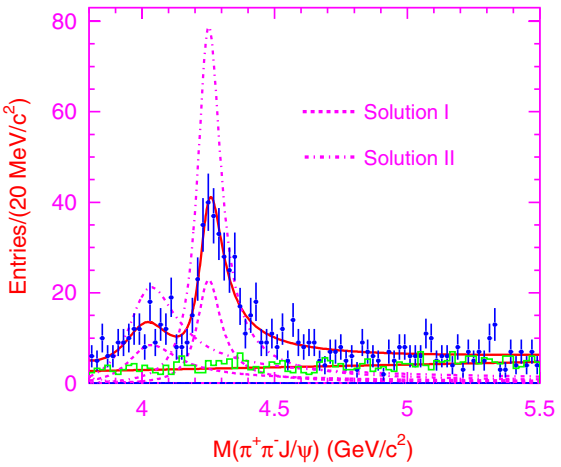


FIG. 82 (color online). The invariant mass of $J/\psi\ \pi^+\pi^-$ candidates produced in initial state radiation studied by Belle (Yuan *et al.*, 2007), with $J/\psi$ sidebands already subtracted, unlike Fig. 81. Points with error bars represent data, the solid curve shows the best fits to the data to two resonances including interference with a floating phase, and the dashed and dash-dotted curves show the two pairs of individual resonance contributions for the two equally probable best-fit phases.

TABLE VI. Measured properties of the $Y(4260) \to J/\psi\ \pi^+\pi^-$. The Belle (Wang *et al.*, 2007) single-resonance fit result is quoted to allow for comparison to the other two.

| Quantity | Value | From ($\chi^2$/ndf) |
|---|---|---|
| $M$ (MeV/$c^2$) | $4259 \pm 8^{+2}_{-6}$ | *BABAR* (Aubert *et al.*, 2008a) |
| | $4263 \pm 6$ | Belle (Yuan *et al.*, 2007) |
| | $4284^{+17}_{-16} \pm 4$ | CLEO (He *et al.*, 2006) |
| | $4263 \pm 5$ | Avg(1.8/2) |
| $\Gamma$ (MeV) | $88 \pm 23^{+6}_{-4}$ | *BABAR* (Aubert *et al.*, 2008a) |
| | $126 \pm 18$ | Belle (Yuan *et al.*, 2007) |
| | $73^{+39}_{-25} \pm 5$ | CLEO (He *et al.*, 2006) |
| | $108 \pm 15$ | Avg(2.4/2) |
| $\mathcal{B} \times \Gamma_{ee}$ (eV) | $5.5 \pm 1.0^{+0.8}_{-0.7}$ | *BABAR* (Aubert *et al.*, 2008a) |
| | $9.7 \pm 1.1$ | Belle (Yuan *et al.*, 2007) |
| | $8.9^{+3.9}_{-3.1} \pm 1.8$ | CLEO (He *et al.*, 2006) |
| | $8.0 \pm 1.4$ | Avg(6.1/2) |

predicted $1^{--}$ $c\bar{c}$ state ($1^3D_1$). The $Y(4260)$ and $Y(4360)$ did not show up in inclusive hadronic cross section ($R$) measurements (Bai *et al.*, 2002), as would be expected of such states [there is no fine-grained $R$-scan data near $Y(4660)$].

A comparison of the measured $J/\psi\pi^+\pi^-$ and total hadronic cross sections in the $\sqrt{s} \simeq 4260$ MeV region yields a lower bound for $\Gamma(Y \to J/\psi\pi^+\pi^-) > 508$ keV at 90% C.L., an order of magnitude higher than expectations for conventional vector charmonium states (Mo *et al.*, 2006). Charmonium would also feature dominant open-charm decays, exceeding those of dipion transitions by a factor expected to be $\gtrsim 100$, because such is the case for $\psi(3770)$ and $\psi(4160)$. As summarized in Table VIII, no such evidence has been found, significantly narrowing any window for either charmonia or, in some cases, quark-gluon hybrid interpretations. CLEO (Coan *et al.*, 2006) studied direct production of the $Y(4260)$ in $e^+e^-$ collisions and identified the only non-$J/\psi\pi^+\pi^-$ decay modes seen thus far, $J/\psi\pi^0\pi^0$ and $J/\psi K^+K^-$, occurring at roughly one-half and one-sixth, respectively, of the $J/\psi\pi^+\pi^-$ rate. The $J/\psi K^+K^-$ decay mode was also observed by Belle (Yuan *et al.*, 2008).

Any interpretation for these vector states will not only have to explain their masses, widths, and manifest reluctance to materialize in open charm or unflavored light meson final states. The dipion invariant-mass spectra exhibit curious structures, as seen for the $Y(4260)$ in Fig. 84 (Aubert *et al.*, 2008a), for the $Y(4360)$ in Fig. 85(a) (Wang *et al.*, 2007), and for the $Y(4660)$ in Fig. 85(b) (Wang *et al.*, 2007). The first shows a distinctly non-phase-space double-hump structure which is qualitatively confirmed by Belle (Yuan *et al.*, 2007), the second exhibits a majority of events at higher masses, and the third indicates a quite dominant $f_0(980)$ component.

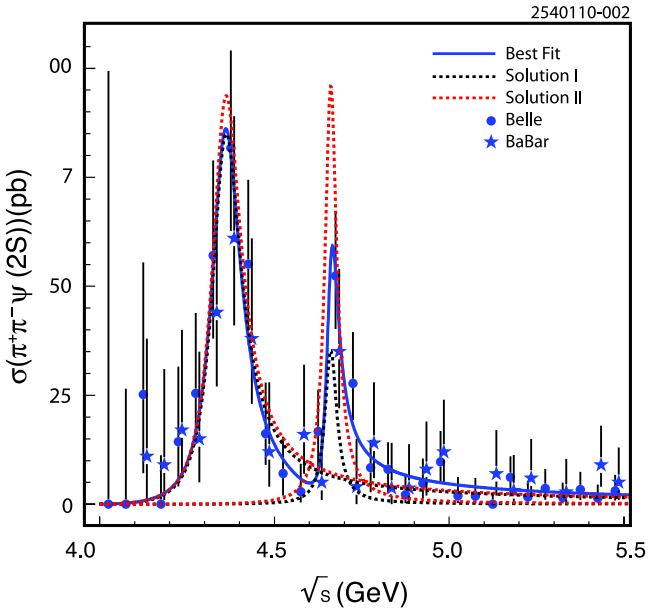


FIG. 83 (color online). From a binned maximum likelihood fit of combined Belle and *BABAR* data, the $\psi(2S)\pi^+\pi^-$ invariant-mass cross section as a function of $\sqrt{s}$. The solid circles and stars show the Belle and *BABAR* data, respectively. The solid curve shows the best fits to the data to two resonances including interference with a floating phase, and the dashed curves show the contributions of two pairs of individual resonances for the two equally probable best-fit phases. From Liu, Qin, and Yuan, 2008.

TABLE VII. Measured properties of the two enhancements found in the $\psi(2S)\pi^+\pi^-$ mass distribution, the $Y(4360)$ and $Y(4660)$. Liu, Qin, and Yuan (2008) performed a binned maximum likelihood fit to the combined Belle and *BABAR* cross section distributions (see Fig. 83).

| Quantity | Value | From ($\chi^2$/dof) |
|---|---|---|
| $M$ (MeV/$c^2$) | $4324 \pm 24$ | *BABAR* (Aubert *et al.*, 2007a) |
| | $4361 \pm 9 \pm 9$ | Belle (Wang *et al.*, 2007) |
| | $4353 \pm 15$ | Avg(1.8/1) |
| | $4355^{+9}_{-10} \pm 9$ | Liu (Liu, Qin, and Yuan, 2008) |
| $\Gamma$ (MeV) | $172 \pm 33$ | *BABAR* (Aubert *et al.*, 2007a) |
| | $74 \pm 15 \pm 10$ | Belle (Wang *et al.*, 2007) |
| | $96 \pm 42$ | Avg(6.8/1) |
| | $103^{+17}_{-15} \pm 11$ | Liu (Liu, Qin, and Yuan, 2008) |
| $M$ (MeV/$c^2$) | $4664 \pm 11 \pm 5$ | Belle (Wang *et al.*, 2007) |
| | $4661^{+9}_{-8} \pm 6$ | Liu (Liu, Qin, and Yuan, 2008) |
| $\Gamma$ (MeV) | $48 \pm 15 \pm 3$ | Belle (Wang *et al.*, 2007) |
| | $42^{+17}_{-12} \pm 6$ | Liu (Liu, Qin, and Yuan, 2008) |

TABLE VIII. Upper limits at 90% C.L. on the ratios $\sigma(e^+e^- \to Y \to T)/\sigma(e^+e^- \to Y \to J/\psi\pi^+\pi^-)$ at $\sqrt{s} = 4.26$ GeV/$c^2$ [CLEO (Cronin-Hennessy *et al.*, 2009)] and $\mathcal{B}(Y \to T)/\mathcal{B}(Y \to J/\psi\pi^+\pi^-)$ [for $Y(4260)$] [*BABAR* (Aubert *et al.*, 2007e, 2009b) and Belle (Pakhlova *et al.*, 2007)], where $T$ is an open-charm final state.

| $T$ | $Y(4260)$ |
|---|---|
| $D\bar{D}$ | 4.0 (Cronin-Hennessy *et al.*, 2009) |
| | 7.6 (Aubert *et al.*, 2007e) |
| $D\bar{D}^*$ | 45 (Cronin-Hennessy *et al.*, 2009) |
| | 34 (Aubert *et al.*, 2009b) |
| $D^*\bar{D}^*$ | 11 (Cronin-Hennessy *et al.*, 2009) |
| | 40 (Aubert *et al.*, 2009b) |
| $D\bar{D}^*\pi$ | 15 (Cronin-Hennessy *et al.*, 2009) |
| | 9 (Pakhlova *et al.*, 2007) |
| $D^*\bar{D}^*\pi$ | 8.2 (Cronin-Hennessy *et al.*, 2009) |
| $D_s\bar{D}_s$ | 1.3 (Cronin-Hennessy *et al.*, 2009) |
| $D_s\bar{D}_s^*$ | 0.8 (Cronin-Hennessy *et al.*, 2009) |
| $D_s^*\bar{D}_s^*$ | 9.5 (Cronin-Hennessy *et al.*, 2009) |

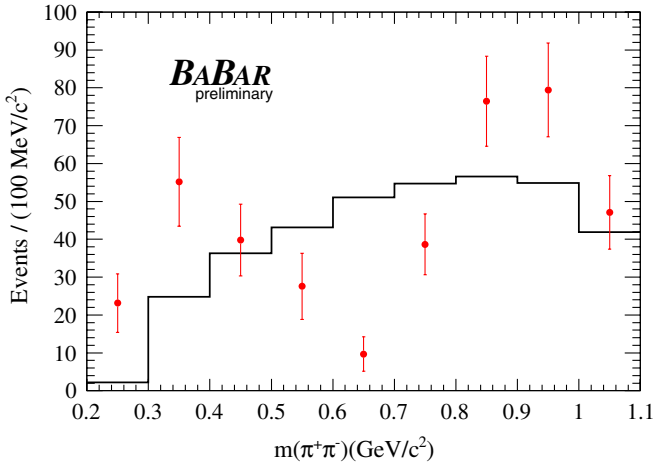


FIG. 84 (color online). The dipion invariant-mass distribution on ISR-produced $Y(4260) \to J/\psi\pi^+\pi^-$ decays, where points represent data and the line histogram represents phase-space MC simulation. From Aubert *et al.*, 2008a.

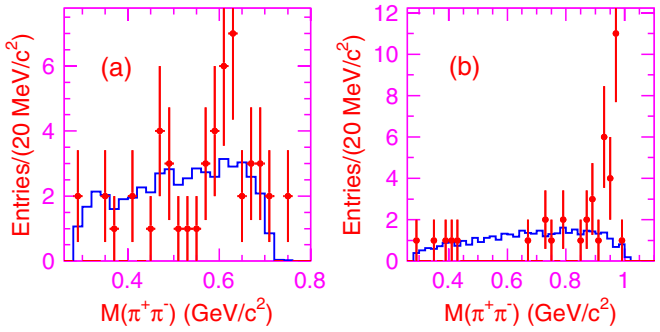


FIG. 85 (color online). The dipion invariant-mass distribution on ISR-produced (a) $Y(4360) \to \psi(2S)\pi^+\pi^-$ and (b) $Y(4660) \to \psi(2S)\pi^+\pi^-$, where points represent data and the line histogram represents phase-space MC simulation. From Wang *et al.*, 2007.

## VII. SOME IMPLICATIONS FOR THEORY AND PERSPECTIVES

The progress in precision of the low-energy data on $e^+e^- \to$ hadrons achieved recently due to ISR studies allows an update of the estimation of the hadronic contribution to the muon anomalous magnetic moment to be performed. It is well known that the precision of the standard model prediction of this quantity is limited by the contributions from strong interactions. These are conventionally separated into a theory-driven light-by-light contribution; see a recent review by Prades, de Rafael, and Vainshtein (2009), and two experiment-driven vacuum polarization contributions, the dominant lowest-order and higher-order parts. The lowest-order term can be calculated from a dispersion integral (Bouchiat and Michel, 1961; Gourdin and de Rafael, 1969) in which the integrand contains a combination of experimental data on cross sections of $e^+e^- \to$ hadrons and perturbative QCD. The integral ranges from the threshold of hadron production, i.e., from the $\pi^0\gamma$ threshold to infinity:

$$a_\mu^{\mathrm{had,LO}} = \left(\frac{\alpha m_\mu}{3\pi}\right)^2 \int_{m_\pi^2}^{\infty} ds \frac{R(s)\hat{K}(s)}{s^2}. \tag{19}$$

The function $\hat{K}(s)$ in the integration kernel is rather smooth, whereas the factor $1/s^2$ emphasizes the low-energy part of the spectrum. Of particular importance is the process $e^+e^- \to \pi^+\pi^-(\gamma)$, which provides about 73% of the lowest-order hadronic contribution and about 62% of its total quadratic error.

In most cases new ISR results from *BABAR* are consistent with previous measurements and have comparable or better accuracy. However, not always do these results agree with the corresponding old data sets. For example, from Fig. 23 discussed in Sec. III it is clear that the cross section of the process $e^+e^- \to \pi^+\pi^-\pi^0$ obtained by *BABAR* (Aubert *et al.*, 2004b) is consistent with that of SND (Achasov *et al.*, 2002) below $\sqrt{s} = 1.4$ GeV, but is much higher than that at DM2 (Antonelli *et al.*, 1992) above this energy. The energy dependence of the cross section observed by DM2 is also inconsistent with other measurements [see the discussion of this problem by Achasov *et al.* (2002)] and the existence of the rather well-established $\omega(1420)$ and $\omega(1650)$ resonances. The contribution of this process to $a_\mu^{\mathrm{had,LO}}$, which was equal to $(2.45 \pm 0.26) \times 10^{-10}$ before *BABAR* (Davier *et al.*, 2003b), becomes $(3.25 \pm 0.09) \times 10^{-10}$ after the new results are taken into account (Davier, 2007). For the process $e^+e^- \to 2\pi^+2\pi^-$, in which the cross section is one of the largest above 1 GeV, the new *BABAR* measurement (Aubert *et al.*, 2005b) is in good agreement with the older results and after taking them into account the precision of the corresponding contribution improves by a factor of 2. Another example is the measurement of two six-pion final states (Aubert *et al.*, 2006b). In Figs. 86 and 87 we compare the cross sections from *BABAR* with those in older measurements. It is clear that the improvement is dramatic because older measurements were too imprecise to make a reasonable prediction. We summarized the discussed contributions to $a_\mu^{\mathrm{had,LO}}$ integrated from threshold to 1.8 GeV for the measurements before *BABAR* [see the references in Davier *et al.* (2003b)] and with *BABAR* in Table IX (Davier, 2007).

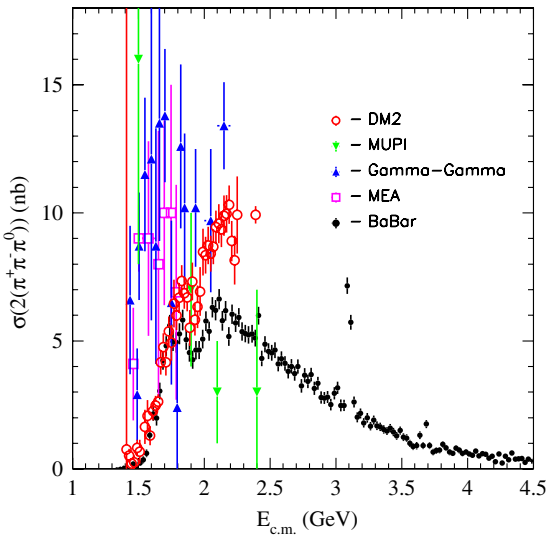


FIG. 86 (color online). The cross section of the process $e^+e^- \to 2\pi^+2\pi^-2\pi^0$ (Cosme *et al.*, 1979; Bacci *et al.*, 1981; Esposito *et al.*, 1981; Castro, 1988; Aubert *et al.*, 2006b).

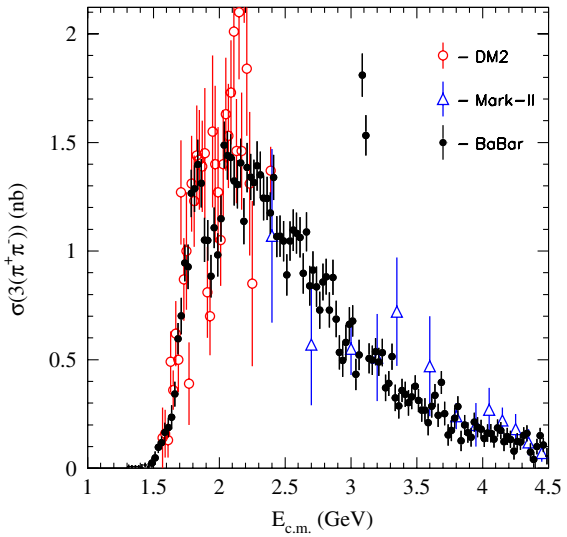


FIG. 87 (color online). The cross section of the process $e^+e^- \to 3\pi^+3\pi^-$ (Jean-Marie *et al.*, 1976; Castro, 1988; Aubert *et al.*, 2006b).

The calculation using all multibody modes measured by *BABAR* (Aubert *et al.*, 2004b, 2005b, 2006b, 2007c) together with the relevant older measurements [for a complete list of references, see Davier *et al.* (2003b)] gives for the contribution of hadronic continuum from threshold to 1.8 GeV the value $(54.2 \pm 1.9) \times 10^{-10}$. It is consistent with the result of the older calculation (Davier *et al.*, 2003b) $(55.0 \pm 2.6) \times 10^{-10}$, and more precise.

An important step in the calculations of $a_\mu^{\mathrm{had,LO}}$ has been made recently by Davier *et al.* (2010a), which for the first time took into account the *BABAR* measurement of the reaction $e^+e^- \to \pi^+\pi^-$ (Aubert *et al.*, 2009a) and finally by Davier *et al.* (2011), which also accounted for the KLOE results on the $\pi^+\pi^-$ final state (Ambrosino *et al.*, 2009, 2011). It uses the whole set of experimental data in the energy range up to 1.8 GeV, the region dominated by hadronic resonances, and perturbative QCD for the contribution of the quark continuum beyond that energy. In particular, they modify the treatment of the $\omega(782)$ and $\phi(1020)$ resonances using the data from Aubert *et al.* (2004b) and include preliminary data of *BABAR* on $e^+e^- \to \pi^+\pi^-2\pi^0$ (Druzhinin, 2007). They also use isospin invariance to estimate the contributions from several unmeasured final states with six pions and $K\bar{K}(n\pi)$ relating them to those of known channels. For other channels they refer to earlier calculations (Davier *et al.*, 2003a, 2003b, 2007).

TABLE IX. The contribution of some multipion processes to $a_\mu^{\mathrm{had,LO}}$ integrated from threshold to 1.8 GeV for the measurements before *BABAR* and including the new *BABAR* results. For the $\pi^+\pi^-\pi^0$ final state the contribution of the $\omega$ and $\phi$ mesons is excluded. All values are in units of $10^{-10}$.

| Process | Before *BABAR* | With *BABAR* |
|---|---|---|
| $\pi^+\pi^-\pi^0$ | $2.45 \pm 0.26$ | $3.25 \pm 0.09$ |
| $2\pi^+2\pi^-$ | $14.20 \pm 0.90$ | $13.09 \pm 0.44$ |
| $3\pi^+3\pi^-$ | $0.10 \pm 0.10$ | $0.11 \pm 0.02$ |
| $2\pi^+2\pi^-2\pi^0$ | $1.42 \pm 0.30$ | $0.89 \pm 0.09$ |

TABLE X. Estimated $a_\mu^{\mathrm{had,LO}}[\pi\pi]$ and $\mathcal{B}_{\mathrm{CVC}}$ contributions from the $e^+e^-$ data (Davier *et al.*, 2011).

| Experiment | $a_\mu^{\mathrm{had,LO}}[\pi\pi]$ $(10^{-10})$ | $\mathcal{B}_{\mathrm{CVC}}$ (%) |
|---|---|---|
| *BABAR* | $514.1 \pm 3.8$ (1.00) | $25.15 \pm 0.18 \pm 0.22$ (1.00) |
| KLOE | $503.1 \pm 7.1$ (0.97) | $24.56 \pm 0.26 \pm 0.22$ (0.92) |
| CMD2 | $506.6 \pm 3.9$ (0.89) | $24.96 \pm 0.21 \pm 0.22$ (0.96) |
| SND | $505.1 \pm 6.7$ (0.94) | $24.82 \pm 0.30 \pm 0.22$ (0.91) |

Contributions to $a_\mu^{\mathrm{had,LO}}[\pi\pi]$ from the individual $\pi^+\pi^-$ cross sections measured at *BABAR* (Aubert *et al.*, 2009a), KLOE (Ambrosino *et al.*, 2009, 2011), CMD2 (Akhmetshin *et al.*, 2004a, 2007), and SND (Achasov *et al.*, 2006) are given in the middle column of Table X (Davier *et al.*, 2011). In the right column we list the corresponding CVC predictions for the $\tau^\pm \to \pi^\pm\pi^0\nu_\tau$ branching fraction corrected for isospin-breaking effects (Davier *et al.*, 2010b). Here the first error is experimental and the second estimates the uncertainty in the isospin-breaking corrections. For each experiment, all available data in the energy range from threshold to 1.8 GeV ($m_\tau$ for $\mathcal{B}_{\mathrm{CVC}}$) are used, and the missing part is completed by the combined $e^+e^-$ data.

The average of the four separate results gives $a_\mu^{\mathrm{had,LO}}[\pi\pi] = (507.8 \pm 2.8_{\mathrm{tot}}) \times 10^{-10}$ (Davier *et al.*, 2011). Comparison with their previous result (Davier *et al.*, 2010b) $a_\mu^{\mathrm{had,LO}}[\pi\pi] = (503.5 \pm 3.5_{\mathrm{tot}}) \times 10^{-10}$ shows that the inclusion of the new *BABAR* data significantly increases the central value of the integral. For higher-order hadronic contributions to $a_\mu^{\mathrm{had,LO}}$, which are also estimated based on $e^+e^-$ data, there is a slight gain in accuracy from $-9.79 \pm 0.08_{\mathrm{exp}} \pm 0.03_{\mathrm{rad}}$ (Hagiwara *et al.*, 2007) to $-9.79 \pm 0.06_{\mathrm{exp}} \pm 0.03_{\mathrm{rad}}$ (Hagiwara *et al.*, 2011).

A compilation of recent results for $a_\mu$, from which the central value of the experimental average (Bennett *et al.*, 2006) has been subtracted, is given in Fig. 88. The shaded vertical band indicates the experimental error. The SM

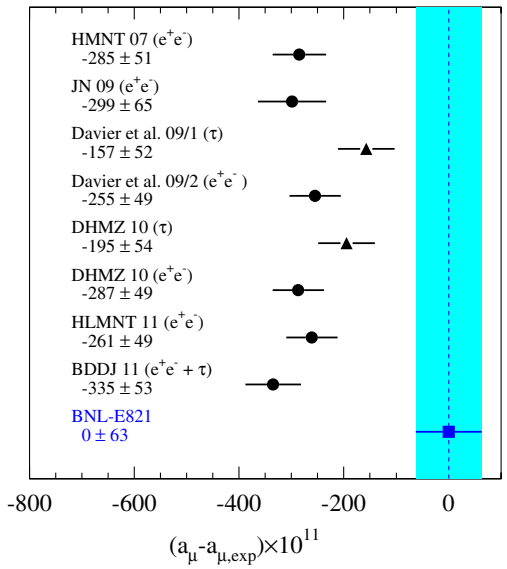


FIG. 88 (color online). Compilation of recent results for $a_\mu$.

predictions are taken from HMNT 07 (Hagiwara *et al.*, 2007), JN 09 (Jegerlehner and Nyffeler, 2009), Davier *et al.* 09/1 ($\tau$ based) (Davier *et al.*, 2010b), Davier *et al.* 09/2 ($e^+e^-$ based, with *BABAR* $\pi^+\pi-$ data) (Davier *et al.*, 2010a), HLMNT 11 ($e^+e^-$ based, with *BABAR* and KLOE $\pi^+\pi^-$ data) (Hagiwara *et al.*, 2011), DHMZ 10 ($\tau$ and $e^+e^-$) (Davier *et al.*, 2011), BDDJ 11 ($\tau$ and $e^+e^-$) (Benayoun *et al.*, 2011).

There have been only a few tests of CVC based on the new data. The most interesting final state is, of course, that with two pions, where a serious discrepancy between the $e^+e^-$ and $\tau$ data was reported (Davier *et al.*, 2003a, 2003b). The results of the most recent tests in this channel (Davier *et al.*, 2010b, 2011) are based on the reevaluation of isospin-breaking corrections. The predictions for the branching fraction of $\tau^\pm \to \pi^\pm\pi^0\nu_\tau$ shown in Table X can be compared to the world-average value of $(25.51 \pm 0.09)\%$ (Nakamura *et al.*, 2010). Although the difference between the CVC prediction and the experimental value is less significant than previously thought (Davier *et al.*, 2003b; Davier, 2007), it is still substantial for all groups but *BABAR*. A new approach to the problem was suggested recently by Jegerlehner and Szafron (2011), where the $\rho$-$\gamma$ mixing was properly taken into account. The CVC prediction for the branching fraction to two pions is $(25.20 \pm 0.17 \pm 0.28)\%$ in good agreement with the direct measurement. Finally, Benayoun *et al.* (2011) reported consistent results on $e^+e^-$ and $\tau$ in the $2\pi$ channel and obtained a theoretical prediction for $a_\mu$, which is lower than the experimental value by $4.1\sigma$.

One more test of CVC that included recent ISR results from *BABAR* was performed by Cherepanov and Eidelman (2009). They used CVC together with the data on $e^+e^- \to \eta\pi^+\pi^-$ and $e^+e^- \to \eta'\pi^+\pi^-$ to estimate the branching fraction of the corresponding $\tau$ decays. For the former final state the estimate based on the older data (Delcourt *et al.*, 1982; Druzhinin *et al.*, 1986; Antonelli *et al.*, 1988; Akhmetshin *et al.*, 2000) predicted for the branching fraction $(0.132 \pm 0.016)\%$, somewhat smaller but not incompatible with $(0.165 \pm 0.015)\%$ obtained from the *BABAR* data (Aubert *et al.*, 2007c). The average of the two gives the CVC prediction of $(0.150 \pm 0.016)\%$, in good agreement with the new world average $\mathcal{B}(\tau^- \to \eta\pi^-\pi^0\nu_\tau) = (0.139 \pm 0.010)\%$ that uses the new precise measurement at Belle (Inami *et al.*, 2009). For the $\mathcal{B}(\tau^- \to \eta'\pi^-\pi^0\nu_\tau)$ they give an upper limit of $<3.2 \times 10^{-5}$ at 90% C.L., which is a factor of 2.5 more restrictive than the upper limit based on the only existing measurement by CLEO: $<8 \times 10^{-5}$ (Bergfeld *et al.*, 1997).

There are two recent evaluations of $\Delta\alpha^{(5)}_{\rm had}(M_Z^2)$, the hadronic contribution to the running $\alpha$ from five flavors (Davier *et al.*, 2011; Hagiwara *et al.*, 2011). Hagiwara *et al.* (2011) included a data set of $e^+e^-$ cross sections, multibody data from *BABAR* and $2\pi$ data from KLOE and the calculation gives the value $0.027\,60 \pm 0.000\,15$, slightly higher and significantly more accurate than the previously accepted value $0.027\,58 \pm 0.000\,35$ (Burkhardt and Pietrzyk, 2005). The estimation performed by Davier *et al.* (2011) additionally used the *BABAR* data on the $\pi\pi$ final state and perturbative QCD between 1.8 and 3.7 GeV and gave an even more precise value $0.027\,49 \pm 0.000\,10$.

## VIII. CONCLUSIONS

Successful experiments at high-luminosity $e^+e^-$ colliders ($\phi$ and $B$ factories) opened a new era in a study of $e^+e^-$ annihilation into hadrons at low energies using a novel method of initial state radiation usually referred to as ISR or radiative return.

Modern detectors operating at these factories which collected unprecedented high integrated luminosity allow this method to compete with direct $e^+e^-$ experiments.

A lot of new data on the cross sections of $e^+e^-$ annihilation into hadrons were obtained using ISR on the production of mesons from threshold of their production $\sim 2m_\pi$ to the c.m. energy of about 4–5 GeV. More than 30 processes have been studied in which mesons and hadronic resonances were produced, many of them for the first time.

Valuable information on the particles with mass of about a few GeV has been obtained, primarily on excited vector mesons, radial, and/or orbital excitations. Parameters of vector charmonia were investigated, and new data on more than 40 decay channels were obtained. Many decays were observed for the first time.

New data on production cross sections were obtained for various baryons: proton, $\Lambda$, $\Sigma^0$, and $\Lambda_c$ hyperon, opening new possibilities for testing form factor models.

New states [$\rho(1900)$, $Y(2175)$, $Y(4260)$, $Y(4320)$, etc.], some of them with presumably exotic quark structure, have been discovered. Their nature is not yet established and widely discussed.

New values of the cross sections obtained using ISR can be used for more precise predictions of the muon anomalous magnetic moment, running fine-structure constant at the $Z$ boson mass, tests of CVC, and many other theoretical models.

Only part of the available ISR data sample has been processed, e.g., for *BABAR* it is about 1/3, and analysis is in progress. Belle has only started a corresponding data processing.

If existing projects of Super $B$ factories are approved, prospects of reaching an integrated luminosity by a factor of 30–100 exceeding that today appear. Such experiments will improve accuracy for many processes in which studies are now statistically limited.

## ACKNOWLEDGMENTS

The authors are grateful to Vera Luth for the idea of this review. We are indebted to our colleagues from the *BABAR* and Belle Collaborations for many years of fruitful work. Thanks are also due to Brian Heltsley from CLEO and Graziano Venanzoni from KLOE for valuable comments. This work was supported in part by RFBR Grants No. 10-02-00695, No. 11-02-00112, No. 11-02-00558, and DFG Grant No. GZ 436 RUS 113/769/0-3.

## REFERENCES

Abashian, A., *et al.* (Belle Collaboration), 2002, Nucl. Instrum. Methods Phys. Res., Sect. A **479**, 117.

Ablikim, M., *et al.* (BES Collaboration), 2005, Phys. Lett. B **630**, 14.

Ablikim, M., *et al.* (BES Collaboration), 2008, Phys. Lett. B **660**, 315.

Achasov, M. N., *et al.* (SND Collaboration), 2002, Phys. Rev. D **66**, 032001.

Achasov, M. N., *et al.* (SND Collaboration), 2003, J. Exp. Theor. Phys. **96**, 789.

Achasov, M. N., *et al.* (SND Collaboration), 2006, J. Exp. Theor. Phys. **103**, 380.

Actis, S., *et al.*, 2010, Eur. Phys. J. C **66**, 585.

Adam, N. E., *et al.* (CLEO Collaboration), 2006, Phys. Rev. Lett. **96**, 082004.

Adams, G. S., *et al.* (CLEO Collaboration), 2006, Phys. Rev. D **73**, 051103.

Agostinelli, S., *et al.* (GEANT4 Collaboration), 2003, Nucl. Instrum. Methods Phys. Res., Sect. A **506**, 250.

Akhmetshin, R. R., *et al.* (CMD-2 Collaboration), 1999, Phys. Lett. B **466**, 392.

Akhmetshin, R. R., *et al.* (CMD-2 Collaboration), 2000, Phys. Lett. B **489**, 125.

Akhmetshin, R. R., *et al.* (CMD-2 Collaboration), 2004a, Phys. Lett. B **578**, 285.

Akhmetshin, R. R., *et al.* (CMD-2 Collaboration), 2004b, Phys. Lett. B **595**, 101.

Akhmetshin, R. R., *et al.* (CMD-2 Collaboration), 2007, Phys. Lett. B **648**, 28.

Alemany, R., M. Davier, and A. Höcker, 1998, Eur. Phys. J. C **2**, 123.

Aloisio, A., *et al.* (KLOE Collaboration), 2005, Phys. Lett. B **606**, 12.

Ambrogiani, M., *et al.* (E835 Collaboration), 1999, Phys. Rev. D **60**, 032002.

Ambrosino, F., *et al.* (KLOE Collaboration), 2009, Phys. Lett. B **670**, 285.

Ambrosino, F., *et al.* (KLOE Collaboration), 2011, Phys. Lett. B **700**, 102.

Amsler, C., *et al.* (Particle Data Group), 2008, Phys. Lett. B **667**, 1.

Antonelli, A., *et al.* (DM2 Collaboration), 1988, Phys. Lett. B **212**, 133.

Antonelli, A., *et al.* (DM2 Collaboration), 1992, Z. Phys. C **56**, 15.

Antonelli, A., *et al.* (FENICE Collaboration), 1996, Phys. Lett. B **365**, 427.

Antonelli, A., *et al.* (FENICE Collaboration), 1998, Nucl. Phys. B **517**, 3.

Arbuzov, A. B., *et al.*, 1998, J. High Energy Phys. 12, 009.

Armstrong, T. A., *et al.* (E760 Collaboration), 1993, Phys. Rev. Lett. **70**, 1212.

Aubert, B., *et al.* (*BABAR* Collaboration), 2002, Nucl. Instrum. Methods Phys. Res., Sect. A **479**, 1.

Aubert, B., *et al.* (*BABAR* Collaboration), 2004a, Phys. Rev. D **69**, 011103.

Aubert, B., *et al.* (*BABAR* Collaboration), 2004b, Phys. Rev. D **70**, 072004.

Aubert, B., *et al.* (*BABAR* Collaboration), 2005a, Phys. Rev. Lett. **95**, 142001.

Aubert, B., *et al.* (*BABAR* Collaboration), 2005b, Phys. Rev. D **71**, 052001.

Aubert, B., *et al.* (*BABAR* Collaboration), 2006a, Phys. Rev. D **73**, 012005.

Aubert, B., *et al.* (*BABAR* Collaboration), 2006b, Phys. Rev. D **73**, 052003.

Aubert, B., *et al.* (*BABAR* Collaboration), 2007a, Phys. Rev. Lett. **98**, 212001.

Aubert, B., *et al.* (*BABAR* Collaboration), 2007b, Phys. Rev. D **76**, 012008.

Aubert, B., *et al.* (*BABAR* Collaboration), 2007c, Phys. Rev. D **76**, 092005; **77**, 119902 (2008).

Aubert, B., *et al.* (*BABAR* Collaboration), 2007d, Phys. Rev. D **76**, 092006.

Aubert, B., *et al.* (*BABAR* Collaboration), 2007e, Phys. Rev. D **76**, 111105.

Aubert, B., *et al.* (*BABAR* Collaboration), 2008a, arXiv:0808.1543.

Aubert, B., *et al.* (*BABAR* Collaboration), 2008b, Phys. Rev. D **77**, 092002.

Aubert, B., *et al.* (*BABAR* Collaboration), 2009a, Phys. Rev. Lett. **103**, 231801.

Aubert, B., *et al.* (*BABAR* Collaboration), 2009b, Phys. Rev. D **79**, 092001.

Aulchenko, V. M., *et al.* (CMD-2 Collaboration), 2005, JETP Lett. **82**, 743.

Aulchenko, V. M., *et al.* (CMD-2 Collaboration), 2006, JETP Lett. **84**, 413.

Bacci, C., *et al.* ($\gamma\gamma 2$ Collaboration), 1980, Phys. Lett. B **95**, 139.

Bacci, C., *et al.* ($\gamma\gamma 2$ Collaboration), 1981, Nucl. Phys. B **184**, 31.

Bai, J. Z., *et al.* (BES Collaboration), 1998, Phys. Rev. D **58**, 092006.

Bai, J. Z., *et al.* (BES Collaboration), 2002, Phys. Rev. Lett. **88**, 101802.

Bai, J. Z., *et al.* (BES Collaboration), 2004, Phys. Rev. D **70**, 012005.

Baier, V. N., and V. S. Fadin, 1968, Phys. Lett. B **27**, 223.

Baier, V. N., and V. A. Khoze, 1965, Sov. Phys. JETP **21**, 1145.

Baldini, R., *et al.*, 2009, Eur. Phys. J. A **39**, 315.

Barberio, E., B. van Eijk, and Z. Was, 1991, Comput. Phys. Commun. **66**, 115.

Bardin, G., *et al.* (PS170 Collaboration), 1994, Nucl. Phys. B **411**, 3.

Barnes, T., S. Godfrey, and E. S. Swanson, 2005, Phys. Rev. D **72**, 054026.

Benayoun, M., *et al.*, 1999, Mod. Phys. Lett. A **14**, 2605.

Benayoun, M., *et al.*, 2011, arXiv:1106.1315.

Bennett, G. W., *et al.* (E821 Collaboration), 2006, Phys. Rev. D **73**, 072003.

Bergfeld, T., *et al.* (CLEO Collaboration), 1997, Phys. Rev. Lett. **79**, 2406.

Binner, S., J. H. Kühn, and K. Melnikov, 1999, Phys. Lett. B **459**, 279.

Bisello, D., *et al.* (DM1 Collaboration), 1981, Phys. Lett. B **107**, 145.

Bisello, D., *et al.* (DM2 Collaboration), 1983, Nucl. Phys. B **224**, 379.

Bisello, D., *et al.* (DM2 Collaboration), 1989, Phys. Lett. B **220**, 321.

Bisello, D., *et al.* (DM2 Collaboration), 1990, Z. Phys. C **48**, 23.

Bisello, D., *et al.* (DM2 Collaboration), 1991a, Nucl. Phys. B, Proc. Suppl. **21**, 111.

Bisello, D., *et al.* (DM2 Collaboration), 1991b, Z. Phys. C **52**, 227.

Bityukov, S. I., *et al.*, 1987, Phys. Lett. B **188**, 383.

Bonneau, G., and F. Martin, 1971, Nucl. Phys. B **27**, 381.

Bouchiat, C., and L. Michel, 1961, J. Phys. Radium **22**, 121.

Brambilla, H., *et al.* (QWG Collaboration), 2011, Eur. Phys. J. C **71**, 1534.

Brandelik, R., *et al.* (DASP Collaboration), 1978, Phys. Lett. B **76**, 361.

Buon, J., *et al.* (DM1 Collaboration), 1982, Phys. Lett. B **118**, 221.

Burkhardt, H., and B. Pietrzyk, 2005, Phys. Rev. D **72**, 057501.

Burkhardt, H., *et al.*, 1989, Z. Phys. C **43**, 497.

Caffo, M., H. Czyż, and E. Remiddi, 1994, Phys. Lett. B **327**, 369.

Caffo, M., H. Czyż, and E. Remiddi, 1997, Nuovo Cimento Soc. Ital. Fis. A **110**, 515.

Castellano, M., *et al.*, 1973, Nuovo Cimento Soc. Ital. Fis. A **14**, 1.
Castro, A., 1988, LAL-88-58.
Cherepanov, V. A., and S. I. Eidelman, 2009, JETP Lett. **89**, 429.
Chernyak, V. L., and A. R. Zhitnitsky, 1977, JETP Lett. **25**, 510.
Chernyak, V. L., *et al.*, 1989, Z. Phys. C **42**, 569.
Coan, T. E., *et al.* (CLEO Collaboration), 2006, Phys. Rev. Lett. **96**, 162003.
Cordier, A., *et al.* (DM1 Collaboration), 1981, Phys. Lett. B **106**, 155.
Cordier, A., *et al.* (DM1 Collaboration), 1982a, Phys. Lett. B **109**, 129.
Cordier, A., *et al.* (DM1 Collaboration), 1982b, Phys. Lett. B **110**, 335.
Cosme, G., *et al.* (M3N Collaboration), 1979, Nucl. Phys. B **152**, 215.
Cronin-Hennessy, D., *et al.* (CLEO Collaboration), 2009, Phys. Rev. D **80**, 072001.
Czyż, H., A. Grzelinska, and J. H. Kühn, 2007, Phys. Rev. D **75**, 074026.
Czyż, H., and J. H. Kühn, 2001, Eur. Phys. J. C **18**, 497.
Czyż, H., *et al.*, 2003, Eur. Phys. J. C **27**, 563.
Czyż, H., *et al.*, 2004, Eur. Phys. J. C **35**, 527.
D'Agostini, G., 1995, Nucl. Instrum. Methods Phys. Res., Sect. A **362**, 487.
Datta, A., and P. J. O'Donnell, 2003, Phys. Lett. B **567**, 273.
Davier, M., 2007, Nucl. Phys. B, Proc. Suppl. **169**, 288.
Davier, M., *et al.*, 2003a, Eur. Phys. J. C **27**, 497.
Davier, M., *et al.*, 2003b, Eur. Phys. J. C **31**, 503.
Davier, M., *et al.*, 2010a, Eur. Phys. J. C **66**, 1.
Davier, M., *et al.*, 2010b, Eur. Phys. J. C **66**, 127.
Davier, M., *et al.*, 2011, Eur. Phys. J. C **71**, 1515.
del Amo Sanchez, P., *et al.* (*BABAR* Collaboration), 2010, Phys. Rev. D **82**, 052004.
Delcourt, B., *et al.* (DM1 Collaboration), 1979, Phys. Lett. B **86**, 395.
Delcourt, B., *et al.* (DM1 Collaboration), 1982, Phys. Lett. B **113**, 93.
Dmitriev, V. F., and A. I. Milstein, 2007, Phys. Lett. B **658**, 13.
Dolinsky, S. I., *et al.* (ND Collaboration), 1991, Phys. Rep. **202**, 99.
Druzhinin, V. P., 2007, arXiv:0710.3455.
Druzhinin, V. P., *et al.* (ND Collaboration), 1986, Phys. Lett. B **174**, 115.
Dubnickova, A. Z., S. Dubnicka, and M. P. Rekalo, 1996, Nuovo Cimento Soc. Ital. Fis. A **109**, 241.
Eichten, E. J., K. Lane, and C. Quigg, 2006, Phys. Rev. D **73**, 014014; **73**, 079903(E) (2006).
Eichten, E. J., *et al.*, 1980, Phys. Rev. D **21**, 203.
Eichten, E. J., *et al.*, 2008, Rev. Mod. Phys. **80**, 1161.
Eidelman, S., and F. Jegerlehner, 1995, Z. Phys. C **67**, 585.
Eidelman, S., *et al.* (Particle Data Group), 2004, Phys. Lett. B **592**, 1.
Eidelman, S. I., and V. N. Ivanchenko, 1991, Phys. Lett. B **257**, 437.
Esposito, B., *et al.* (MEA Collaboration), 1981, Lett. Nuovo Cimento Soc. Ital. Fis. **31**, 445.
Frabetti, P. L., *et al.* (FOCUS Collaboration), 2001, Phys. Lett. B **514**, 240.
Franzini, P., and M. Moulson, 2006, Annu. Rev. Nucl. Part. Sci. **56**, 207.
Gomez-Avila, S., M. Napsuciale, and E. Oset, 2009, Phys. Rev. D **79**, 034018.
Gourdin, M., and E. de Rafael, 1969, Nucl. Phys. B **10**, 667.
Hagiwara, K., *et al.*, 2003, Phys. Lett. B **557**, 69.
Hagiwara, K., *et al.*, 2007, Phys. Lett. B **649**, 173.
Hagiwara, K., *et al.*, 2011, J. Phys. G **38**, 085003.
He, Q., *et al.* (CLEO Collaboration), 2006, Phys. Rev. D **74**, 091104.
Inami, K., *et al.* (Belle Collaboration), 2009, Phys. Lett. B **672**, 209.
Jean-Marie, B., *et al.* (Maek-II Collaboration), 1976, Stanford Linear Accelerator Center Report No. SLAC-PUB-1711.
Jegerlehner, F., and A. Nyffeler, 2009, Phys. Rep. **477**, 1.
Jegerlehner, F., and R. Szafron, 2011, Eur. Phys. J. C **71**, 1632.
Kardapoltzev, L. V., 2007, Bachelor's thesis (Novosibirsk State University) (unpublished).
Kawamoto, N., and A. I. Sanda, 1978, Phys. Lett. B **76**, 446.
Khoze, V. A., *et al.*, 2001, Eur. Phys. J. C **18**, 481.
Khoze, V. A., *et al.*, 2002, Eur. Phys. J. C **25**, 199.
Konchatnij, M. I., and N. P. Merenkov, 1999, JETP Lett. **69**, 811.
Kuraev, E. A., and V. S. Fadin, 1985, Sov. J. Nucl. Phys. **41**, 466.
Kurdadze, L. M., *et al.* (Olya Collaboration), 1984, Sov. J. Nucl. Phys. **40**, 286.
Kurdadze, L. M., *et al.* (Olya Collaboration), 1986, JETP Lett. **43**, 643.
Kurdadze, L. M., *et al.* (Olya Collaboration), 1988, JETP Lett. **47**, 512.
Kurokawa, S., and E. Kikutani, 2003, Nucl. Instrum. Methods Phys. Res., Sect. A **499**, 1, and other papers included in this volume.
Lees, J. P., *et al.* (*BABAR* Collaboration), 2011, arXiv:1103.3001.
Liu, Z. Q., X. S. Qin, and C. Z. Yuan, 2008, Phys. Rev. D **78**, 014032.
Malaescu, B., 2009, arXiv:0907.3791.
Mo, X. H., *et al.*, 2006, Phys. Lett. B **640**, 182.
Muller, S. E. (KLOE Collaboration), 2010, Chinese Phys. C **34**, 686.
Nakamura, K., *et al.*, 2010, J. Phys. G **37**, 075021.
Napsuciale, M., *et al.*, 2007, Phys. Rev. D **76**, 074012.
Osterheld, A., *et al.* (Crystal Ball Collaboration), Stanford Linear Accelerator Center Report No. SLAC-PUB-4160, 1986.
Pakhlova, G., *et al.* (Belle Collaboration), 2007, Phys. Rev. Lett. **98**, 092001.
Pakhlova, G., *et al.* (Belle Collaboration), 2008a, Phys. Rev. D **77**, 011103.
Pakhlova, G., *et al.* (Belle Collaboration), 2008b, Phys. Rev. Lett. **100**, 062001.
Pakhlova, G., *et al.* (Belle Collaboration), 2008c, Phys. Rev. Lett. **101**, 172001.
Pakhlova, G., *et al.* (Belle Collaboration), 2009, Phys. Rev. D **80**, 091101.
Pakhlova, G., *et al.* (Belle Collaboration), 2011, Phys. Rev. D **83**, 011101.
Pakhlova, G. V., P. N. Pakhlov, and S. I. Eidelman, 2010, Phys.-Usp. **53**, 219.
Pedlar, T. K., *et al.* (CLEO Collaboration), 2005, Phys. Rev. Lett. **95**, 261803.
Prades, J., E. de Rafael, and A. Vainshtein, 2009, arXiv:0901.0306.
Renard, F. M., 1981, *Basics of Electron Positron Collisions* (Editions Frontieres, Gif sur Yvette, France).
Rodrigo, G., *et al.*, 2001, Eur. Phys. J. C **22**, 81.
Rodrigo, G., *et al.*, 2002, Eur. Phys. J. C **24**, 71.
Seeman, J. T., *et al.*, Stanford Linear Accelerator Center Report No. SLAC-PRPRINT-2001-040, 2001.
Seth, K. K., 2005, Phys. Rev. D **72**, 017501.
Shen, C. P., *et al.* (Belle Collaboration), 2009, Phys. Rev. D **80**, 031101.
Shifman, M. A., A. I. Vainshtein, and V. I. Zacharov, 1979, Nucl. Phys. B **147**, 385.
Siegrist, J. L., *et al.* (MARK-I Collaboration), 1976, Phys. Rev. Lett. **36**, 700.
Swanson, E. S., 2006, Phys. Rep. **429**, 243.

Thacker, H. B., and J. J. Sakurai, 1971, Phys. Lett. B **36**, 103.
Tsai, Y. S., 1971, Phys. Rev. D **4**, 2821; **13**, 771(E) (1976).
Tzara, C., 1970, Nucl. Phys. B **18**, 246.
Vasserman, I. B., *et al.* (ND Collaboration), 1988, Sov. J. Nucl. Phys. **47** 1035.
Wang, W. F. (*BABAR* Collaboration), 2009, in *Proceedings of the International Workshop on $e^+e^-$ Collisions from phi to psi (PHIPSI09), Beijing, China* (IOP Publishing Ltd., Beijing).
Wang, X. L., *et al.* (Belle Collaboration), 2007, Phys. Rev. Lett. **99**, 142002.
Yao, W. M., *et al.* (Particle Data Group), 2006, J. Phys. G **33**, 1.
Yuan, C. Z., *et al.* (Belle Collaboration), 2007, Phys. Rev. Lett. **99**, 182004.
Yuan, C. Z., *et al.* (Belle Collaboration), 2008, Phys. Rev. D **77**, 011105.